



Développement et optimisation d'une cellule à cristaux liquides adaptative pour la correction dynamique de la vision maculaire

Thèse

Louis Bégel

Philosophiæ doctor (Ph. D.)

Québec, Canada

© Louis Bégel, 2025

Développement et optimisation d'une cellule à cristaux liquides adaptative pour la correction dynamique de la vision maculaire

Thèse

Louis Bégel

Sous la direction de:

Tigran Galstian, directeur de recherche

Résumé

Cette thèse porte sur le développement d'une lentille à cristaux liquides adaptative (LCL) destinée aux systèmes optiques de grande ouverture, avec un accent particulier sur la correction dynamique des aberrations optiques de l'œil humain. Une architecture dites "quadripolaire" innovante, combinée à une nouvelle configuration d'électrodes résistive, permet un contrôle précis et en temps réel des paramètres de la lentille. Les résultats expérimentaux démontrent la mise en place de lentilles ajustables dynamiquement, avec des puissances optique (PO) convergentes ou divergentes ($-5 \leq PO \leq 40$ D), des diamètres variant du sous-millimètre ($\geq 0.65mm$) à plusieurs millimètres ($\leq 6.5mm$), pouvant être positionnées librement au sein d'une large ouverture optique ($\geq 25mm^2$). Ce dispositif se distingue par sa faible consommation énergétique ($\leq 5V$), ses temps de réponse rapides ($\leq 0.5s$), le rendant particulièrement adapté à des applications telles que l'amélioration de l'acuité visuelle humaine, avec l'imagerie adaptative. En intégrant une analyse du front d'onde, le système permet une correction des aberrations optiques de bas ordre (défocalisation, astigmatismes, inclinaison (tip/tilt), etc.), ouvrant ainsi la voie à des solutions de correction visuelle personnalisée. La modélisation théorique et la validation expérimentale confirment la capacité de la lentille à moduler dynamiquement le front d'onde optique. Ces travaux établissent cette lentille à cristaux liquides comme une alternative prometteuse, offrant une adaptabilité supérieure aux optiques correctrices statiques, avec des applications potentielles en ophtalmologie, réalité augmentée et imagerie de haute précision.

Abstract

This thesis focuses on the development of an adaptive liquid crystal lens (LCL) designed for large-aperture optical systems, with a particular emphasis on the dynamic correction of human eye aberrations. An innovative so-called "quadripolar" architecture, combined with a novel resistive electrode configuration, enables precise and real-time control of the lens parameters. Experimental results demonstrate the implementation of dynamically adjustable lenses, with converging or diverging optical power (OP) ranging from -5 to 40 diopters, and diameters varying from the sub-millimeter scale (≥ 0.65 mm) to several millimeters (≤ 6.5 mm), freely positionable within a large optical aperture (≥ 25 mm²). This device stands out due to its low power consumption (≤ 5 V) and fast response times (≤ 0.5 s), making it particularly suitable for applications such as human visual acuity enhancement and adaptive imaging. By integrating wavefront analysis, the system enables the correction of low-order optical aberrations (defocus, astigmatism, tilt, etc.), paving the way for personalized vision correction solutions. Theoretical modeling and experimental validation confirm the lens's ability to dynamically modulate the optical wavefront. These findings establish this liquid crystal lens as a promising alternative, offering superior adaptability compared to static corrective optics, with potential applications in ophthalmology, augmented reality, and high-precision imaging.

Table des matières

Résumé	iii
Abstract	iv
Table des matières	v
Liste des tableaux	vii
Liste des figures	viii
Remerciements	xiii
Avant-propos	xiv
Introduction	1
1 Les notions théoriques	3
1.1 Optique de l’Œil : Formation des Images et Perception	3
1.2 Notion de Front d’Onde et Aberrations Optiques : Analyse et Correction . .	7
1.2.1 Décomposition du Front d’Onde à l’Aide des Polynômes de Zernike .	7
1.2.2 Techniques de Mesure du Front d’Onde : Principes et Applications .	9
1.2.3 Impact du Front d’Onde sur la Qualité de l’Image Rétinienne	11
1.2.4 Correction des Aberrations Optiques par Optique Adaptative	13
1.3 Cristaux Liquides : Structure, Phases et Propriétés Électro-Optiques	14
1.3.1 Propriétés physique des cristaux liquides nématiques (NLC)	16
1.3.2 Réponse des NLC à un Champ Électrique	18
Le couple électrique	18
Réponse statique des NLC	21
Réponse dynamique des NLC	24
Temps de relaxation :	24
Temps d’activation :	25
1.3.3 Propagation d’une onde electromagnétique dans un NLC	25
1.4 Lentilles de Cristaux Liquides : Design et Modélisation	27
1.4.1 Lentilles dites "modales" vs Lentilles "quadripolaire"	27
2 Adaptive lens for foveal vision, imaging and projection over large clear apertures	32
2.1 Introduction	33
2.2 Structure of the lens and its operation principle	35

2.3	Experimental results	39
2.4	Discussions and Conclusions	47
3	Dynamic control of defocus, astigmatism and tilt aberrations with a large area foveal liquid crystal lens	50
3.1	Introduction	50
3.2	Structure and operating principle	51
3.3	Results and discussion	55
3.4	Summary and Conclusions	63
4	Dynamic presbyopia correction in the macular field of view by using a liquid crystal lens	65
4.1	Introduction	66
4.2	Design and operating principle of the lens	67
4.3	Experimental results	72
4.3.1	Transition speed measurements and optimization	77
4.3.2	Application in presbyopia correction	82
	Conclusion	89
	Bibliographie	91

Liste des tableaux

1.1	Polynômes de Zernike et leurs aberrations associées	9
1.2	Illustration des polynômes de Zernike	9
3.1	Amplitude and phase settings between orthogonal electrodes used to generate astigmatism along the desired axis.	60
3.2	Amplitude setting on electrodes A, B, C and D for Defocus + Tilt generation. .	61

Liste des figures

1.1	Schéma du système optique de l'oeil humain.	4
1.2	Schéma de l'organisation cellulaire de la rétine, basé sur [1].	5
1.3	Acuité visuelle en fonction de la position de l'image sur la rétine [2]	6
1.4	Représentation 3D de échantillonnage du front d'onde à l'aide d'une matrice de microlentilles d'un Shack-Hartmann	10
1.5	Mesures des MTF en lumière blanche de l'œil, réalisées par Campbell et Gubisch (1966), pour une gamme de diamètres pupillaires. Moyenne de trois sujets [3]	12
1.6	Représentation schématique de la correction du front d'onde en réflexion à l'aide d'un miroir déformable et en transmission à l'aide d'un SLM	14
1.7	Représentation des mesophases des molécules en formes de batonnets (basé sur [4])	15
1.8	- Morphologie des mésogènes conduisant à des mésophases thermotropes [5]	16
1.9	Représentation des différents type d'ancrage, planaire, planaire twisté et homeotrope	17
1.10	Schéma des différentes déformations de l'axe du directeur n	18
1.11	Alignement du NLC suivant le champ électrique appliqué.	19
1.12	Couple électrique vs l'angle θ - ψ	20
1.13	Représentation des CL d'une cellule au repos (a gauche). Et leur réorientation suite à un champ électrique externe (a droite)	23
1.14	Angle du directeur n au centre de la cellule en fonction du champ électrique E appliqué. Avec E_c le champ électrique de seuil.	23
1.15	Représentation de la biréfringence	25
1.16	Illustration présentant la différence entre une lentille à cristaux liquides dite "modale" et une lentille dite "quadripolaire"	28
1.17	Circuit équivalent du système de lentille à cristaux liquides	29
1.18	Evolution temporelle du potentiel électrique sur une période au travers d'une lentille simple à électrodes résistives	30
1.19	Profil du potentiel électrique moyenné sur une période	30
1.20	Profils moyens de $U+V_{offset}$ à 20Hz pour différentes amplitudes du signal offset : de 0 V_{RMS} , 1.2 V_{RMS} et 2 V_{RMS} de gauche à droite.	31
1.21	Caption	31
2.1	Schematic demonstration of the device, a) 3D representation showing the electrode configuration and key layers, b) Top view of two cross-oriented serpentine patterns of ITO in the unit area of 0.65 mm \times 0.65 mm.	36

2.2	Schematic demonstration of 4 phase-shifted electrical control signals (applied to contacts A, B, C and D) with an additional low frequency offset voltage shown by 4 horizontal curved dashed lines, with periods $T_1 = 1/F$ and $T_2 = 1/f$, respectively. Vertical dashed lines 1-4 show the phase shift between signals : Line 1 correspond to phase 0, Line 2 : $\pi/4$, Line 3 : $\pi/2$ and Line 4 : $3\pi/2$ of the period T_1	38
2.3	Cross sectional view of V_{RMS} voltage distribution along X and Y axis, over the oscillation cycle ; a) No offset voltage is applied ; the dark rectangle corresponds to the area of the lens below threshold voltage, b) Adding alternative offset equal to V_{th} : during the first half period T_2 of the offset (filled triangles correspond to the top substrate voltage distribution profile and filled circles correspond to the bottom substrate), and vice versa for the second half period (see main text for details).	39
2.4	Schematic presentations of experimental setups used for lens characterization. (a) polarimetric measurements, (b) Shack-Hartmann wavefront sensing.	40
2.5	a) Polarimetric interference patterns for $V = 2 V_{RMS}$, $2.5 V_{RMS}$ and $3.0 V_{RMS}$, from left to right, respectively, and $V_{off} = 1.2 V_{RMS}$, (b and c) Optical path length for two different lens diameters (1.3 mm and 4.55 mm), obtained from Shack Hartmann measurements, with increment of $0.1 V_{RMS}$	41
2.6	Interference pattern for several lens sizes, ranging from $CA = 0.65$ mm to $CA = 4.55$ mm, $V = 3.2 V_{RMS}$ and $V_{off} = 1.2 V_{RMS}$	42
2.7	Optical characterization of lenses of various sizes, ranging from 1.3 mm to 4.55 mm, a) OP vs voltage, b) Total RMS wavefront error vs voltage, c) RMS wavefront error for spherical aberrations vs voltage. Hatched zones correspond to max and min values measured for each lens size.	43
2.8	a) Interference patterns for several positions of a lens (with the same $CA = 1.3$ mm) through the surface of the MTLCL. $V = 3.2 V_{RMS}$ and $V_{off} = 1.2 V_{RMS}$; b) Electric field's profile through the active lens (line P_2) and through the addressing electrodes (line P_1).	44
2.9	Left column : theoretical simulations of the electric field distribution depending upon the external electrodes' states, floating : F ; ground : G ; V_a, V_b, V_c and V_d : A/B/C/D signals. Right column : experimental observations of the interference pattern. a) Reference image, all electrodes are in the floating (off) state. Lens generation : b) applied 4 phase shifted signals $V_a/V_b/V_c$ and V_d , while maintaining external electrodes in floating states. c) external electrodes are in Ground state. d) external electrodes are in the same state as the control signals applied to the peripheral control electrodes of the desired zone.	46
2.10	Impact of the MTLCL on the local image quality recorded on a random scene by using a commercial Raspberry Pi camera combined with MTLCL, a) original photo, MTLCL is off. b) photo with a local lens (with 3.9 mm diameter) activated (at $3.6 V_{RMS}$), focused on the area "Think Python". c) the corresponding modulation transfer functions of the region of interest.	47

3.1	(a) Schematic 3D representation of the device showing electrodes' structure, orientation, and contact electrodes' positions (e.g., 1-5 on top and 6-10 on bottom substrates), (b) Top schematic view, example of a "smallest lens unit" area (shown by the dashed red rectangle), where 2-3 & 7-8 represent activated contact electrodes (on top & bottom substrates) with corresponding signals V_a, V_b, V_c and V_d	52
3.2	Coordinate for a square pupil inscribed outside a unit circle.	55
3.3	(a) Digitally reconstructed wavefronts by using square Zernike polynomials (described in the main text), coupling AST0 and defocus from $a_6 = 0.375\mu m$ and $a_4 = 1.7\mu m$, respectively; (b) Experimentally obtained polarimetric images, confirming the generation of tunable vertical/horizontal astigmatism (AST0) with amplitude difference ΔV applied between top and bottom electrodes. . . .	57
3.4	(a) Digitally reconstructed wavefronts with a square aperture, coupling AST45 and defocus with $a_5 = 0.5\mu m$ and $a_4 = 1.7\mu m$, respectively; (b) Experimental generation of tunable oblique astigmatism (AST45) with phase shift control $\Delta\varphi$	58
3.5	Different driving modes and corresponding astigmatism Zernike coefficients (AST45 = a_5 and AST0 = a_6); (a) and (b) Each bar shows the dependence of the Zernike coefficient's variation on the applied electric field. Optical power (OP) variation is represented by red circles and the total RMS aberrations (without considering astigmatism and defocus) are plotted by black triangles; (c) and (d) Amplitudes and phase settings on electrodes A, B, C and D for AST45 and AST0 generation, respectively.	59
3.6	Examples of generating astigmatism with precise control along arbitrary (desired) directions.	60
3.7	a) Digital wavefront reconstruction of $Tilt_y$ $b_2 = 0.8\mu m$ and Defocusing $b_4 = 1.7\mu m$ aberrations; b) Experimental demonstration of Tilt and Defocus control. These configurations are chosen for demonstration purpose with $\Delta V = 0.8V$, showing several combination of Tilt x + Tilt y + Defocus.	61
3.8	Demonstration of the possibility of generating and controlling a tunable negative lens with CA=2.3 mm (a-c : top pictures show the polarimetric images, obtained for different optical power values, while the bottom curves show the corresponding reconstructed waveforms (obtained from polarimetric data). . . .	62
4.1	a) Schematic top view of transparent electrodes of the lens. b) Zoom on the corner of the patterned electrodes and c) Schematic 3D view of the lens. External contact electrodes (dark rectangles) are arranged at a constant distance. d) Top photography of the lens with flat printed connectors (FPC) and flat flexible cables (FFC).	68
4.2	Schematic representation of the proposed MTLCL with two (cross-oriented) LC layers (sandwiched between two flat substrates and laminated together) with dynamically changing positions of local lenses following the region of interest (RoI) for a human eye. The orange ellipses represent molecules. a) The limited field of view (FOV) focusing on the retina, with the tunable lens size (local CA) necessary to adjust the focus on the retina. b) The focal shift on the retina with a presbyopia eye. c) Local lens activated in the RoI to bring in focus the letter E, while keeping uniform the periphery (under the red colored electrodes). d) The same as above but for the letter F.	71

4.3	Excitation dependencies of RMS aberrations and OP values for various sizes of the clear aperture of the local lens.	73
4.4	Comparative images of a target object (2D array of white squares) formed with the use of the MTLCL for different regions of interest, a) in the center and b) shifted to the top left. Dashed square corresponds to the MTLCL area. FFC1/2/3 and 4 correspond to the flat flexible cable positions activated to create the lens in a).	74
4.5	Two numerical solutions	76
4.6	Temporal evolution of polarimetric interference patterns (recording moments are displayed on the top of each image), a) without overdrive, $U = 3.5$ V b) with overdrive 20 V applied during $\Delta t = 0.19$ s.	79
4.7	Example of a non-optimized transition dynamics (change of the normalized optical power, OP) illustrating the slow response during the activation (turn-on) and relaxation for the following specific example of electrical excitation conditions : $U = 3.5$ V, $F = 120$ Hz, $U_{off} = 1.2$ V, and $f = 20$ Hz.	80
4.8	Examples of optimization of the speed of the MTLCL with a) 14 V and b) 20 V overdrive (OD) voltages, applied with various pulse durations (Δt), compared with the normal drive response (without overdrive).	81
4.9	Demonstrations of transition times with relatively high amplitude (HA) excitations at various frequencies from a predefined lens state (S2) to either a) to a quasi homeotropic state S3, or b) to a quasi planar state S1, both with zero OP.	82
4.10	Demonstration of the impact of the MTLCL on visual acuity of 7 patients.	85
4.11	Comparison between natural correction and when the MTLCL lens is activated (by using the average VA for users).	86

A mes parents

Remerciements

Je souhaite exprimer ma gratitude envers mon directeur de thèse, **Tigran Galstian**, pour son soutien tout au long de cette aventure. Son engagement et sa passion ont été une source constante d'inspiration et de motivation, me permettant de surmonter les défis rencontrés au fil du projet. Ce travail n'aurait pas été possible sans son accompagnement, et je lui suis reconnaissant pour l'opportunité qu'il m'a offerte, tant sur le plan scientifique que personnel.

Un grand merci à l'équipe de recherche, en particulier **Loïc, Anastasiia, Oleksandr, Justin, Arthur, Jonathan, Marc-Antoine, Frédéric, Zhanna** et **Maria**. Nos échanges ont largement contribué à l'avancement de mes recherches et ont rendu cette expérience encore plus enrichissante.

Je tiens également à remercier l'équipe de LensVector, notamment **Armen, Aram, Mikhail, Vladimir** et **Seydou** pour leurs précieux conseils, l'accès à leurs équipements et leur aide à chaque étape du projet.

Enfin, un grand merci à **Patrick Larochelle**, dont l'aide précieuse et les solutions apportées ont été déterminantes pour la réussite de ce travail.

Évidemment, un merci particulier à mes proches, amis et famille dont la présence et vos encouragements ont été essentiels pour traverser cette expérience.

À tous, merci infiniment.

Avant-propos

Cette thèse se compose de 4 chapitres , dont le premier est consacré à l'exposé des fondements théoriques. Les 3 autres chapitres correspondent à 3 articles scientifiques, qui ont été publiés dans des revues à comité de lecture.

Le chapitre 1 vise à établir les bases nécessaires à la compréhension des chapitres à venir tout en fournissant un aperçu de l'état actuel de la recherche et en décrivant nos objectifs... Nous présenterons les bases théoriques des cristaux liquides afin de faciliter la compréhension sur les principes de fonctionnement des lentilles ajustables à base de cristaux liquides. Nous introduirons les concepts fondamentaux des lentilles quadripolaires au travers d'une matrice, qui seront abordées dans les chapitres suivants. Enfin, nous présenterons les résultats atteints avec cette innovation au travers des différents articles, formatés pour correspondre à la mise en page de la thèse.

Chapitre 2 :

— "*Adaptive lens for foveal vision, imaging, and projection over large clear apertures*",
Begel, L., Khodadad, B., Galstian, T., publié dans Optics Express (2023).

Cet article présente la possibilité de générer des lentilles dont le diamètre peut être dynamiquement modifié de sous-millimétrique (0.65mm) à plusieurs millimètres (5.2mm). Ces lentilles peuvent être créées dans différentes régions d'intérêt sur de grandes ouvertures optiques (supérieures à 25 mm²). La méthode repose sur l'activation d'électrodes périodiquement espacées, basée sur une configuration en forme de serpent avec des signaux électriques déphasés. Un assemblage hautement reconfigurable, où des lentilles sont localement créées avec une position, un diamètre, une puissance optique (OP) variables, tout en limitant au maximum les perturbations extérieures à la zone d'intérêt.

Chapitre 3 :

- "*Dynamic control of defocus, astigmatism and tilt aberrations with a large area foveal liquid crystal lens*",
Begel, L., Galstian, T., publié dans Optics Express (2024).

Dans cette étude, nous démontrons que ce design permet également de générer indépendamment un astigmatisme avec un axe et une amplitude arbitraires en modifiant les phases et les différences de tension entre les 4 électrodes de contrôle. De plus, nous montrons la capacité du dispositif à générer des lentilles divergentes localisées en utilisant un cristal liquide à double fréquence (DFNLC).

Chapitre 4 :

- "*Macular accommodative vision with advanced presbyopia correction using liquid crystals*",
Begel, L., Galstian, T., publié dans Optics Express (2024).

Ce dispositif, pouvant couvrir une grande surface (similaire à des lunettes ophtalmiques), offre une focalisation continue de 0 à 3 dioptries, avec une épaisseur de moins de 0,5 mm et un temps de réponse de 0,5 s. Il fonctionne à basse tension (<5 V) et minimise les aberrations. Une première étude avec des sujets humains a montré une amélioration de l'acuité visuelle sur des patients atteints de presbytie, pour des objets proches (35 cm) en fonction de la puissance optique de la lentille.

En conclusion, cette thèse donne un aperçu du potentiel et des applications possible de cette nouvelle configuration de lentilles à cristaux liquides ajustables, la génération de lentilles dynamiques et modulaire à partir d'un seul dispositif avec des applications dans la correction de la presbytie et l'amélioration de la vision fovéale. Les chapitres présentés mettent en lumière la capacité de ces lentilles à offrir des solutions optiques reconfigurables et performantes, avec un contrôle précis des aberrations, du diamètre et de la position des lentilles dans de larges ouvertures.

Introduction

Cette thèse s’attache à repousser les limites des lentilles à cristaux liquides en les adaptant aux exigences des systèmes optiques de grandes ouvertures. L’enjeu est de concevoir une architecture inédite, capable d’exploiter pleinement le potentiel de l’optique adaptative, en particulier pour la correction dynamique de la vision humaine.

Contexte et enjeux

La vision est un sens fondamental permettant d’interagir avec notre environnement. Cependant, elle peut être altérée par divers défauts optiques, qu’ils soient d’origine génétique, environnemental ou acquis avec l’âge. Parmi les anomalies les plus courantes, on retrouve la myopie, l’hypermétropie, l’astigmatisme ou encore la presbytie. Ces défauts visuels affectent des milliards de personnes et nécessitent des dispositifs optiques capables de corriger à la fois la défocalisation et les aberrations astigmatiques.

Limitations des solutions actuelles.

Les lunettes et les lentilles de contact constituent aujourd’hui les solutions non invasifs les plus courantes pour corriger ces anomalies. Toutefois, leur correction statique ne permet pas de s’adapter en temps réel aux variations des conditions visuelles, telles que les changements de distance focale ou la combinaison de plusieurs défauts optiques.

Les lentilles à focalisation variable, qu’elles soient à base de liquides ou de cristaux liquides, offrent une alternative prometteuse. Grâce à leur capacité d’ajustement dynamique, elles permettent une correction adaptable et personnalisée, optimisant ainsi la vision en toutes circonstances.

Intérêt des lentilles à cristaux liquides

Dans cette thèse, nous nous concentrons sur les lentilles à cristaux liquides. Les dispositifs actuels reposent principalement sur un adressage bipolaire, ce qui limite leur flexibilité. La méthode modale, introduite par D. Love et son équipe [6], utilise une couche diélectrique transparente recouvrant une électrode circulaire. Cette configuration permet un contrôle pro-

gressif du potentiel électrique, générant un profil de phase parabolique et un effet de lentille. L'ajustement de l'amplitude et de la fréquence du signal appliqué permet de moduler la puissance optique. Cependant, la résistance de la couche semi-conductrice étant prédéfinie en fonction du diamètre de la lentille, cela impose des contraintes en termes de flexibilité et de répétabilité

Vers une approche matricielle et quadripolaire

Afin de surmonter les limitations des structures bipolaires, une nouvelle approche basée sur un champ électrique multidirectionnel a été développée. Cette architecture quadripolaire permet un contrôle électrique total de l'orientation des cristaux liquides en générant une rotation continue du champ électrique entre ses orientations transversale et longitudinale [7].

Le récent développement d'une électrode résistive transparente en forme de serpent a également permis d'améliorer la répétabilité des dépôts de couches minces [8]. Cette avancée technologique nous a conduit à la mise en place d'une matrice d'électrodes permettant de générer une lentille électriquement variable, de modifier en temps réel la taille de la pupille et de contrôler son positionnement dans la matrice. En combinant cette approche avec un contrôle de l'amplitude, de la fréquence et de la phase des signaux appliqués, il devient possible d'obtenir une modulation dynamique du front d'onde. Nous verrons que ce principe ouvre des perspectives prometteuses, pour la correction de la vision humaine, mais également pour les systèmes optiques de grande ouverture.

LES NOTIONS THÉORIQUES

1.1 Optique de l'Œil : Formation des Images et Perception

L'évaluation des aberrations optiques est primordiale dans de nombreuses applications, notamment en ophtalmologie pour le diagnostique et la correction des défauts visuels [9], en microscopie pour optimiser la résolution des images [10], les systèmes de vision optique pour la reconnaissance et l'imagerie avancée [11], ainsi qu'en photolithographie, où le contrôle précis des aberrations est essentiel à la fabrication des composants électroniques [2]. Une compréhension de ces aberrations est essentielle, elles permettent de prédire la résolution maximale atteignable et d'envisager des stratégies de correction adaptées. Ces corrections peuvent être effectuées soit de manière active, grâce à l'optique adaptative, soit de manière passive, via des techniques de déconvolution d'image après acquisition [12].

Parmi les systèmes optiques de référence, l'œil humain joue un rôle fondamental dans la perception de notre environnement. En tant que système optique biologique, il présente des caractéristiques singulières qui inspirent directement la conception et l'amélioration de nombreux dispositifs optiques. Néanmoins, comme tout organisme vivant sa morphologie et le vieillissement des tissus varie d'un individu à l'autre et peuvent être à l'origine de défauts dans la qualité de vision [13]. Identifier et corriger les aberrations intrinsèques de l'œil est un enjeu clé pour l'amélioration de la vision et le développement de nouvelles technologies correctrices [14]. Nous présenterons les principaux éléments optiques de l'œil, servant d'introduction à l'étude des aberrations optiques.

L'œil est constitué de plusieurs composants optiques pour focaliser la lumière sur la rétine. Les principaux composants optiques de l'œil décrits dans la figure 1.1, comprennent, la cornée, une lentille ($n \approx 1.37$) à l'avant de l'œil en forme de ménisque contribue à environ 70% de la puissance réfractive totale de l'œil ($\approx 40 D$). Elle sert de première surface de focalisation pour les rayons lumineux entrant dans l'œil. Ensuite, le cristallin, une lentille biconvexe flexible responsable de l'accommodation. C'est la capacité de l'œil à ajuster la focalisation des objets

à différentes distances, la tension des muscles entourant la capsule du cristallin provoque une déformation du cristallin, augmentant ainsi sa puissance optique (de 10 à 30 D chez un jeune, mais devient progressivement fixe après l'âge de 45 ans [15]). Située entre la cornée et le cristallin, l'iris, un diaphragme ajustable en fonction de la quantité de lumière environnante, joue le rôle de pupille d'entrée du système optique. Les humeurs aqueuse et vitrée, des liquide visqueux, remplissent la majeure partie de l'œil et aident à maintenir la pression intraoculaire et la forme de l'œil. Pour finir, l'image se forme sur la rétine (environ 24 mm derrière la cornée), où un degré d'angle visuel correspondant à une distance de 290 μm sur la rétine [16].

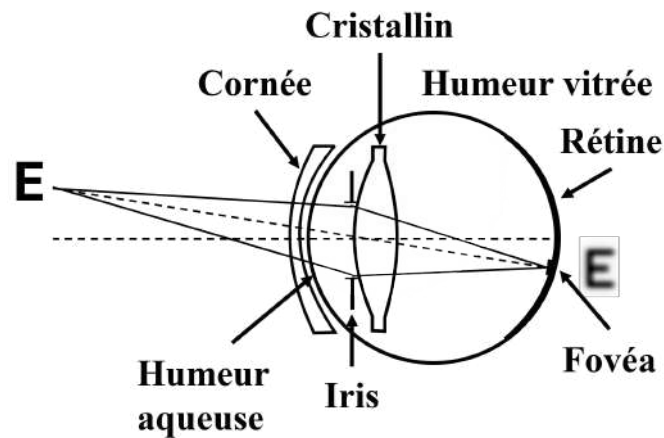


FIGURE 1.1 – Schéma du système optique de l'œil humain.

L'image est captée par des photorécepteurs organisés en mosaïques, analogue aux pixels de caméra, dont les caractéristiques définissent la sensibilité et la résolution. La rétine contient deux types principaux de photorécepteurs : Les bâtonnets, au nombre d'environ 100 millions, sont responsables de la vision en faible intensité et sont concentrés en périphérie. Ils mesurent environ 1,5 μm de diamètre et atteignent leur densité maximale ($\approx 160\,000/\text{mm}^2$) dans une région de 20 degrés autour de la fovéa [17]. Les cônes, environ 20 fois moins nombreux, assurent la vision en couleur et les détails [1]. Ils se concentrent dans la fovéa, la région centrale où la résolution spatiale atteint son maximum [18]. Avec un diamètre de 1.5 μm , ils sont espacés de 2 μm . Leur diamètre et leur espacement augmentent en s'éloignant de la fovéa, où ils se mélangent aux bâtonnets [17]. Il existe trois types de cônes, chacun sensible à une gamme de longueurs d'onde, cônes S : pic à 420 nm (bleu), cônes M : pic à 531 nm (vert), cônes L : pic à 588 nm (rouge), ce qui permet la perception des couleurs.

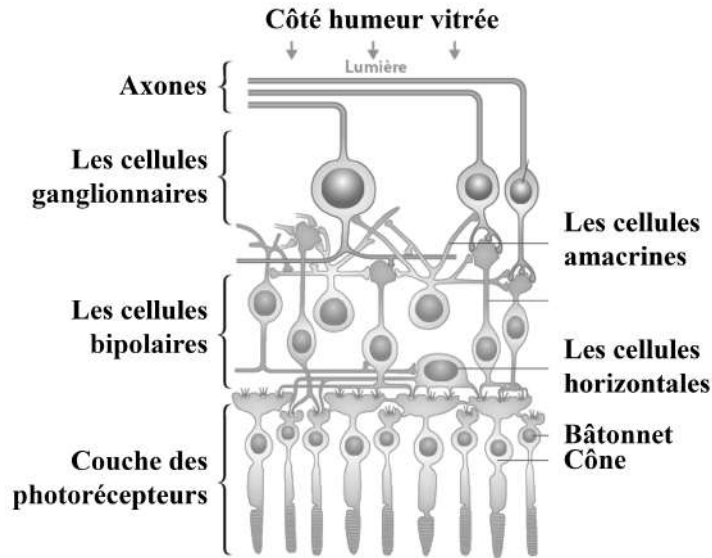


FIGURE 1.2 – Schéma de l'organisation cellulaire de la rétine, basé sur [1].

Malgré sa conception optique minimaliste, la vision est un ensemble de processus complexe qui ne se limite pas à la formation d'une image sur la rétine ; elle implique un traitement neuronal sophistiqué. Nous nous contenterons d'en présenter les grandes lignes ; Après la capture de la lumière par les photorécepteurs, l'information est traitée par différentes couches cellulaires de la rétine avant d'être transmise au cortex via le nerf optique. Ce traitement repose sur deux voies principales [1] : une voie directe, où le signal des photorécepteurs est relayé par les cellules bipolaires vers les cellules ganglionnaires, et une voie indirecte impliquant les cellules horizontales et amacrines, qui génère des inhibitions latérales, amplifiant la perception des contrastes. Les cellules bipolaires et ganglionnaires possèdent des champs récepteurs où elles reçoivent simultanément des signaux directs et opposés des photorécepteurs environnants, ce qui permet à l'œil de détecter essentiellement les variations d'intensité lumineuse plutôt que les niveaux absolus de lumière. Ce mécanisme varie selon l'excentricité et le niveau de lumière : dans la fovéa, chaque cône est relié à une seule cellule ganglionnaire, assurant une haute résolution spatiale, alors qu'en périphérie, plusieurs photorécepteurs convergent vers une même cellule ganglionnaire, favorisant la sensibilité au détriment de la précision. Par conséquent, l'étude conjointe des aberrations optiques et de la sensibilité neuronale est essentielle pour comprendre les limites et les performances du système visuel humain qui varie d'un individu à l'autre.

Ici, nous aborderons les défauts de réfraction qui affectent la vision en altérant la formation des images sur la rétine. Parmi les plus courants, on retrouve la myopie, l'hypermétropie, l'astigmatisme et la presbytie. La myopie, est due à un œil trop long ou à une courbure excessive de la cornée, provoquant une focalisation devant la rétine. En conséquence, les objets éloignés apparaissent flous, tandis que la vision de près reste nette. Ce défaut est généralement corrigé

par des lentilles concaves, recule le point focal vers la rétine. À l'inverse, l'hypermétropie résulte d'un œil trop court, entraînant une focalisation derrière la rétine. Cela entraîne une vision floue des objets rapprochés, tandis que la vision de loin peut rester claire. La correction s'effectue à l'aide de lentilles convexes, qui permettent de ramener l'image sur la rétine. L'astigmatisme, résulte d'une irrégularité dans la courbure de la cornée ou du cristallin. Cette anomalie empêche la lumière de converger en un seul point, provoquant une vision floue ou déformée, quel que soit le plan focal. Il est corrigé grâce à des lentilles cylindriques, qui compensent les différences de courbure. Enfin, avec l'âge, le cristallin perd progressivement de sa flexibilité, réduisant la capacité de l'œil à s'accommoder pour voir des objets proches. Ce phénomène, appelé presbytie, apparaît généralement après 40 ans et est corrigé à l'aide de lunettes progressives ou de lentilles bifocales, qui permettent d'adapter la mise au point selon la distance d'observation.

Les méthodes classiques d'évaluation des troubles visuels reposent sur des tests en dioptrie et des échelles d'acuité visuelle comme celle de Snellen [19]. Cette notion sera décrite plus en détail dans le chapitre 4. Elle représente la capacité de l'œil à discerner des détails fins, un aspect fondamental de la perception. Une acuité visuelle dite "normale" correspond à la capacité de distinguer deux points séparés par un angle (MAR) d'une minute d'arc, ce qui équivaut à une vision 10/10. Cette résolution est maximale au niveau de la fovéa, qui couvre un champ visuel d'environ $1,25^\circ$, mais diminue rapidement au-delà, en raison de la réduction de la densité des photorécepteurs et de l'augmentation des aberrations optiques (fig.1.3).

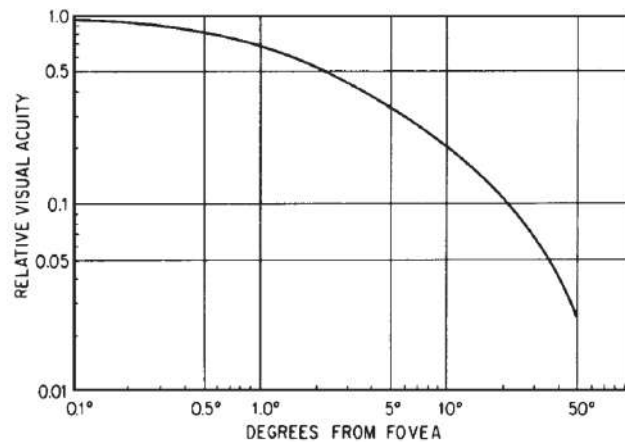


FIGURE 1.3 – Acuité visuelle en fonction de la position de l'image sur la rétine [2]

Les défauts de réfraction influencent directement l'acuité visuelle en altérant la formation de l'image sur la rétine. Une image floue entraîne une diminution de la résolution et une réduction du contraste, affectant ainsi la perception des détails fins. La quantification précise de ces défauts est essentielle pour optimiser la correction de la vision et améliorer l'acuité. Si les méthodes classiques, comme la mesure en dioptries et l'acuité visuelle sur l'échelle de Snellen [20, 19], permettent une première évaluation des troubles visuels, elles restent limitées pour

détecter des aberrations plus complexes. Des méthodes plus avancées sur l'analyse du front d'onde s'appuyant sur des outils mathématiques offrent une mesure détaillée et précise des défauts optiques [12].

1.2 Notion de Front d'Onde et Aberrations Optiques : Analyse et Correction

1.2.1 Décomposition du Front d'Onde à l'Aide des Polynômes de Zernike

La déviation optique d'un front d'onde plan ou sphérique de référence est décrite comme une aberration. Lors de l'analyse et de la correction des performances optiques d'un système tel que l'œil humain, les polynômes de Zernike (Z_i) représentent mathématiquement les aberrations du front d'onde, y compris celles qui se produisent naturellement dans l'œil humain. Les données collectées peuvent être décomposées en coefficients de Zernike (a_i), qui quantifient l'ampleur de chaque type d'aberration. Comprendre et mesurer ces aberrations est essentiel pour des applications telles que la conception de lentilles correctrices et l'amélioration de l'acuité visuelle, et l'optimisation des systèmes d'imagerie adaptative [14]. Les polynômes de Zernike forment une série de polynômes orthogonaux définis sur un cercle unitaire, ce qui signifie qu'ils permettent une décomposition sans redondance des aberrations optiques [21]. Ils permettent donc de décrire les aberrations sur des ouvertures circulaires, telle que la pupille de l'œil. Chaque polynôme de Zernike correspond à un type spécifique d'aberration, permettant une caractérisation détaillée des erreurs de front d'onde (W). Exprimé en coordonnées cartésiennes (x, y) ou polaire (ρ, θ) avec $\rho = \sqrt{x^2 + y^2}$ la coordonnées radiales et $\theta = \arctan(\frac{y}{x})$ angulaires :

$$W(\rho, \theta) = \sum_{i=0}^{\infty} a_i Z_i(\rho, \theta) \quad (1.1)$$

où, $0 \leq \rho \leq 1$ et $0 \leq \theta \leq 2\pi$, Afin de classer ces polynômes de manière structurée, on utilise une notation basée sur l'ordre radial n et la fréquence angulaire m . Ainsi, un polynôme de Zernike général peut être défini selon [21],

$$Z_i(\rho, \theta) = Z_n^m(\rho, \theta) = \begin{cases} \sqrt{2(n+1)} R_n^{|m|}(\rho) \cos(m\theta) & \text{si } m \neq 0 \text{ et } i \text{ est pair,} \\ \sqrt{2(n+1)} R_n^{|m|}(\rho) \sin(|m|\theta) & \text{si } m \neq 0 \text{ et } i \text{ est impair,} \\ \sqrt{n+1} R_n^0(\rho) & \text{si } m = 0. \end{cases} \quad (1.2)$$

Cette classification permet de distinguer les termes de Zernike selon leur composante radiale et angulaire.

$$\begin{cases} n = \text{Arrondi supérieur} \left[\frac{-3 + \sqrt{9 + 8i}}{2} \right] \\ m = 2i - n(n + 2) \\ i = 0, 1, 2, \dots \end{cases} \quad (1.3)$$

Les polynômes radiaux de Zernike, notés $R_n^{|m|}(\rho)$, sont définis comme une somme finie de termes polynomiaux :

$$R_n^{|m|}(\rho) = \sum_{s=0}^{\frac{n-|m|}{2}} \frac{(-1)^s (n-s)!}{s! \left(\frac{n+|m|}{2} - s \right)! \left(\frac{n-|m|}{2} - s \right)!} \rho^{n-2s}. \quad (1.4)$$

Ces polynômes décrivent les variations du front d'onde en fonction de la distance radiale ρ normalisée sur le cercle unitaire. Enfin, pour déterminer l'amplitude des différents modes de Zernike dans le front d'onde mesuré, on effectue une projection par intégration sur la pupille :

$$a_i = \int_0^{2\pi} \int_0^1 W(\rho, \theta) Z_i(\rho, \theta) d\rho d\theta. \quad (1.5)$$

pour caractériser l'erreur totale du front d'onde par rapport à un front idéal (sans aberration), on utilise la déviation quadratique moyenne (RMS), qui est une mesure objective de la dégradation optique, σ :

$$\sigma = \sqrt{\sum_{i=0}^N a_i^2}. \quad (1.6)$$

Cette décomposition du front d'onde en polynômes de Zernike, fournit une carte détaillée de la manière dont le système optique s'écarte de la performance idéale. Dans le cadre de cette thèse, nous nous intéresserons aux aberrations de premières ordre, responsable des principales déformations du front d'onde.

Ainsi, les polynômes de Zernike permettent de modéliser et de quantifier les défauts de réfraction de l'œil, en associant chaque type d'aberration à un mode spécifique. Les défauts de réfraction classiques, comme la myopie, l'hypermétropie et l'astigmatisme, correspondent aux polynômes de bas degré ($n \leq 2$), tandis que les aberrations optiques plus complexes, telles que la coma et l'aberration sphérique, sont décrites par des polynômes de haut degré ($n \geq 3$). Par exemple, le défaut de mise au point causé par la myopie ou l'hypermétropie est associé au mode Z_2^0 , qui représente une déformation parabolique du front d'onde affectant la convergence des

j	Radial (n)	Azimutal (m)	Aberration	$Z_j(\rho^2 = x^2 + y^2)$
1	0	0	Piston	1
2	1	1	Tilt	$2\rho \sin \theta$
3	1	-1	Tip	$2\rho \cos \theta$
4	2	0	Defocus	$\sqrt{3}(2\rho^2 - 1)$
5	2	-2	Astigmatisme 45°	$\sqrt{6}\rho^2 \sin 2\theta$
6	2	2	Astigmatisme 0°	$\sqrt{6}\rho^2 \cos 2\theta$
7	3	1	Coma y	$\sqrt{8}(3\rho^3 - 2\rho) \sin \theta$
8	3	-1	Coma x	$\sqrt{8}(3\rho^3 - 2\rho) \cos \theta$
9	3	3	Trefoil y	$\sqrt{8}\rho^3 \sin 3\theta$
10	3	-3	Trefoil x	$\sqrt{8}\rho^3 \cos 3\theta$
11	4	0	Aber. sphérique	$\sqrt{5}(6\rho^4 - 6\rho^2 + 1)$

TABLE 1.1 – Polynômes de Zernike et leurs aberrations associées

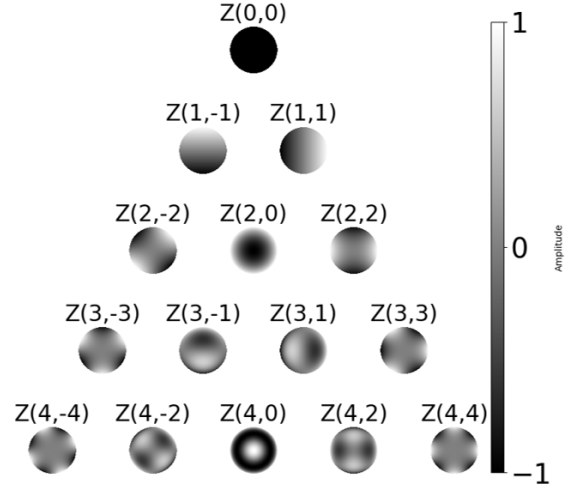


TABLE 1.2 – Illustration des polynômes de Zernike

rayons lumineux sur la rétine. De même, l'astigmatisme, qui entraîne une déformation directionnelle de l'image, est modélisé par les modes $Z_2^{\pm 2}$, caractérisant une courbure asymétrique de la cornée ou du cristallin.

Ces polynômes permettent ainsi une représentation plus détaillée des imperfections optiques que les simples mesures en dioptries. En identifiant précisément l'amplitude de chaque mode, il devient possible d'examiner comment ces aberrations influencent la formation de l'image sur la rétine.

1.2.2 Techniques de Mesure du Front d'Onde : Principes et Applications

Différentes techniques peuvent être utilisées pour mesurer les aberrations du front d'onde dans un système optique. Parmi elles, la détection pyramidale du front d'onde [22, 23], utilise un prisme pyramidale placée dans un plan focal conjugué. Les différences d'intensité entre les images obtenues permettent de relier ces variations aux dérivées de l'erreur du front d'onde [24], offrant ainsi une alternative aux systèmes de type Shack-Hartmann. Les mesures interférométriques, telles que l'interférométrie à cisaillement latéral, sont également utilisées pour la quantification des erreurs optiques [25]. Ces techniques permettent d'obtenir une mesure globale du front d'onde avec une résolution élevée, bien que leur mise en oeuvre soit souvent plus exigeante en termes de stabilité et d'alignement [26].

Une méthode simple et largement répandue pour quantifier les déformations du front d'onde d'un système optique (notamment l'œil) est d'utiliser un analyseur de front d'onde Shack-Hartmann (SH) [27]. Le principe repose sur l'échantillonnage du front d'onde à l'aide d'un réseau de micro-lentilles positionné dans un plan conjugué de la pupille, là où l'erreur de front d'onde doit être mesurée. Chaque micro-lentille focalise localement le front d'onde dévié sur

une caméra (généralement une caméra CCD) placée dans son plan focal [28]. Les rayons étant perpendiculaires au front d'onde, si celui-ci est localement approximé par un plan incliné, la figure illustre ce procédé 1.4, le déplacement de chaque point de focalisation par rapport à une référence est proportionnel à la pente locale du front d'onde [29].

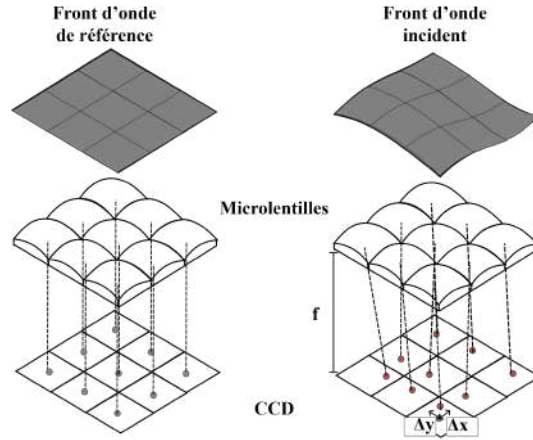


FIGURE 1.4 – Représentation 3D de l'échantillonnage du front d'onde à l'aide d'une matrice de microlentilles d'un Shack-Hartmann

Un front d'onde plan produit une grille de points focaux uniformément espacés, tandis qu'un défaut du front d'onde crée une grille désordonnée (la figure 1.4 présente un schéma en 3 dimension). La pente locale du front d'onde est déduite des déplacements grâce à la formule suivante :

$$\begin{cases} \left. \frac{\partial W(x,y)}{\partial x} \right|_{\substack{x=x_i \\ y=y_i}} = \frac{\Delta x_i}{f} \\ \left. \frac{\partial W(x,y)}{\partial y} \right|_{\substack{x=x_i \\ y=y_i}} = \frac{\Delta y_i}{f} \end{cases} \quad (1.7)$$

Avec i représentant la lentille considérée, f la distance focale des microlentilles, et Δx_i , Δy_i les déplacements des points focaux mesurés derrière une microlentille sur la caméra CCD.

Pour reconstruire $W(x,y)$, qui décrit la surface complète du front d'onde, les pentes doivent être intégrées [30]. Cette intégration permet de reconstituer la forme du front d'onde à partir de ses dérivées partielles. Une approche courante consiste à projeter les pentes mesurées sur une base de polynômes de Zernike, dont les dérivées définissent les pentes théoriques du front d'onde. La reconstruction consiste à déterminer les coefficients a_i qui minimisent l'écart entre les pentes mesurées et les pentes théoriques. Cette minimisation repose sur une approche des moindres carrés, qui ajuste les coefficients de Zernike de manière à réduire l'erreur quadratique moyenne entre les pentes mesurées et celles modélisées par les polynômes de Zernike.

1.2.3 Impact du Front d'Onde sur la Qualité de l'Image Rétinienne

Suite aux mesures des coefficients d'amplitude des polynôme de Zernike et la reconstruction du front d'onde $W(\rho, \theta)$, il est possible d'estimer la résolution du système optique. Cette estimation repose sur la réponse du système optique à un point source situé à l'infini, qui permet de déterminer la fonction d'étalement du point (PSF). La forme de la PSF est directement influencées par la présence d'aberrations optique. En particulier, sa largeur fournit une indication sur la résolution spatiale du système. Pour décrire mathématiquement cette PSF [31], La fonction complexe de la pupille est noté :

$$P(\rho, \theta) = A(\rho, \theta) e^{-iW(\rho, \theta)} \quad (1.8)$$

où $A(\rho, \theta)$ est la fonction de transmission d'amplitude de la pupille et $e^{-iW(\rho, \theta)}$ représente les déphasages introduits par les aberrations du front d'onde. En supposant une pupille circulaire de rayon r_0 , la fonction d'ouverture est donnée par [32] :

$$A(\rho, \theta) = \begin{cases} 1, & \text{si } \rho < r_0. \\ 0, & \text{si } \rho > r_0. \end{cases} \quad (1.9)$$

Ici, la fonction complexe de la pupille $P(\rho, \theta)$ est décrite, La PSF du système optique peut être obtenue en calculant le module carré de la transformée de Fourier de la fonction pupille [31] :

$$PSF(u, v) = |\mathcal{F}\{P(\rho, \theta)\}|^2 \quad (1.10)$$

En l'absence d'aberrations et lorsque la pupille de sortie est circulaire, la distribution d'intensité suit la fonction du disque d'Airy, dont le premier minimum se situe à un angle donné :

$$\alpha = 1.22 \frac{\lambda}{D} \quad (1.11)$$

Avec D le diamètre de la pupille. Pour un diamètre de pupille de 3mm et une longueur d'onde de 550nm, un point source à l'infini est imagé sur la rétine avec un angle de 46" arc seconde, ou 4 μm [33]. Cette valeur correspond à la plus petite distance distinguable entre deux objets au travers du système optique.

Par conséquent, la PSF du système s'élargit avec la présence d'aberrations, et la qualité d'image est dégradée. l'intensité maximal de la PSF est réduite et redistribuée autour. dans ce cas, le ratio d'intensité au centre de la PSF avec et sans aberrations s'exprime tel que :

$$S = 1 - \left(\frac{2\pi}{\lambda} \right)^2 \sigma^2 \quad (1.12)$$

Où σ est l'erreur moyen du front d'onde (RMS), eq.1.6.

La valeur de S fait référence au ratio de Strehl. Ici pour de petites abberations, σ peut être directement relié à la qualité d'image. Un critère de qualité d'image définis par Maréchal (1947) considère un système optique au limite de diffraction lorsque le ratio de Strehl est au dessus de 0.8 ou σ inférieur à $\lambda/14$. En complément de l'analyse de la PSF, il est essentiel d'examiner la fonction de transfert de modulation (MTF), qui permet d'évaluer la capacité du système optique à transmettre les détails d'une image en fonction de leur fréquence spatiale. La MTF est dérivée du module de la fonction de transfert optique (OTF) qui représente la réponse fréquentielle d'un système optique, obtenue par transformée de Fourier de la PSF [3].

$$MTF = |\mathbf{OTF}| = |\mathcal{F}\{PSF\}| \quad (1.13)$$

Cela signifie que plus la PSF est large, plus la MTF est réduite, traduisant une perte de contraste à haute fréquence spatiale [3]. La MTF donne le rapport de la modulation de l'image d'un réseau à celle de l'objet, en fonction de la fréquence spatiale du réseau. Elle peut être interprétée comme l'atténuation du contraste ou la sensibilité au contraste du système. la modulation est définie par le rapport suivant, qui mesure la variation de contraste :

$$MTF = \frac{I_{\max} - I_{\min}}{I_{\max} + I_{\min}} \quad (1.14)$$

où I_{\max} et I_{\min} sont les intensités maximales et minimales du motif testé. Dans l'œil humain, la MTF est fortement influencée par la taille de la pupille et les aberrations optiques, comme le montrent les mesures réalisées par Campbell et Gubisch (1966), qui ont étudié la MTF pour différentes tailles de pupilles [3].

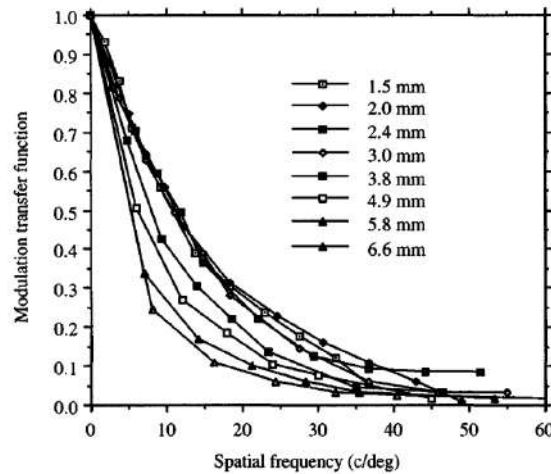


FIGURE 1.5 – Mesures des MTF en lumière blanche de l'œil, réalisées par Campbell et Gubisch (1966), pour une gamme de diamètres pupillaires. Moyenne de trois sujets [3]

De ce fait, en corrigeant les aberrations, notamment celles de bas ordre, il est possible d'améliorer significativement ses performances, l'acuité visuelle, la sensibilité au contraste, et la performance visuelle globale. L'œil humain est un système optique vivant et dynamique. Contrairement à des lentilles ou systèmes optiques rigides, il est influencé par des facteurs environnementaux et de vieillissement des tissus. Ces variations provoquent des aberrations optiques, qui altèrent la qualité de la vision. Aujourd'hui, les lunettes ou les lentilles de contacts corrigent les aberrations simples (défocalisation, astigmatisme primaire) et restent statiques. Ce qui peut nécessiter plusieurs paires de lunettes ou des lunettes progressive des lors que l'on souhaite observer des objets proches ou lointain. Pour répondre aux multiples situations rencontrées par l'œil, il est indispensable d'utiliser des solutions adaptatives capables de s'ajuster aux fluctuations de l'œil vivant. Avec les progrès technologiques, la correction précise de ces aberrations continue de s'améliorer. Les technologies de miroirs déformables et de cristaux liquides (SLM) représentent des avancées majeures dans le contrôle du front d'onde. D'autres technique de correction permanente existe comme Lasik, une chirurgie réfractive pour remodeler précisément la cornée utilise les données des aberrations de Zernike. Néanmoins, cette méthode en plein essor reste invasive.

1.2.4 Correction des Aberrations Optiques par Optique Adaptative

La compensation dynamique des aberrations dans un système optique est appelée optique adaptative. Cette approche à vue le jour en astronomie, avec l'utilisation d'un miroir déformable pour corriger certaines aberrations causés par l'atmosphère [34]. C'est en 1997 que la première correction statique des aberrations de l'œil à l'aide d'un miroir déformable et d'un capteur de front d'onde a été réalisée [14]. Cela a été suivi par des corrections dynamiques qui ont permis une amélioration significative de la résolution des images rétinienne [35, 36]. Aujourd'hui, les deux principaux correcteurs de front d'onde sont basés sur la réflexion avec les miroirs déformables qui utilisent des ajustements mécaniques pour moduler le chemin optique et la transmission avec les modulateurs de phase à cristaux liquides (Spatial light modulator SLM) qui module la phase de l'onde via un contrôle local de l'indice de réfraction.

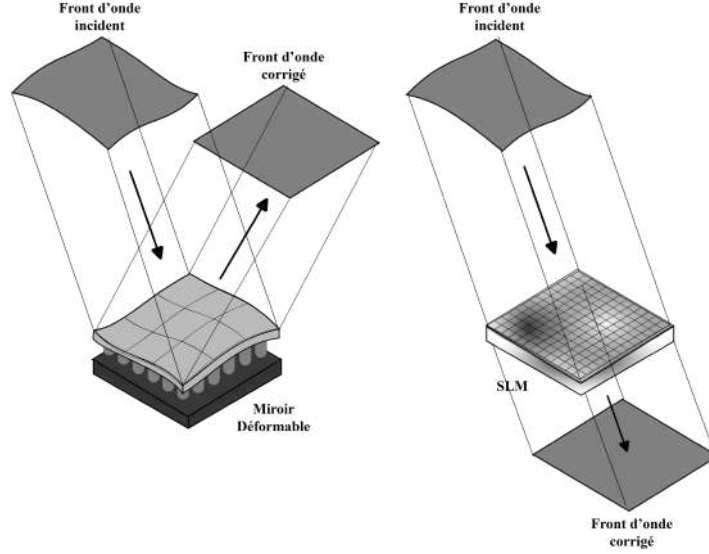


FIGURE 1.6 – Représentation schématique de la correction du front d’onde en réflexion à l’aide d’un miroir déformable et en transmission à l’aide d’un SLM

Parmis les miroirs déformables, la surface de ces derniers peuvent être segmenté ou continus. Bien que miniaturisés grâce aux technologies MEMS et LCD, ces dispositifs restent coûteux, encombrants, nécessitent des hautes tensions, et posent des défis d’intégration dans les systèmes sans fils. Pour dépasser ces limitations, une lentille ajustable à cristaux liquides segmentée (TLCL-s) a été développée par notre équipe [37, 38] : elle génère un profil d’indice de réfraction complexe et sans pixellisation grâce à des tensions appliquées sur des électrodes périphériques. Plus récemment, cette lentille a démontré ses performances dans des systèmes optiques plus complexe tel que l’endo-microscopie [39]. Cependant, cette efficacité bien que démontrée, reste limité au systèmes optique de petite ouverture. Le but de cette thèse est donc de développer et concevoir une lentille à cristaux liquide capable de moduler le front d’onde dans le but de concerver les avantages de la TLCL-s tout en travaillant sur des systèmes de grandes ouverture. Avant d’ouvrir sur le sujet de recherche, nous présenterons les propriétés des cristaux liquides et le principe de fonctionnement des lentilles ajustables à cristaux liquides.

1.3 Cristaux Liquides : Structure, Phases et Propriétés Électro-Optiques

Les cristaux liquides (CL) ont été découverts pour la première fois à la fin du XIXe siècle par Friedrich Reinitzer, un botaniste autrichien [40]. En chauffant une substance ressemblant au cholestérol, appelée benzoate de cholestéryl, Reinitzer a constaté que celle-ci passait d’abord à l’état de liquide trouble avant de se cristalliser en refroidissant. Cette découverte a révélé l’existence d’états intermédiaires entre les solides cristallins et les liquides isotropes, que le scientifique Otto Lehmann a désignés sous le nom de mésomorphes ou mésophases. Ce n’est

toutefois qu'en 1968, soit près de quatre-vingts ans plus tard, que le premier écran à cristaux liquides, tel que nous le connaissons aujourd'hui, a été mis au point [41].

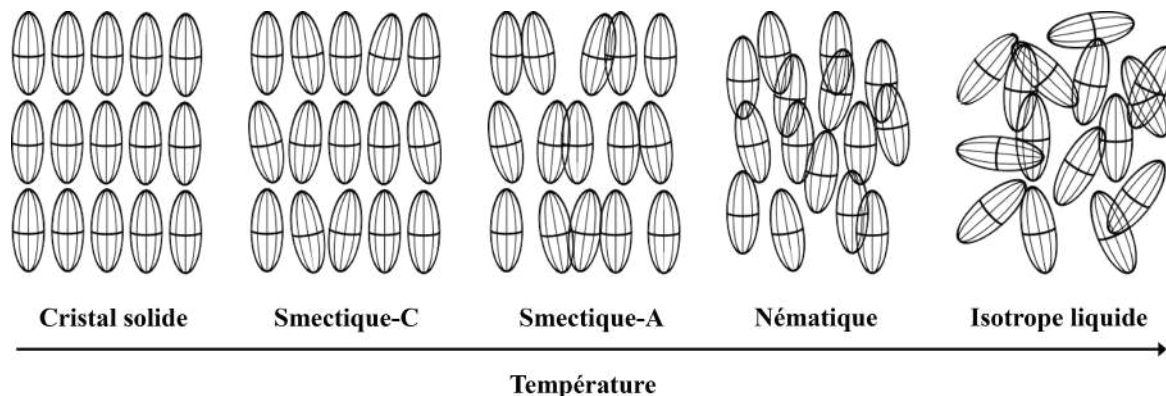


FIGURE 1.7 – Représentation des mesophases des molécules en formes de batonnets (basé sur [4])

Les mesophases sont une phase de la matière intermédiaire entre les solides cristallins et les liquides isotropes. En ce sens, ils présentent des caractéristiques de ces deux phases. Les cristaux sont caractérisés par un ordre à longue portée à la fois dans la position et l'alignement moléculaires, tandis que les liquides isotropes ne présentent que des ordres à courte portée et sont invariants en rotation et en translation à l'échelle macroscopique. Les molécules LC, ou mésogènes, présentent un certain nombre de modes d'ordre à longue distance avec un degré semi-continu à travers des mécanismes de température (thermotropes), de concentration (lyotropes) et de composition moléculaire (metallotropes). Les cristaux liquides (LC) sont des composés organiques que l'on peut visualiser comme un assemblage de molécules fortement allongées. ils se présentent sous la forme d'un ensemble de molécules en forme de bâtonnets (calamitiques), courbés (forme de banane) ou de disques (discotique) de quelques nanomètres [4]. Les mésogènes discotiques sont capables d'un ordre colonnaire bidimensionnel, tandis que les mésogènes en forme de bâtonnet présentent un ordre orienté et de translation unidirectionnelle, comme indiqué dans la figure 1.7.

Au cours de ces travaux, nous nous concentrerons sur les mésogènes thermotropes qui présentent une forte anisotropie physique et dont les transitions de phase sont régies par la température. A basse température ces LC forment des solides cristallins conventionnels, transitant par de multiples phases intermédiaires ou mésophases jusqu'à un liquide isotrope avec l'augmentation de la température. La figure 1.7 illustre la dépendance de la température des mésophases thermotropes. À basse température, les phases smectiques sont caractérisées par la présence d'un ordre directionnel et positionnel de dimension inférieure à celle de la phase cristalline ; les molécules de LC s'alignent dans des plans réguliers qui sont isotropes en position à l'intérieur d'eux même. Lorsque l'on fait varier la température dans la gamme smectique, l'orientation moléculaire (communément appelée directeur n) passe d'un plan à l'autre. Tran-

sition de phase inclinée (Smectic C) à perpendiculaire (Smectic A) par rapport aux plans moléculaires. Avec l'ajout d'une énergie thermique supplémentaire, l'ordre positionnel disparaît et génère une phase nématique, caractérisé par un ordre directionnel mais non positionnel. Les propriétés fluidiques varient énormément entre mesophases. Avec une isotropie positionnel la phase nématique à une viscosité très faible. Si la température continu d'augmenter, l'ordre directionnel et positionnel seront perdu et le mésogène devient désordonné, entrant dans une phase liquide isotrope conventionnelle. Notre intérêt se portera sur les CL nématique, qui existe à température ambiante capital pour la plupart des technologies LC.

1.3.1 Propriétés physique des cristaux liquides nématiques (NLC)

L'organisation moléculaire et l'anisotropie physique des mésophases nématiques leur confèrent des propriétés uniques à l'échelle macroscopique. Le maintien de cette anisotropie géométrique importante, nécessite une structure molécules qui est à la fois allongée et rigide. Les Cristaux liquides nématique à température ambiante sont généralement constitués de longues chaînes aliphatiques qui donnent une forme étendue et flexibles qui procure une mobilité entre molécules et de composants aromatiques au centre qui donnent de la rigidité et assurent la polarisation de la molécule. En général, une condition essentielle qui doit être remplie est que la longueur de la molécule soit supérieure à son diamètre. De plus, dans le cas où la partie rigide est polaire et la partie flexible apolaire, le mésogène est amphiphile.

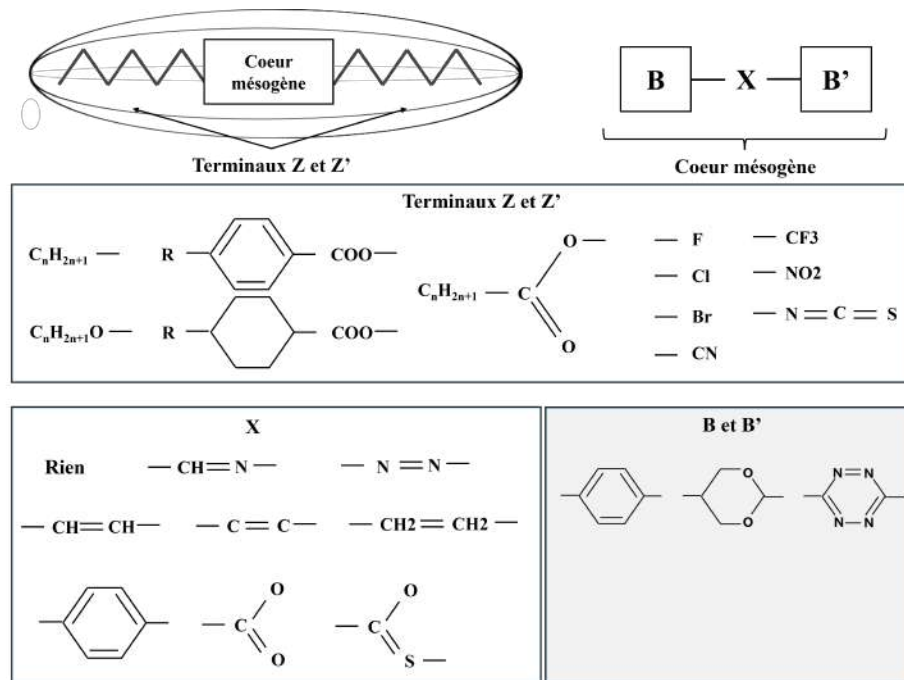


FIGURE 1.8 – Morphologie des mésogènes conduisant à des mésophases thermotropes [5]

L'orientation des molécules le long du directeur n peut être définie expérimentalement soit

en appliquant un champ électrique externe (décrit dans la section suivante), soit en imposant des conditions aux substrats de la cellule de LC, connues sous le nom de conditions d'ancrage. Il consiste à piéger les molécules en contact avec les surfaces dans une direction choisie, afin de maintenir, en l'absence de champ, les molécules alignées. Les conditions d'ancrage typiques pour une cellule de cristal liquide peuvent être soit planaires simples (\vec{n} parallèle aux substrats), torsadées (combinaison de deux conditions d'ancrage planaires dans des directions différentes dans le plan du substrat), soit homéotropes (\vec{n} orthogonal aux plaques confinantes), voir Figure 1.9.

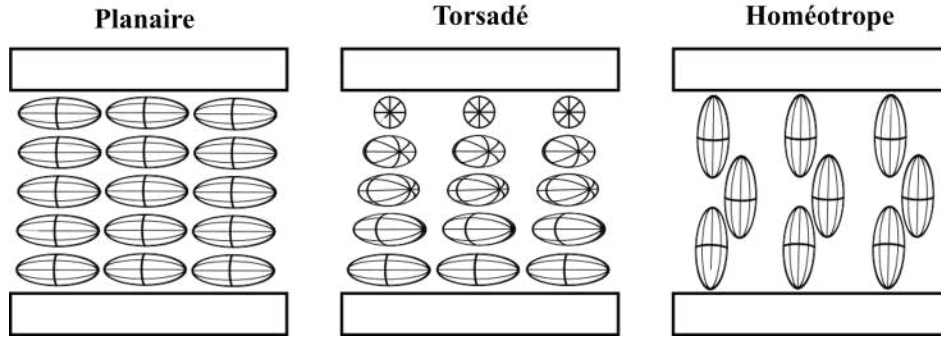


FIGURE 1.9 – Représentation des différents type d'ancrage, planaire, planaire twisté et homéotrope

Notre intérêt se portera sur l'alignement planaire, obtenue par frottement d'une couche mince de polymère, typiquement du polyimide (PI) ou de l'alcool polyvinylique (PVA), dont la structure à longue chaîne se prête à un ré-arrangement par frottement abrasif. Cet ancrage crée une force de maintien ou de rappel lorsque une perturbation extérieure est appliquée (champ électrique, magnétique, etc.). Néanmoins, c'est cet effet "moutonnier" des mésophases, lié aux forces élastiques intrinsèques, qui leur confèrent des propriétés uniques : il suffit de contraindre la direction d'orientation de quelques molécules pour engendrer la réorientation des autres molécules voisines dans cette même direction. Une façon de quantifier l'énergie élastique présente dans le système est de premièrement calculer la densité d'énergie élastique occasionnée par les différents types de déformations que subissent les molécules anisotropes. Dans un volume fixe de CL nématiques uniaxiaux, la densité d'énergie élastique totale f_e est donnée par la relation de Frank-Oseen suivante [42, 43]. Il suffit d'intégrer cette densité d'énergie libre f_e sur tout le volume des molécules afin d'obtenir l'énergie totale libre W_e

$$f_e = \frac{1}{2}K_1(\nabla \cdot \vec{n})^2 + \frac{1}{2}K_2(\vec{n} \cdot (\nabla \times \vec{n}))^2 + \frac{1}{2}K_3(\vec{n} \times (\nabla \times \vec{n}))^2 \quad (1.15)$$

$$W_e = \int f_e \partial V \quad (1.16)$$

Le vecteur unitaire \vec{n} oriente les molécules selon l'axe d'anisotropie. Les déformations du milieu,

telles que l'évasement, la torsion et la flexion, sont décrites dans la figure 1.10 par les termes $K_1(\text{div}(\vec{n}))^2$, $K_2(\vec{n} \cdot \vec{\text{rot}}(\vec{n}))^2$ et $K_3(\vec{n} \wedge \vec{\text{rot}}(\vec{n}))^2$, respectivement.

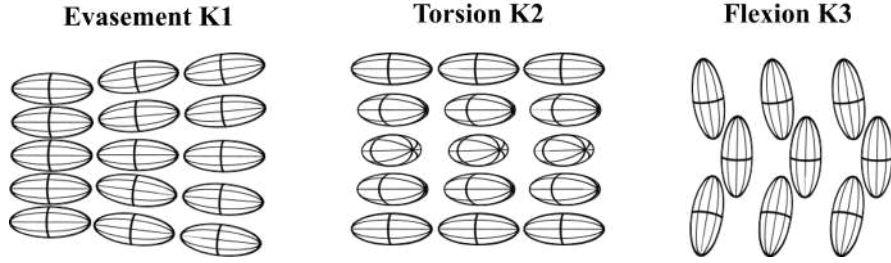


FIGURE 1.10 – Schéma des différentes déformations de l'axe du directeur n

Ces déformations augmentent l'énergie libre du système et s'opposent au couple généré par un champ électrique (décrit plus tard). Les constantes K_1 , K_2 et K_3 sont les constantes d'élasticité associées, influencées par la structure chimique des cristaux liquides.

Maintenant, si l'on considère une cellule en deux dimensions, que le directeur $n_x = \cos \theta$, $n_y = \sin \theta$, $n_z = 0$ et $\frac{\delta n}{\delta z} = 0$, on peut réduire l'équation 1.15. En approximant les constantes élastiques, tel que $K_1 = K_3 = K$ et considérant que l'angle d'ancrage des CL est quasi-plan, θ est petit, tel que $\cos \theta \approx 1$ et $\sin \theta \approx 0$. On obtient :

$$f_e = \frac{1}{2}K \left[\left(\frac{\partial \theta}{\partial y} \right)^2 + \left(\frac{\partial \theta}{\partial x} \right)^2 \right] \quad (1.17)$$

Pour minimiser l'énergie élastique, les molécules doivent s'orienter parallèlement les unes par rapport aux autres.

1.3.2 Réponse des NLC à un Champ Électrique

Le couple électrique

L'un des principaux intérêts des cristaux liquides réside dans leur réponse à un champ électrique appliqué. Le directeur nématique peut être facilement orienté en appliquant quelques volts à travers la couche de cristal liquide. Lorsque les molécules se réorientent, les propriétés optiques de la couche de cristal liquide changent radicalement. Lorsqu'un champ électrique E est appliqué à un cristal liquide nématique, il induit une polarisation P qui dépend de l'orientation du directeur du cristal liquide par rapport à la direction du champ appliqué. Le couple résultant engendre une rotation perpendiculaire à E , centrée sur la molécule [44]. Par conséquent, les molécules s'orienteront de manière à minimiser le couple et équilibrer l'énergie électrique.

Pour un cristal liquide nématique, le tenseur de permittivité $\bar{\epsilon}$ dans le système de coordonnées

aligné avec le directeur $(0, n, n_\perp)$ peut s'exprimer sous la forme suivante :

$$\bar{\epsilon} = \begin{bmatrix} \epsilon_{//} & 0 \\ 0 & \epsilon_\perp \end{bmatrix} \quad (1.18)$$

où $\epsilon_{//}$ est la permittivité parallèle au directeur et ϵ_\perp est la permittivité perpendiculaire au directeur. Cette anisotropie dans la permittivité est une propriété fondamentale qui permet le contrôle de l'alignement du cristal liquide via des champs externes. Lorsque le champ électrique E est appliqué, il induit une polarisation des molécules du cristal liquide en raison du déplacement des électrons le long de la direction du directeur n . Le vecteur déplacement électrique D dans ce contexte est donné par [44] :

$$D = \bar{\epsilon}E = \epsilon_0 E + P \quad (1.19)$$

Ici, ϵ_0 représente la permittivité du vide, et les composantes du champ électrique le long et perpendiculairement au directeur contribuent au déplacement total [45] :

$$\vec{D} = \epsilon_0 \epsilon_\perp \vec{E} + \epsilon_0 \Delta\epsilon (\vec{E} \cdot \vec{n}) \vec{n} \quad (1.20)$$

Ici $\Delta\epsilon = \epsilon_{//} - \epsilon_\perp$. Pour mieux comprendre le comportement des cristaux liquides nématiques sous un champ électrique, il est souvent nécessaire de considérer le cas où le directeur n'est pas aligné avec les axes de coordonnées $(0, x, y)$ de la cellule, fig.1.11.

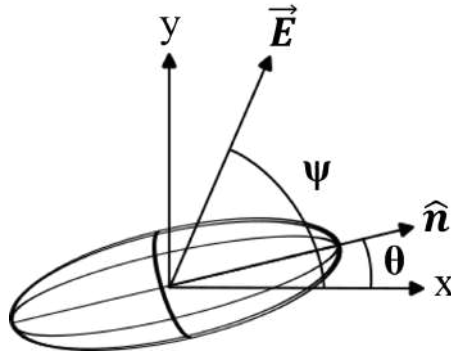


FIGURE 1.11 – Alignement du NLC suivant le champ électrique appliqué.

En effectuant une rotation du système de coordonnées d'un angle θ pour l'aligner avec le directeur, le tenseur de permittivité se transforme en conséquence. La matrice de rotation $R(\theta)$ est appliquée pour obtenir le tenseur de permittivité dans le nouveau système de coordonnées $(0, x, y)$, tel que $\bar{\epsilon}' = R(\theta)\epsilon R^T(\theta)$. Après avoir simplifié les identités trigonométriques, le tenseur de permittivité dans les nouvelles coordonnées s'exprime sous la forme :

$$\bar{\epsilon}' = \begin{pmatrix} \epsilon_\perp + \Delta\epsilon \cos^2 \theta & \frac{\Delta\epsilon}{2} \sin 2\theta \\ \frac{\Delta\epsilon}{2} \sin 2\theta & \epsilon_\perp + \Delta\epsilon \sin^2 \theta \end{pmatrix}$$

A l'aide de l'équation 1.19, la polarisation P induite par le champ électrique appliqué peut être exprimée en termes du tenseur de permittivité et du champ E , lorsque le champ électrique E est projeté dans un repère (O,x,y) , la composante du champ le long des directions x et y est exprimée $\vec{E} = \begin{pmatrix} \cos(\Psi) \\ \sin(\Psi) \end{pmatrix} E$. Cela conduit à une expression pour la polarisation sous la forme :

$$\vec{P} = \begin{pmatrix} E\Delta\epsilon(\cos^2 \theta \cos \Psi + \frac{1}{2} \sin 2\theta \sin \Psi) \\ E\Delta\epsilon(\frac{1}{2} \sin 2\theta \cos \Psi + \sin^2 \theta \sin \Psi) \end{pmatrix} \quad (1.21)$$

Ici, les constantes ϵ_0 et ϵ_{\perp} ont été simplifiées. Cette expression indique que la polarisation dépend non seulement de l'amplitude du champ électrique, mais aussi de la géométrie relative du champ par rapport au directeur, ce qui se traduit par les angles θ et Ψ .

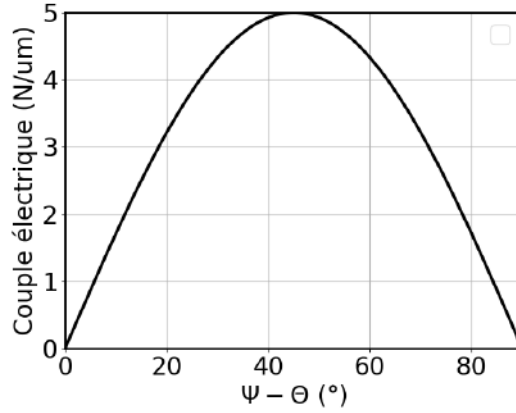


FIGURE 1.12 – Couple électrique vs l'angle θ - ψ

Le moment dipolaire résultant du couplage entre E et P génère un couple diélectrique Γ_E , qui agit pour réorienter les molécules du cristal liquide de manière à minimiser l'énergie du système. Ce couple est donné par [46] :

$$\begin{aligned} \vec{\Gamma}_E &= \vec{P} \times \vec{E} \\ &= (E\Delta\epsilon(\cos^2 \theta \cos \Psi + \frac{1}{2} \sin 2\theta \sin \Psi)).(E \sin \Psi) \\ &\quad - E\Delta\epsilon(\frac{1}{2} \sin 2\theta \cos \Psi + \sin^2 \theta \sin \Psi).(E \cos \Psi) \\ &= \frac{E^2 \Delta\epsilon}{2} \sin(2(\Psi - \theta))_y \end{aligned} \quad (1.22)$$

Le couple électrique $\vec{\Gamma}_E$, qui est proportionnel au carré du champ électrique appliqué, joue un rôle crucial dans l'alignement des molécules de cristal liquide avec le champ. Ce couple atteint son maximum lorsque l'angle Ψ - θ est de 45° , et il devient nul lorsque le champ est

perpendiculaire ou parallèle au directeur n . Dans les configurations de cellules LC, le champ E est aligné le long de l'axe y , avec un angle $\Psi = 90^\circ$. Pour que les molécules commencent à tourner, un angle d'inclinaison initial θ_i par rapport à l'axe x est nécessaire, un angle qui est obtenu grâce à des méthodes d'ancrage décrites précédemment.

Dans la plupart des cas, nous parlerons de cristal liquide possédant une anisotropie diélectrique positive ($\Delta\epsilon > 0$), les molécules tendent à s'aligner parallèlement (ou anti-parallèlement) au champ appliqué, car cela minimise l'énergie électrique. En revanche, si l'anisotropie diélectrique est négative ($\Delta\epsilon < 0$), les molécules préfèrent s'aligner perpendiculairement au champ appliqué. De plus, pour éviter les effets d'électromigration et la génération d'électricité statique qui peuvent survenir dans le cristal liquide avec un courant continu, il est nécessaire d'utiliser un courant alternatif à haute fréquence [44]. La fréquence du champ électrique appliqué peut avoir un impact significatif sur la réorientation moléculaire et la dynamique globale du cristal liquide. Par exemple, les cristaux liquides à double fréquence (détaillé plus loin) peuvent inverser le signe de leur anisotropie diélectrique en fonction de la fréquence appliquée [44]. La fréquence de croisement (f_c) correspond à la fréquence à laquelle le cristal liquide se comporte comme un milieu isotrope ($\Delta\epsilon = 0$) [44].

Par conséquent, ce champ électrique viendra contraindre les molécules. La densité d'énergie électrique du système en deux dimensions peut être exprimée en fonction du champ électrique E et du déplacement électrique D [45, 47] :

$$f_E = -\frac{1}{2}D \cdot E \quad (1.23)$$

Lorsque l'on veut exprimer la permittivité en fonction de l'orientation relative entre le champ électrique E et l'axe directeur \hat{n} , on utilise $(\theta - \Psi)$. Néanmoins, pour simplifier les démonstrations, nous réduirons le système à une dimension selon l'axe Y , basé sur un ancrage fort avec θ petit et on supposera que le champ électrique E est aligné le long d'une seule direction, le long de l'axe y , ce qui signifie que $E_x = 0$ et $E_y = E$. On obtient :

$$f_E = -\frac{1}{2}\epsilon_0\epsilon_{//}E^2 \left(1 - \frac{\Delta\epsilon}{\epsilon_{//}}\sin^2(\theta)\right) \quad (1.24)$$

Réponse statique des NLC

Transition de Freederickz :

L'énergie libre totale (W_{tot}) est la fonction qui combine les différentes formes d'énergie interne et externe présentes dans le système, permettant de prédire son comportement à l'équilibre. Ici, on considère le système statique ou quasi-statique, on néglige l'énergie cinétique. Dans un système en équilibre, l'énergie libre est minimisée, ce qui détermine la configuration stable

du système. Pour déterminer le champ électrique critique, la valeur du champ électrique pour laquelle la force électrique dépasse les forces élastiques, entraînant une réorientation des molécules.

Dans les cas d'une cellule planaire, on a la densité d'énergie total f_{tot} [4] :

$$f_{tot} = f_e + f_E = \frac{1}{2}K \left[\left(\frac{\partial \theta}{\partial y} \right)^2 + \left(\frac{\partial \theta}{\partial x} \right)^2 \right] - \frac{1}{2}\epsilon_0\epsilon_{//}E^2 \left(1 - \frac{\Delta\epsilon}{\epsilon_{//}} \sin^2(\theta) \right) \quad (1.25)$$

En minimisant la densité d'énergie total à l'aide de l'approximation d'Euler-Lagrange, nous obtenons :

$$\frac{\partial^2 \theta(y)}{\partial^2 y} - \frac{\epsilon_0 \Delta\epsilon E^2}{K} \cdot \theta = 0 \quad (1.26)$$

En assumant les conditions d'ancrage ou $\theta(0) = 0$ et $\theta(d) = 0$ avec d l'épaisseur de la cellule, la solution oscillatoire de cette équation différentielle se résume à $\theta(y) = B \sin(\lambda d) = 0$ avec $\lambda = \sqrt{\frac{\epsilon_0 \Delta\epsilon E^2}{K}}$. Pour trouver des solutions (ou $B \neq 0$) cela requiert $\lambda d = n\pi$ pour $n = 1, 2, 3, \dots$. En considérant le mode fondamental $n = 1$, on obtient la valeur du champ électrique de seuil E_c :

$$\begin{aligned} \sqrt{\frac{\epsilon_0 \Delta\epsilon E_c^2}{K}} \cdot d &= n \cdot \pi \\ E_c &= \frac{\pi}{d} \sqrt{\frac{K}{\epsilon_0 \Delta\epsilon}} \end{aligned} \quad (1.27)$$

En dessous de l'intensité critique de champ électrique, le directeur reste inchangé et conserve une orientation uniforme. Les forces élastiques de rappel, induites par un ancrage fort dominant et empêchent toute réorientation moléculaire. Cependant, au delà de cette valeur critique ($E > E_c$) le couple électrique devient prédominant, surmontant les forces élastiques et entraîne une réorientation progressive du directeur \hat{n} .

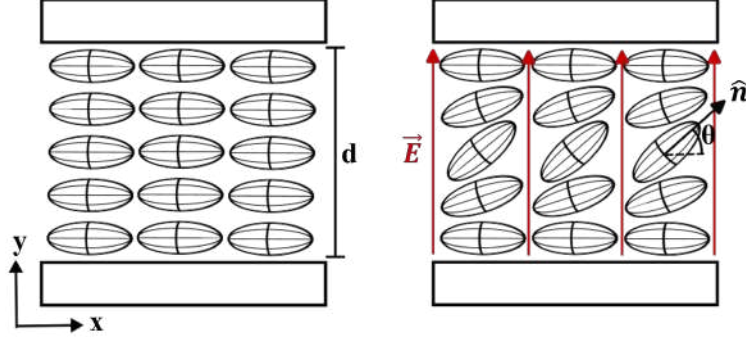


FIGURE 1.13 – Représentation des CL d’une cellule au repos (a gauche). Et leur réorientation suite à un champ électrique externe (a droite)

Une condition supplémentaire consiste que l’angle $\theta(y)$ atteigne son maximum θ_m lorsque la fonction sinus est égale à 1, c’est-à-dire lorsque l’argument du sinus est un multiple impair de $\pi/2$, qui correspond à la position $d/2$. Au final, la solution générale devient [48] :

$$\theta(y) = \theta_m \sin\left(\frac{\pi y}{d}\right) \quad (1.28)$$

Cette transition est décrite analytiquement par Yang [4, 49], où l’angle d’orientation au milieu de la cellule ($y = d/2$) suit la relation :

$$\sin \theta_m = 2 \sqrt{\frac{E - E_c}{E_c}} \quad (1.29)$$

où θ_m dépend uniquement du champ électrique E , du champ électrique de seuil E_c .

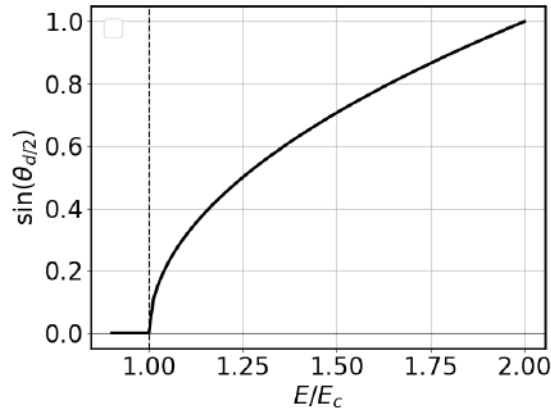


FIGURE 1.14 – Angle du directeur n au centre de la cellule en fonction du champ électrique E appliqué. Avec E_c le champ électrique de seuil.

Réponse dynamique des NLC

Jusqu'à présent, l'équilibre entre les forces élastiques des molécules et la force électrique externe a été envisagé de manière statique. Si le champ électrique externe est supprimé, les molécules reviennent à leur position initiale par relaxation, sous l'effet des forces élastiques et de la viscosité du milieu, favorisées par la géométrie d'ancrage planaire. L'analyse dynamique doit donc prendre en compte le couple visqueux, qui s'oppose à la rotation du directeur [50, 44]. Des équations, comme l'expression d'Erickson-Leslie [51, 52], ont été proposées pour décrire cette rotation dynamique avec précision. Maintenant, d'un point de vue dynamique, le temps de réponse vient de la conservation des moments de forces, dans lequel le moment élastique, visqueux et électrique sont exprimés tel que :

$$\gamma_1 \frac{\partial \theta(t)}{\partial t} = K \frac{\partial^2 \theta(y)}{\partial y^2} - \frac{1}{2} E^2 \epsilon_0 \Delta \epsilon \cdot \sin(2(\theta)) \quad (1.30)$$

avec, γ_1 le coefficient de viscosité.

Temps de relaxation :

Dans un premier temps, nous considérons la dynamique de relaxation, brusquement les molécules LC ne sont plus soumises à un champ électrique E et reviennent progressivement à leur état d'équilibre. Pour estimer le temps de relaxation (τ_{off}), on simplifie l'équation 1.30 :

$$\gamma_1 \frac{\partial \theta(t)}{\partial t} = K \frac{\partial^2 \theta(y)}{\partial y^2} \quad (1.31)$$

En reprenant la solution générale 1.28, on déduit $\frac{\partial^2 \theta(y)}{\partial y^2} = -\left(\frac{\pi}{d}\right)^2 \theta(t)$, ainsi :

$$\frac{\partial \theta(t)}{\partial t} = -\left(\frac{\pi}{d}\right)^2 \frac{K}{\gamma_1} \theta(t) \quad (1.32)$$

La solution générale de cette equation différentielle donne :

$$\theta(t) = \theta_0 \exp\left(-\frac{t}{\tau_{off}}\right) = \theta_0 \exp\left(-\left(\frac{\pi}{d}\right)^2 \frac{K}{\gamma} t\right) \quad (1.33)$$

avec $\tau = \tau_{off}$, la constante de relaxation :

$$\tau_{off} = \frac{\gamma d^2}{K \pi^2} = \frac{\gamma}{\epsilon_0 \Delta \epsilon \cdot E_c^2} \quad (1.34)$$

$\theta(t)$ décroît exponentiellement avec le temps à un tau déterminé par τ_{off} , qui dépend des paramètres physiques K , γ , et d .

Temps d'activation :

Dans un second temps, pour déterminer le temps d'activation, on applique brusquement un champ électrique en maintenant E le long de l'axe Y et θ petit, la démonstration est la même que pour τ_{off} tel que l'équilibre des forces :

$$\gamma \frac{\partial \theta}{\partial t} = K \frac{\partial^2 \theta}{\partial y^2} - E^2 \epsilon_0 \Delta \epsilon \cdot \theta \quad (1.35)$$

On obtient le temps d'activation :

$$\tau_{on} = \frac{\gamma}{\epsilon_0 \Delta \epsilon E^2 - K \frac{\pi^2}{d^2}} = \frac{\gamma}{\epsilon_0 \Delta \epsilon (E^2 - E_c^2)} \quad (1.36)$$

Par conséquent, à l'opposé du processus de désactivation, le temps de réponse lors de l'activation est influencé par l'amplitude du champ électrique. Un champ électrique plus intense accélère la réorientation des molécules. De plus, l'épaisseur du cristal liquide affecte les dynamiques tant de l'activation que de la désactivation, les cellules plus épaisses ayant pour effet de ralentir à nouveau le processus.

1.3.3 Propagation d'une onde electromagnétique dans un NLC

Des lors qu'une onde electromagnetique se propagent dans un milieu anisotrope uniaxe. Les propriétés diffèrent selon la direction de propagation par rapport a l'axe optique (ou axe y). Ils possèdent deux indices de réfraction distincts : l'indice de réfraction ordinaire (n_o) et l'indice de refraction extrordinaire (n_e).

Par conséquent, les cellules de CL présentent deux indices, n_o et n_e . L'indice de refraction du milieu sera donc different selon la direction de propagation de la lumiere, de sa polarisation et de l'orientation moleculaire.

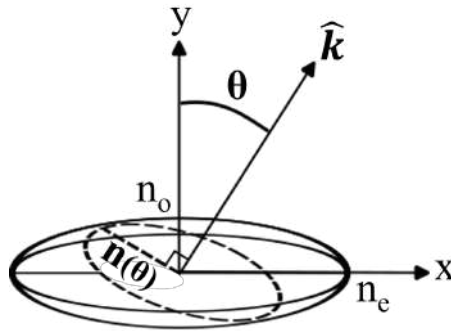


FIGURE 1.15 – Représentation de la biréfringence

La meilleure représentation de cette anisotropie d'indice est l'ellipsoïde des indices de la figure 1.15. Dans un milieu anisotrope a birefringence positive, l'indice extra-ordinaire (n_e) est orienté le long (n) de l'axe moléculaire et l'indice ordinaire (n_o) est dans le plan normal (n_\perp) a cet axe. Cet arrangement est inversé dans un milieu a birefringence négative. Dans la grande majorité des CL, la biréfringence est positive ($\Delta n = n_{//} - n_\perp = n_e - n_o$) et varie de 0.05 à 0.45 [53]. La lumière qui frappe un CL avec un angle de polarisation parallèle à l'axe optique subit un indice de réfraction effectif ($n(\theta)$) qui dépend de l'angle moléculaire (θ) avec l'axe optique (selon y).

On considère l'onde électromagnétique E se propageant sous forme d'onde plane :

$$E(r, t) = E_0 \exp i(k.r - \omega t) \quad (1.37)$$

En considérant les équations Maxwell-Ampère et Maxwell Faraday, la relation entre le vecteur d'onde et les champs électriques et magnétiques est exprimé :

$$\begin{aligned} k \times H &= -\omega \epsilon E \\ k \times E &= \omega \mu_0 H \end{aligned} \quad (1.38)$$

où k est le vecteur d'onde, ω la fréquence angulaire, et μ_0 la perméabilité du vide. En éliminant le champs magnétique H entre ces deux équations, on obtient l'équation de l'onde $k \times (k \times E) = -\omega^2 \mu_0 \epsilon E$. Une identité vectorielle standard pour le produit vectoriel double est $a \times (b \times c) = (a.c)b - (a.b)c$, on obtient :

$$k(k.E) - k^2 E = \omega^2 \mu_0 \epsilon E \quad (1.39)$$

Considérons que le vecteur d'onde k se situe dans le plan (0,x,y), les composantes de k sont donc k_x et k_y , et l'angle entre k et l'axe y est θ , avec $k_x = k \sin \theta$ et $k_y = k \cos \theta$, substituons k_x et k_y dans l'équation de l'onde et développons les termes pour chaque composante.

$$\begin{pmatrix} k_x^2 - k^2 + \omega^2 \mu_0 \epsilon_o & k_x k_y \\ k_x k_y & k_y^2 - k^2 + \omega^2 \mu_0 \epsilon_e \end{pmatrix} \begin{pmatrix} E_x \\ E_y \end{pmatrix} = 0 \quad (1.40)$$

Avec la norme du vecteur $k^2 = k_x^2 + k_y^2$, le déterminant de cette matrice est :

$$\det = \omega^4 \mu_0 \epsilon_o \epsilon_e - \omega^2 \mu_0 k^2 (\epsilon_o \sin^2 \theta + \epsilon_e \cos^2 \theta) \quad (1.41)$$

En posant $k = \frac{\omega}{c} n(\theta)$, où $n(\theta)$ est l'indice de refraction effectif pour un angle θ . De plus, pour que le déterminant soit nul (condition nécessaire pour que le système ait des solutions non triviales) et après simplification, $n_e^2 = \epsilon_e / \epsilon_o$ et $n_o^2 = \epsilon_o / \epsilon_o$, avec $c^2 = 1 / \mu_0 \epsilon_o$ on obtient :

$$n(\theta) = \frac{n_e \cdot n_o}{\sqrt{n_e^2 \cos^2(\theta) + n_o^2 \sin^2(\theta)}} \quad (1.42)$$

Cette différence d'indice entre l'onde extraordinaire et l'onde ordinaire engendre des variations de chemin optique (OPL : Optical Path Length) de la lumière en fonction de l'orientation des molécules et de la distance parcourus dans la matière. Cette dernière, engendre un déphasage :

$$\Delta\varphi = \frac{2\pi}{\lambda} \left(\int_0^d n(\theta) dy - n_o d \right) \quad (1.43)$$

où d est l'épaisseur de CL traversé et λ la longueur d'onde du faisceau. C'est la modulation de ce déphasage ou variation de chemin optique qui est le plus souvent utilisé dans les dispositifs à cristaux liquides. Ainsi, dans un milieu biréfringent uniaxial, une polarisation se comportera comme si elle se déplaçait dans un matériau isotrope ordinaire, avec un indice de réfraction, tandis que pour les autres polarisations, l'indice de réfraction varie avec l'angle de la lumière incidente.

Connaissant ces propriétés polaire et birefringente, le principe des lentilles à cristaux liquides est de créer une interaction entre le champ électrique de commande et l'orientation moléculaire.

1.4 Lentilles de Cristaux Liquides : Design et Modélisation

Le développement des lentilles à cristaux liquides repose sur leur capacité à moduler un champ électrique pour orienter les molécules anisotropes selon des angles précis. Cette orientation génère un profil sphérique d'indice de réfraction, qui produit le profil de phase nécessaire à l'effet de lentille. Cependant, la conception d'un système permettant de créer un champ électrique sphérique tout en minimisant la consommation d'énergie et les perturbations électromagnétiques reste un défi majeur.

1.4.1 Lentilles dites "modales" vs Lentilles "quadripolaire"

Le design conventionnel, illustré à la figure 1.16, repose sur l'insertion de cristaux liquides entre des couches conductrices minces [7]. Une fine couche semi-conductrice, souvent en oxyde de titane, est déposée sur une plaque de verre. La conductivité de cette couche dépend de sa concentration en oxygène : le titane pur est conducteur, mais l'ajout progressif d'oxygène réduit sa conductivité jusqu'à un seuil critique où il devient isolant [54]. Cette propriété rend le contrôle précis de la concentration d'oxygène essentiel. Cependant, ce processus est délicat en raison de l'oxydation naturelle du titane en présence d'air. Pour stabiliser cette concentration, la couche est enfermée entre deux couches protectrices.

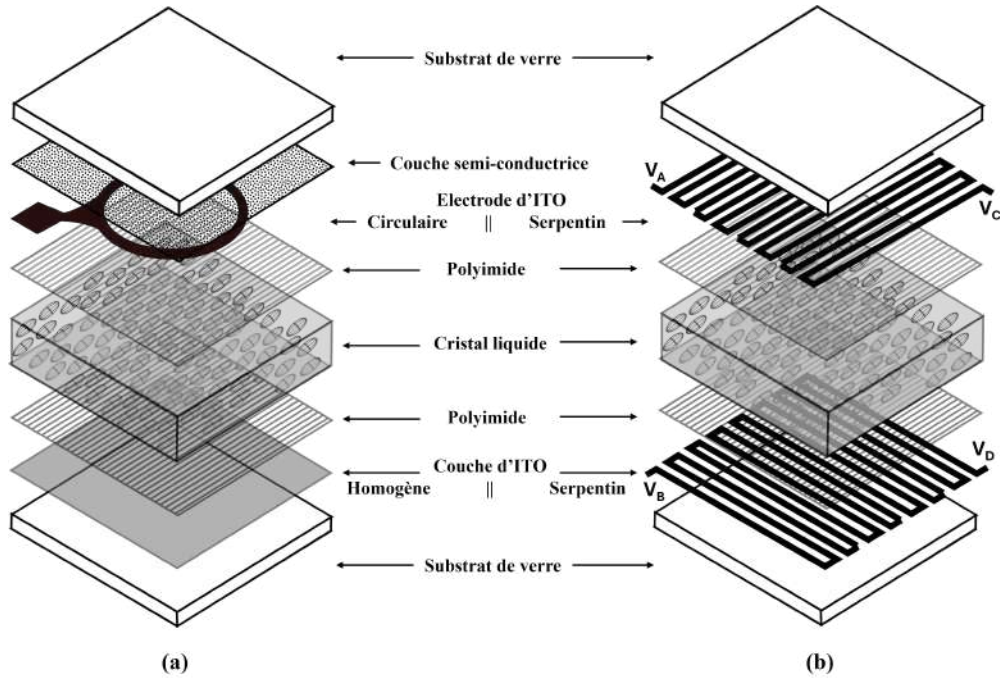


FIGURE 1.16 – Illustration présentant la différence entre une lentille à cristaux liquides dite "modale" et une lentille dite "quadripolaire"

Une couche supplémentaire d'oxyde d'indium-étain (ITO) est ensuite déposée. Un trou circulaire y est réalisé, délimitant la zone active de la lentille. Le diamètre de ce trou fixe celui de la lentille. Lorsque les cristaux liquides sont déposés et qu'un potentiel est appliqué à l'ITO, le champ électrique résultant est donné par $E = \Delta V/d$, où ΔV est la différence de potentiel et d l'épaisseur des cristaux liquides. L'application d'un signal alternatif permet de moduler la profondeur du champ électrique en ajustant la fréquence d'oscillation.

Cependant, ce design présente des limitations majeures. La fabrication homogène et reproductible de la couche semi-conductrice est techniquement complexe et coûteuse. De plus, la résistance obtenue pour un diamètre de lentille précis, ne permet pas de flexibilité dans le choix du diamètre de la lentille. Cela motive le développement de design ne nécessitant pas cette couche, tout en maintenant des performances optiques similaires [55, 56]. Notre équipe a récemment développé une configuration qui repose sur des couches conductrices en ITO gravées en forme de serpent [8], elles permettent de moduler efficacement le champ électrique avec une consommation énergétique réduite. Ces électrodes serpents, orientées orthogonalement autour des cristaux liquides, augmentent la résistance électrique, limitant ainsi la consommation d'énergie. La figure 1.16(b) illustre la configuration des électrodes de ce design où les cristaux liquides sont placés entre deux couches d'ITO gravées en serpent. Ces électrodes sont alimentées par quatre signaux sinusoïdaux déphasés de 90° : le signal A (0°), le signal B (90°), le signal C (180°) et le signal D (270°). Cette configuration génère un champ électrique tridimensionnel contrôlé dans les cristaux liquides.

Pour modéliser le comportement des électrodes serpentins et des cristaux liquides, un circuit électronique équivalent est défini, comme le montre la figure 1.17. Dans ce modèle, R_s représente la résistivité des électrodes ITO, c la capacitance des cristaux liquides, et g leur conductivité.

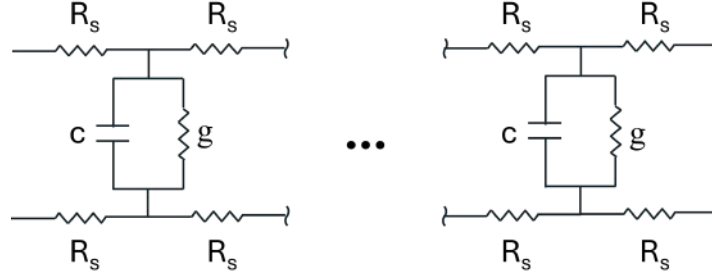


FIGURE 1.17 – Circuit équivalent du système de lentille à cristaux liquides

La différence de potentiel entre les électrodes supérieure (U_t) et inférieure (U_b) est donnée par $U = U_t - U_b$, et le champ électrique est défini par $E = U/d$, où d est l'épaisseur des cristaux liquides. L'équation différentielle associée à la répartition du potentiel au travers de la lentille est donnée dans [57, 58, 59] et sera décrit plus en détail dans le chapitre 2, avec l'équation 2.1. Dans un domaine fréquentiel, les signaux appliqués sur U_t sont en opposition de phase, de même pour U_b , c'est cette différence de potentiel qui définit la grandeur du champ électrique E dans la lentille. La différence de ces signaux engendre en toute circonstance une chute du potentiel à 0 au centre de la lentille, indépendamment de la résistivité de l'électrode en serpent.

Dans un domaine temporel, le déphasage des signaux engendre une rotation rapide du potentiel électrique qui induit un profil de phase conique à l'échelle de la vitesse de réorientation des CL, comme le montre la figure 1.18 et 1.19.

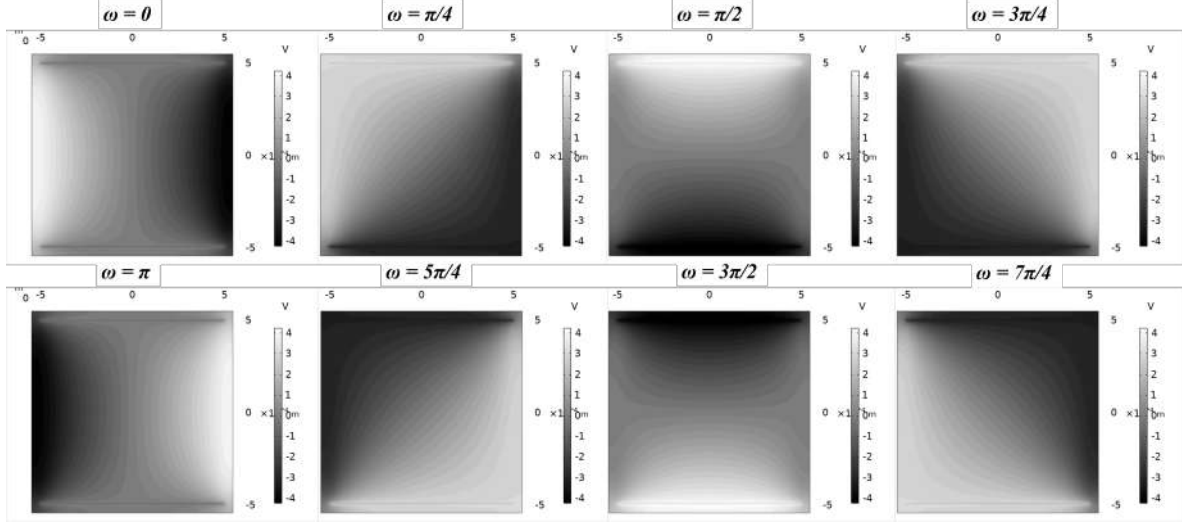


FIGURE 1.18 – Evolution temporelle du potentiel électrique sur une période au travers d'une lentille simple à électrodes résistives

Néanmoins, dans cette configuration une limitation est présente. En s'approchant du centre de la lentille, une portion non négligeable au centre de la lentille est soumise à une valeur de potentiel inférieur au seuil d'orientation de Freedericksz (E_c), un plateau dans le profil de phase est générée, ce qui entraîne l'apparition d'aberration sphérique et réduit les performances de la TLCL.

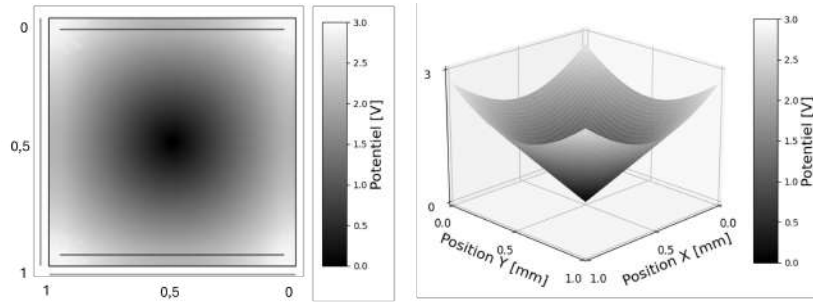


FIGURE 1.19 – Profil du potentiel électrique moyenné sur une période

Pour surmonter cet inconvénient et atténuer le pic central (fig.1.19), un signal à basse fréquence (f) avec une amplitude de V_{offset} est superposé (fig.2.2) au signal haute fréquence (F) [60, 61]. Pour minimiser l'amplitude de V_{offset} , le signal est appliqué à U_t et U_b en opposition de phase. Cette approche de l'offset vise à faire tourner, autour de la région centrale, la position où le potentiel atteint 0V au cours de sa période ($1/f$). Par conséquent, en moyennant sur cette période le potentiel n'est plus à 0 au centre de la lentille 1.20.

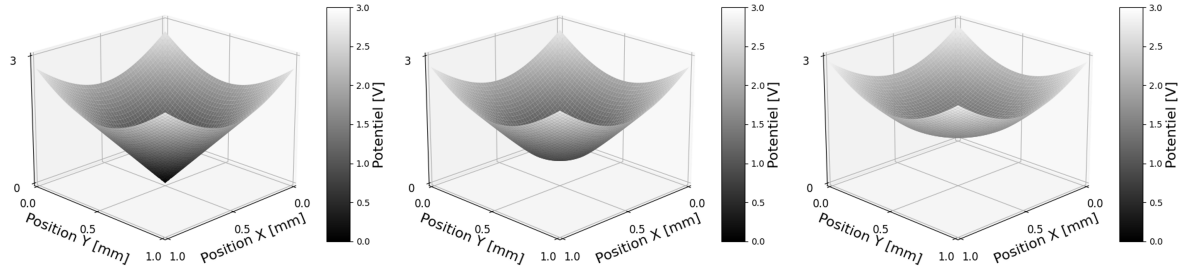


FIGURE 1.20 – Profils moyens de $U+V_{offset}$ à 20Hz pour différentes amplitudes du signal offset : de $0 V_{RMS}$, $1.2 V_{RMS}$ et $2 V_{RMS}$ de gauche à droite.

Ce design élimine la nécessité de couches semi-conductrices complexes. Les indices de réfraction des matériaux restent proches dans le spectre visible, minimisant les réflexions et préservant la qualité optique. Cette approche permet une meilleure reproductibilité, tout en répondant aux contraintes d'applications où les ressources énergétiques sont limitées. Dans un circuit RC, plus la fréquence est basse, plus l'impédance augmente, ce qui entraîne une diminution de la puissance dissipée.

Connaissant cette approche, nous avons développé

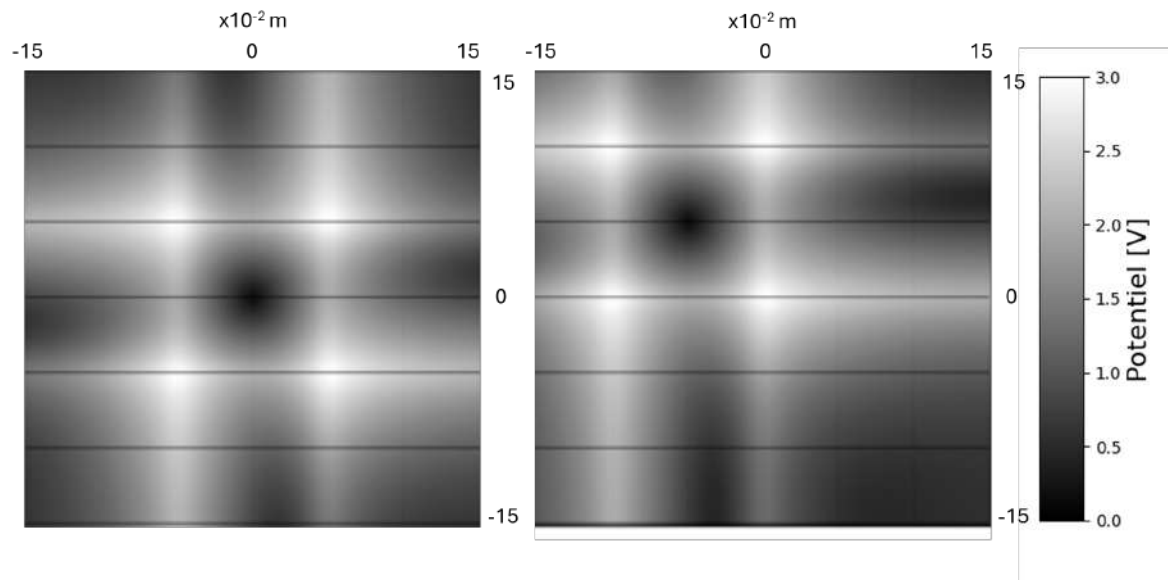


FIGURE 1.21 – Caption

C'est avec ce Enfin, en optique physiologique, la puissance optique d'une lentille ou d'un système optique s'exprime en dioptries (D). La valeur en dioptries correspond à l'inverse de la longueur focale effective de la lentille, exprimée en mètres. Par exemple, une lentille ayant une longueur focale de 1 mètre a une puissance de 1 dioptrie.

ADAPTIVE LENS FOR FOVEAL VISION, IMAGING AND PROJECTION OVER LARGE CLEAR APERTURES

Bégel Louis¹, Khodadad Behzad², and Galstian Tigran^{1,2}

¹ Center for Optics, Photonics and Laser, Department of Physics, Engineering Physics and Optics, Université Laval, 2375 Rue de la Terrasse, Quebec, G1V 0A6, Canada

² LensVector Canada, 2375 Rue de la Terrasse, Quebec, G1V 0A6, Canada

We report an electrically tunable liquid crystal device that enables the generation of lenses the diameters of which may be dynamically changed from sub-millimeter to multiple millimeter sizes. These lenses can be created in different regions of interest over very large (above 50 mm) optical clear apertures. The approach is based on the activation of periodically spaced contacts on a single serpentine-shaped electrode with phase-shifted electrical signals. It enables a highly reconfigurable operation of locally created lenses with variable position, diameter, optical power (OP) and aberrations.

The preliminary demonstration of the capabilities of the proposed device is presented here by creating a local lens, moving its center over an area of 25 mm x 25 mm, gradually changing its diameter from 1.3 mm to 4.55 mm as well as by tuning its OP value from zero up to, respectively, ≈ 40 and ≈ 3.5 diopters. Typical driving signals are at the order of 3.5 V. We think that such lenses can be used for ophthalmic or augmented reality applications as well as in microscopy, adaptive panoramic cameras with large distorted field of view, dynamic projection, etc.

2.1 Introduction

During the last few decades, the tendency of optical systems for miniaturization [62] has encouraged the development of electrically variable adaptive components (for example, lenses, [63]) to enhance the performance of these systems. In the large majority of cases, it is highly desirable to achieve such adaptive capabilities without mechanical movements. Among others, mobile applications are growing significantly, and they are extremely sensitive to vibrations, shock and drop. For example, it is not convenient to use mechanical solutions for adaptive vision or even for Augmented/Virtual reality (while some of these systems still are using it because they do not have alternative solutions). In addition, size, weight, and energy consumption must be limited in such applications. Here is where the liquid crystal (LC) based solutions are very promising since rather important refractive index modulations can be achieved by locally reorienting the optical axis of the LC (the average orientation of molecular axes, called *director*, [44, 64]) thanks to the dielectric torque. In addition, these components are operating with very low power consumption that is important for mobile applications. Not surprisingly, electrically tunable LC lenses (TLCLs) were intensively explored (see, for example, [65]) in various areas such as autofocus [66], wavefront modulation [67, 37, 38], depth measurement from focus/defocus [68, 69], depth of field extension [70, 71], etc.

Currently, there is an increased interest for devices with large clear apertures (CAs), ranging from 20 mm to 50 mm, which is first of all related to augmented reality and ophthalmic applications (for dynamic distance accommodation). Unfortunately, TLCLs with large diameters are difficult to make, particularly if we prefer refractive type lenses (see hereafter). The reason is the relatively small optical path difference $OPD = \Delta n \times L$ that can be achieved in LCs, where $\Delta n = n_{\parallel} - n_{\perp}$ is the optical birefringence (n_{\parallel} and n_{\perp} are the extraordinary and ordinary refractive indices, respectively) and L is the thickness of the LC layer. For example, if we consider a single aperture TLCL, based on the gradient index (GRIN) principle, then the achievable optical power (OP) may be estimated as $OP = 8 \times OPD/CA^2$ [66]. Obviously, increasing the CA, for example, from 2 mm to 50 mm, decreases the achievable OP values by a factor of 625. The possibility of building such lenses by using the refractive Fresnel approach (to increase the achievable OP range) is presently being actively investigated by several groups (see, e.g., [72, 73, 74, 75]).

However, it is important to mention that in most above-mentioned (e.g., vision/ophthalmic) applications the "detection" is performed by the human eye. It is well known that human vision can be split into foveal and peripheral vision. The foveal one, in turn, can be split between central ($\pm 2.5^\circ$), paracentral ($\pm 4^\circ$) and macular ($\pm 9^\circ$) [2]. In the case of wearing glasses, the typical distance of glass from the eye is between 12 mm and 17 mm. Thus, a tunable lens, positioned on the eye glass for foveal vision, should require a maximum diameter of 5.5 mm to be activated at each time. When the eye ball is reoriented to put another object into its foveal vision zone, then the 5.5 mm diameter zone must be activated elsewhere, on the

surface of typically 50 mm total CA (largest size of eye glasses). Some change of the diameter and the profile of that lens may also be necessary.

Thus, we could work with very large optical surfaces if we could generate "local" lenses (of diameter 5.5 mm, or so) at various areas of that surface and tune their local diameters and OP values. Such an operation might be imagined by using standard LC displays (LCDs) or spatial light modulators (SLMs). However the OPD, achievable with these devices, is usually very small, e.g., $OPD = 0.5 \mu m$. Thus, only the diffractive Fresnel type solutions may be considered here with well-known difficulties related to their dichroic aberrations, focus discretization and manufacturing complexity [76]. In addition, to cover 50 mm diameters, it would require a huge number of electrodes to be controlled dynamically.

We have recently suggested (in a patent application without detailed analyzes, [75], and then with a basic study in an article [8]) a possible method of generation of relatively smooth transversal distributions of electrical potential (needed for the creation of above-mentioned refractive lenses), while using very limited number of control electrodes. It is based on a micro structured electrode layer providing very specific effective sheet resistance values, similar to those used in so-called modal control lenses. The modal control concept was pioneered by Kahn for tunable apertures [77]. Naumov's group has developed the first LC lens with the modal control approach[6]. Such a lens can be modeled as spatially distributed RC circuit and its structure is a set of layers in the following order : a low resistivity layer as a ground contact (such as indium tin oxide or ITO), an LC layer (dielectric), a high resistivity or weakly conductive layer (WCL) that improves the voltage and refractive index distribution, and a hole patterned electrode. The value of the optimal sheet resistance of the WCL is mostly defined by the lens radius and the LC thickness (Mega Ohms for mm sized diameters). On the basis of modal control LC lens, Kirby et al. have proposed a "Quad-pol" LC lens [60] that is driven by phase-shifted signals producing symmetrical electric field distribution. Kotova et al. have done research on the Quad-pol LC focusing device that implements phase delay profile in the form of a circular and elliptical cone and controls the position of the centre [58, 61]. With this approach, Algorri et al. have generated microaxicon arrays [59, 78, 79, 80]. The mentioned-above Quad-pol devices have a similar structure, and, while their electric field distributions are less affected by the change of the resistance of the WCL in the approximation of a small modal parameter, [57], the reproducible fabrication of environmentally reliable WCL remains a challenge. In addition, the radius of the lens is still limited (<10 mm) due to the use of GRIN approach. Thus, its use in relatively large aperture optical systems (ophthalmology, panoramic camera, etc.) is very limited. To avoid this limitation, refractive LC Fresnel lenses have been developed (see, e.g., [81, 73]). One of these approaches ([73]) does not use WCL which is very interesting. Unfortunately, its manufacturing seems to be complicated.

In the present study, we describe an interesting development of our new WCL-free approach ([75, 8]) based on the Quad-pol principle. We show that by the appropriate choice of electrode

geometry and driving method, we can create a cost effective, local, scalable, movable and tunable lens. To the best of our knowledge, such a device was not reported yet in the scientific literature. The proposed TLCL is using a matrix of control electrodes (further called, MTLCL) allowing its activation in the zone of interest at various (almost arbitrary) positions over a large optical surface. This is achieved thanks to the specific micro structured ITO pattern that is used to control the voltage distribution across the surface of the lens with a minimum number of control electrodes and without the use of WCLs, see, e.g., in [8, 82, 74] (see other approaches to replace the WCL in [83, 84]).

2.2 Structure of the lens and its operation principle

The proposed device is a sandwich-like structure composed of two ITO coated glass substrates that are separated by a gap thanks to spacers of $40\ \mu\text{m}$ diameter ($L=40\ \mu\text{m}$). It can be considered as a juxtaposition of multiple smallest controllable "unit cells", reported in [8]. Figure 3.1a) schematically shows the 3D view of the structure. The ITO layers are cast at inner surfaces of these substrates and are lithographically patterned into serpentine shaped continuous electrodes (one at each substrate). Two substrates are arranged so that their serpentine electrodes have orthogonal orientations. A top view of two serpentine electrodes is shown in Fig.3.1b). There are multiple spatially periodic electrical contacts (see, e.g., E1, E2 etc., on the top substrate and E5, E6, etc., on the bottom substrate, Fig.3.1a), that are connected to different segments of the same serpentine electrode. This allows actively changing the electrical potential distribution in these areas. The electrical potential between these contact areas is shaped thanks to the spatial attenuation as well as the specific driving method (see hereafter). In this specific implementation, the ITO serpentine was patterned with a width w and gap g of $w=35\ \mu\text{m}$ and $g=5\ \mu\text{m}$, respectively. Commercial polyimide (PI-150) layer was cast by spin coating over the ITO pattern of each substrate, baked and rubbed in "anti parallel" directions in order to obtain a homogeneous molecular alignment. The unit cell of the device here is a square area ($0.65\ \text{mm} \times 0.65\ \text{mm}$), the top view of which is shown in Fig.3.1b). While in principle, the number of control electrodes is not limited, in the current implementation, each substrate has 40 control contacts, resulting in a total controllable (active) area of $25\ \text{mm} \times 25\ \text{mm}$.

The cavity (formed by two substrates) is filled with a home-made nematic LC (NLC) mixture selected because of the relatively high birefringence of $\Delta n = 0.217$.

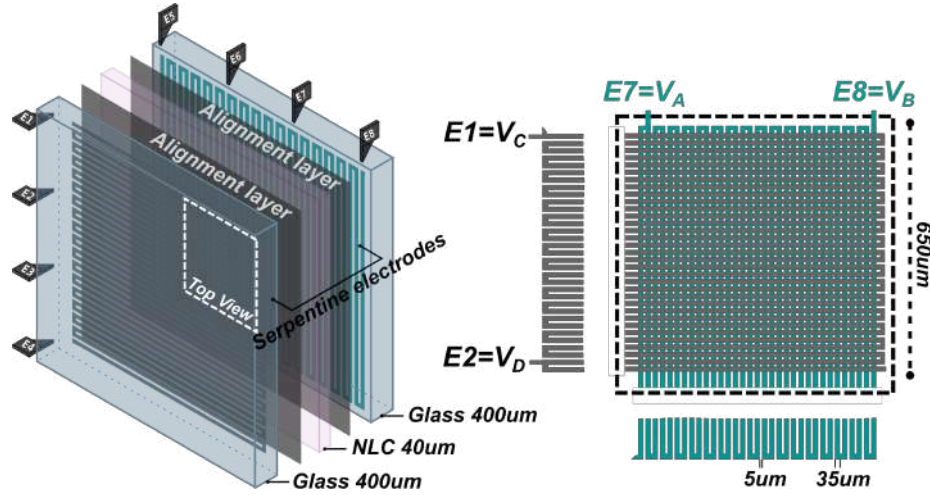


FIGURE 2.1 – Schematic demonstration of the device, a) 3D representation showing the electrode configuration and key layers, b) Top view of two cross-oriented serpentine patterns of ITO in the unit area of $0.65 \text{ mm} \times 0.65 \text{ mm}$.

We can start the analyzes of the operation principle of our device on the example of its unit cell [8], while the operation with larger diameters (including multiple unit cells) will be very similar, but will require the activation of control electrodes that are further from each other, like "peripheral" electrodes (V_A , V_B , V_C , and V_D , see Fig.3.1b)). In this case, intermediate control electrodes (between peripheral ones) must be managed in a well defined manner (e.g., left floating, see hereafter).

The main operation mechanism of the proposed device is based on the specific electrical resistance between control electrodes (low in comparison with the NLC's impedance) and on the combination of different phase shifts of electrical potentials applied to different control electrodes of the cell. For material and geometrical conditions that we are going to use here, this resistance generates an almost linear voltage distribution from one control electrode to another (on the same substrate) [58]. When the potentials, applied to control electrodes V_A and V_B , have a mutual phase shift of 180° (e.g., $\phi_A : 0^\circ$ and $\phi_B : 180^\circ$), then the potential at the center of this area is zero. The resulting voltage distribution on the substrate has the shape of a ramp, from $+V_A$ to $-V_B$. The same driving principle is used for electrode fingers V_C and V_D on the opposite substrate. However, in addition, these two driving signals have a common phase shift of 90° with respect to signals applied to two other electrodes (that is, $\phi_C : 90^\circ$ and $\phi_D : 270^\circ$).

The space-time distribution of the voltage U on each substrate can be described by a second-order partial differential equation taking into account the distributed RC circuit composed of the resistive serpentine ITO electrode lines (between peripheral electrodes) combined with the

capacitive dielectric NLC layer between two substrates, [58, 59].

$$\vec{\nabla}_s^2 U = R_s \cdot c \frac{\partial U}{\partial t} + R_s \cdot g \cdot U \quad (2.1)$$

Where, $c = \epsilon/L$ and $g = \sigma/L$, with ϵ being the dielectric permittivity and σ the conductivity of the NLC layer. If we consider *sin* driving functions (e.g., $\sin(\omega t + \phi)$) with $\omega = 2\pi f$, then the fourier transform of the eq.2.1 allows determining the complex amplitude of the voltage U .

$$\begin{cases} \vec{\nabla}_s^2 U = \chi^2 U \\ \chi^2 = R_s(g - i\omega c) \end{cases} \quad (2.2)$$

We can see, from eq.2.2, that the voltage distribution is governed by the parameter χ measured in reciprocal centimetres. We can therefore expect that the distributions $U(x, y)$ will differ considerably for large and small values of χl (where l is the characteristic size of the aperture). We shall define the impedance of the structure as $Z = (g - i\omega c)^{-1}$ and the ratio between the effective sheet resistance of the serpentine electrode R_s and the impedance, as $(\chi l)^2 = R_s l^2 / Z$. To be able to control the propagation of the electrical potential in the transverse plane (for different local diameters, see hereafter), the value of the resistance R_s must satisfy the condition $|\chi l| \ll 1$. In this case, the influence of the frequency on the voltage distribution becomes negligible, and the voltage distribution is controlled by the amplitude and the phase of the potential applied on control electrodes (E1, E2, etc.). The RC circuit has enough time to recharge and the potential at the centre follows the potentials' changes occurring at the peripheries, inducing a linear voltage distribution. However, we must keep R_s sufficiently high to limit the power dissipation.

This Quad-Pol lens is based on two resistive surfaces and potentials on top (U_t) and bottom (U_b) substrates. By considering $\chi_t = \chi_b = \chi$, we obtain the following voltage distributions :

$$\begin{cases} \vec{\nabla}_s^2 U_t = \chi_t^2 U_t - \chi_t^2 U_b = \chi^2 (U_t - U_b) \\ \vec{\nabla}_s^2 U_b = \chi_b^2 U_b - \chi_b^2 U_t = \chi^2 (U_b - U_t) \end{cases} \quad (2.3)$$

These equations may be solved, e.g., by using the finite element method on *Comsol* (in our case). For simplicity, we have considered our serpentine patterns as uniform resistive layers (identical on both substrates) with the sheet resistance of $5 \times 10^6 \Omega/\square$, while the conductivity of the NLC was set at $\sigma \approx 10^{-9} S.m^{-1}$.

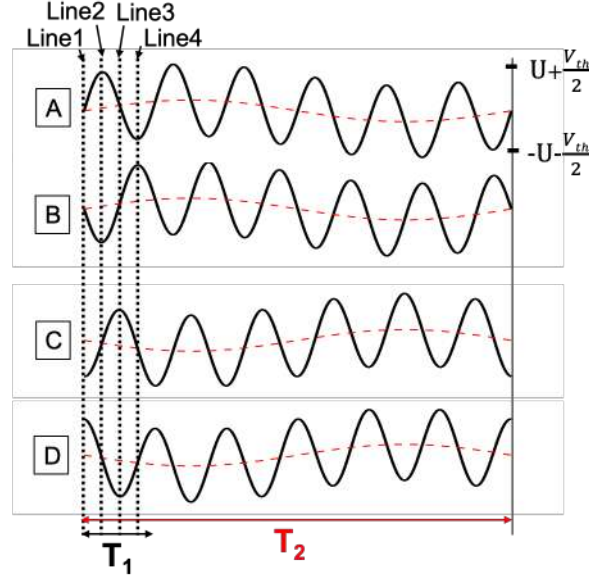


FIGURE 2.2 – Schematic demonstration of 4 phase-shifted electrical control signals (applied to contacts A, B, C and D) with an additional low frequency offset voltage shown by 4 horizontal curved dashed lines, with periods $T_1 = 1/F$ and $T_2 = 1/f$, respectively. Vertical dashed lines 1-4 show the phase shift between signals : Line 1 correspond to phase 0, Line 2 : $\pi/4$, Line 3 : $\pi/2$ and Line 4 : $3\pi/2$ of the period T_1 .

Molecules of an NLC with positive dielectric anisotropy ($\Delta\epsilon \geq 0$, at driving frequencies) tend to align parallel to the electrical field, and this interaction is governed by the root mean square (RMS) value of the applied voltage, $U_t - U_b$. To further simplify the analyses, we can consider the case when we use similar voltages $V_A/V_B/V_C/V_D = V$ with the same, relatively high (120 Hz), frequency F_1 . As it can be imagined from Fig.2.2 (thanks to Lines 1-4), the result of the imposed relative phase shift is a continuous change (with rotation) of the electric field and the creation of an RMS voltage distribution of conical shape (see its cross section in Fig.2.3a)). In the described geometry, NLC molecules can be reoriented only if the applied voltage exceeds a certain threshold value V_{th} [64, 44]. Thus, due to the above-described electric potential distribution profile and the existence of that threshold, there will be an area in the center of the cell where molecules will not be reoriented and the phase delay (of light traversing this area) will remain constant. This plateau can be eliminated in several ways, e.g., by adjusting the phase between two parallel electrodes on the same substrate (e.g., 160° instead of 180°) or by adding a low frequency offset V_{off} (see curved dashed lines in Fig.2.2) to two electrodes of the same substrate or by adding specific phase-shifted offset signals to all electrodes [85, 60, 79], (see Fig.2.3b)). The alternative offset component of the driving signal is shifting the instantaneous position of the zero volts in the transverse plane (between positions $-z_0$ and $+z_0$, see Fig.2.3b). It helps to shift-up the RMS voltage profile such that there is no region under the threshold voltage ($V_{off} \geq V_{th}$) of LC (see Fig.2.3 b)) as well as to increase the curvature of the potential in the center of the lens.

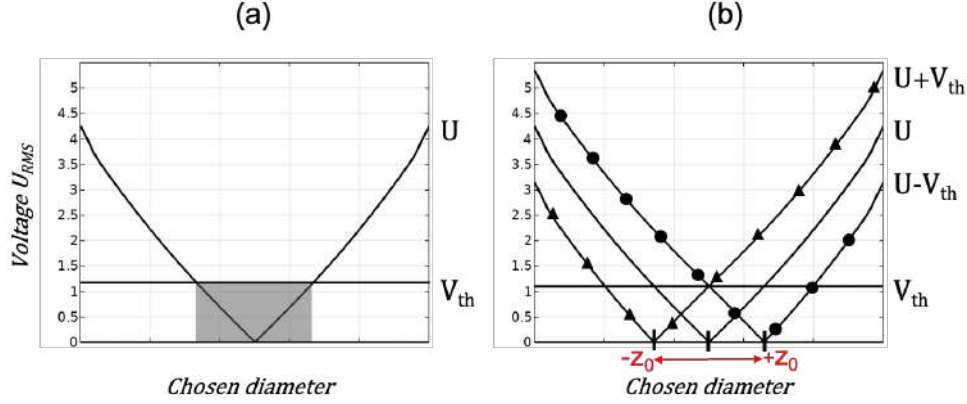


FIGURE 2.3 – Cross sectional view of V_{RMS} voltage distribution along X and Y axis, over the oscillation cycle; a) No offset voltage is applied; the dark rectangle corresponds to the area of the lens below threshold voltage, b) Adding alternative offset equal to V_{th} : during the first half period T_2 of the offset (filled triangles correspond to the top substrate voltage distribution profile and filled circles correspond to the bottom substrate), and vice versa for the second half period (see main text for details).

In order to generate the above-mentioned 4 electrical signals, a driving module has been designed and built. It consists of a custom electrical phase shift waveform generator. The micro controller (coupled with buffers/inverters) can generate two 90° phase-shifted electrical signals with high-frequencies F_1 and F_2 (in our implementation, $F_1 = F_2 = F$), as well as one signal with low-frequency f . These signals are combined as shown Fig. 2.2a) to produce 4 signals on contacts A, B, C and D. Finally, multiplexers are used to generate the drive outputs. These multiplexers can select open-circuit (floatting), one of the A/B/C/D signals, or ground to be applied to electrodes.

2.3 Experimental results

We have started the experimental characterization of our device by observing traditional interference fringes captured by placing the lens between two crossed polarizers with the rubbing direction of the NLC oriented at 45° from the linear polarization at the input as shown Fig. 2.4 a)[39].

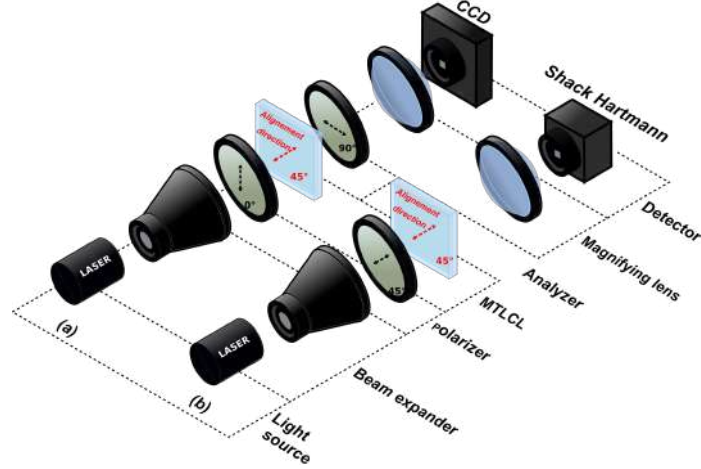


FIGURE 2.4 – Schematic presentations of experimental setups used for lens characterization. (a) polarimetric measurements, (b) Shack-Hartmann wavefront sensing.

In this case, both extraordinary and ordinary polarized propagation modes will be generated inside the NLC layer. They will exit from the cell with different phase delays at different transversal positions (when the lens is activated), and will interfere thanks to the second polarizer (analyzer) oriented at 45° with respect to the ground state molecular orientation of the NLC. Thus, two neighboring constructive (bright line) or destructive (dark line) interference fringes represent an optical phase difference of 2π . The obtained OPD can be easily converted into phase delay by multiplying it by $2\pi/\lambda$. One can see examples of such interference fringes in Fig. 2.5a) for three different values of the OP of the same lens (same diameter). This can give us a first visual information concerning the obtained wavefront profiles. We can use them also for a quantitative analyses. However, we can obtain more precise quantitative data by using a Shack-Hartmann wavefront sensor (described in Fig. 2.4 b)). For example, Fig. 2.5 b) and Fig. 2.5 c) demonstrate such wavefronts for excitation voltage values ranging from $1.5 V_{RMS}$ to $5.5 V_{RMS}$ (see the right vertical axis). The frequency of main excitation signals here was $F=120$ Hz during all this experiment and the frequency of the offset signal was $f=20$ Hz.

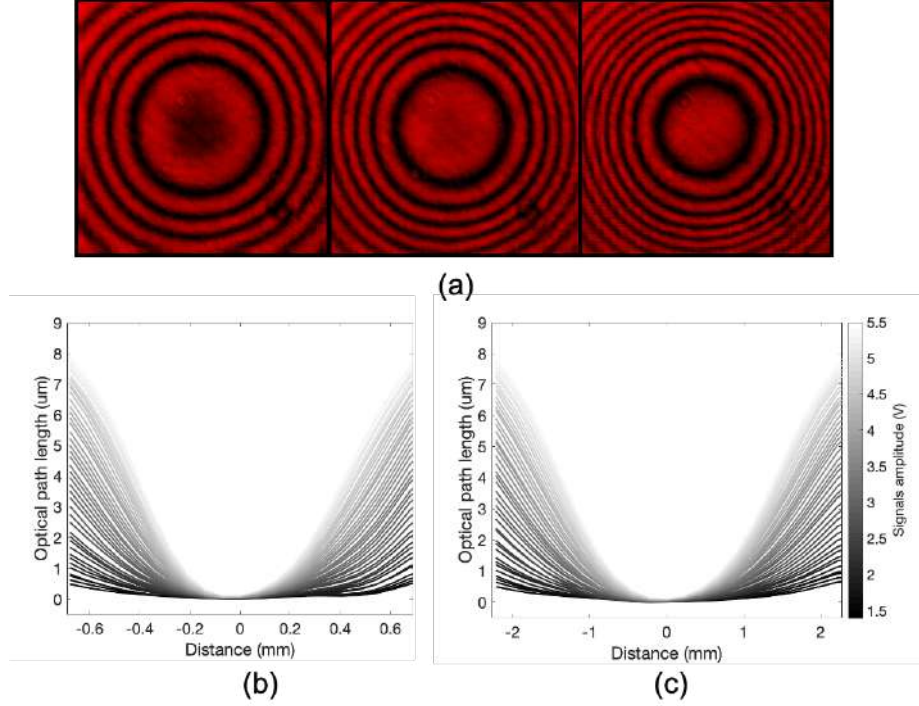


FIGURE 2.5 – a) Polarimetric interference patterns for $V = 2 V_{RMS}$, $2.5 V_{RMS}$ and $3.0 V_{RMS}$, from left to right, respectively, and $V_{off} = 1.2 V_{RMS}$, (b and c) Optical path length for two different lens diameters (1.3 mm and 4.55 mm), obtained from Shack Hartmann measurements, with increment of $0.1 V_{RMS}$.

Fig.2.5 shows the capability of this lens to progressively increase its OP by increasing the voltage value applied on control electrodes (see hereafter for quantitative measurements of corresponding aberrations). This demonstration was performed qualitatively for a given diameter (Fig.2.5 a)) and, in a more detailed way, for two specific diameters, 1.3 mm and 4.55 mm, Fig.2.5 b) and Fig.2.5 c), respectively. However, as we have already mentioned, the proposed design has the capability of gradually scaling the size of the lens diameter. If we wish to increase the CA, then we must keep in mind that our lens is a GRIN lens, and thus its OP decreases quadratically with the aperture size of the local lens. Also, to generate local lenses with larger CA, we must choose a different sheet resistance for the ITO to keep aberrations low.

To demonstrate this capability, the control contacts A, B, C and D were first selected as peripheral electrodes (defining the desired size of the lens), and excitation signals were applied to them. All inner electrodes (between the peripheral ones) were left in the floating (F) states. The low resistance serpentine electrode pattern, we have designed here for a specific application, allows to easily generate from simple ($\varnothing=0.65$ mm) up to septuple lens sizes ($\varnothing=4.55$ mm), see Fig.2.6, with the same character of voltage distribution. The top left picture in Fig.2.6 shows the interference pattern of the device in the ground state. The large curved

dark zone between two bright zones is witnessing the slightly non uniform gap (thickness) of the NLC due to the fabrication imperfections. The picture at the top right demonstrates the generation of a small diameter lens (CA=0.65 mm). The following pictures (below) show larger lenses, obtained by pushing peripheral electrodes farther from each other. The last picture (bottom right) shows the example of a lens with CA=4.55 mm.

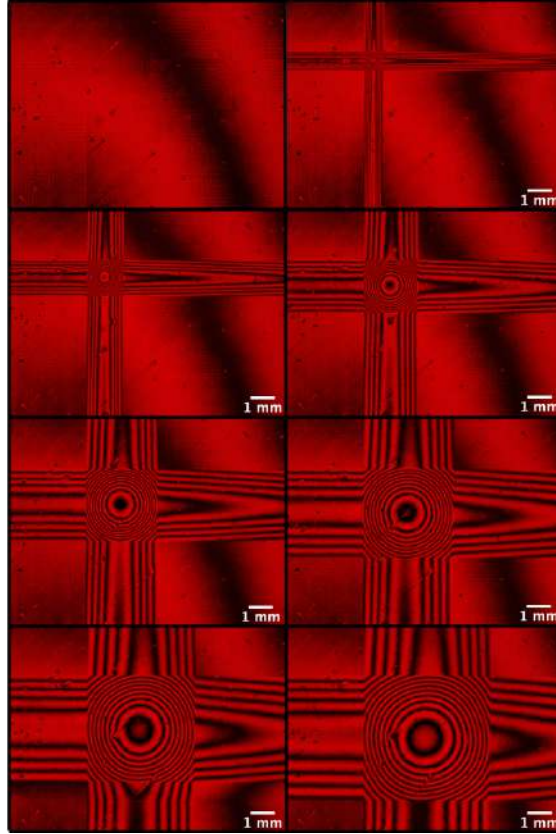


FIGURE 2.6 – Interference pattern for several lens sizes, ranging from CA = 0.65 mm to CA = 4.55 mm, $V = 3.2 V_{RMS}$ and $V_{off} = 1.2 V_{RMS}$.

Corresponding wavefronts were quantitatively characterized by using a probe beam of extraordinary polarization mode (the incident beam was linearly polarized along the rubbing direction of the polyimide). Our experimental procedure was as follows (see fig.2.4. b) [82]). The reference wavefront was recorded without the MTLCL by using a Shack-Hartmann wavefront sensor (Thorlabs). Then, we have introduced the MTLCL and aligned its position (x,y, and z) by using micrometric tables. A relay lens was used to image the output plane of the MTLCL on the sensor plane of the Shack-Hartmann sensor. For a given voltage and frequency of excitation signals, aberrations of the lens were measured and analyzed using Zernike coefficients. We have measured up to the 66th Zernike polynomials, but we shall discuss only aberrations between the orders 0 to 4; according to Zernike classification, these first-order aberrations are responsible for main deformations of the wavefront [2]. Zernike polynomials are orthogonal over

a unit circle and represent optical aberrations over a circular pupil. These characteristics are lost when non circular pupils are employed. Some schemes for square pupils have obtained square polynomials [86] from the orthogonalization of circle polynomials [87], using a circle inside the square. This procedure has the disadvantage of losing the part of the wavefront that falls outside the circle. Some other studies overcome this problem by defining a unit square inside the circle [88]. However, these orthogonalizations are theoretical interpretations of square wavefront shape from circular shape, so we shall not investigate this question here since our main goal is to show the main capabilities (here, the tunability) and size variations for circular apertures only.

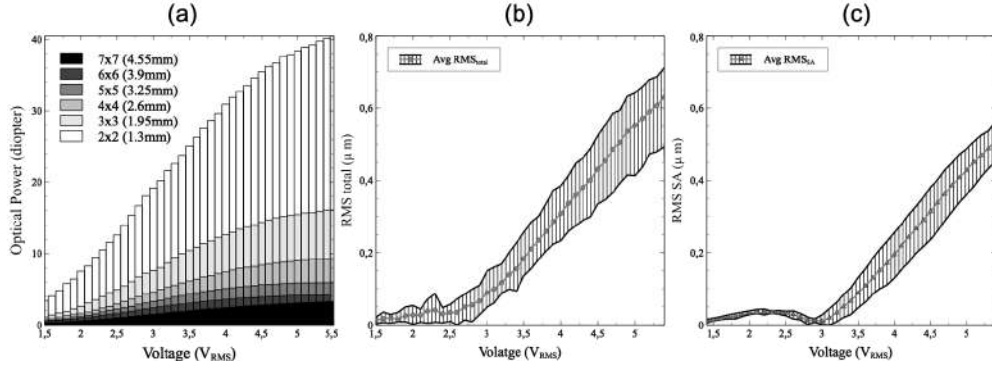


FIGURE 2.7 – Optical characterization of lenses of various sizes, ranging from 1.3 mm to 4.55 mm, a) OP vs voltage, b) Total RMS wavefront error vs voltage, c) RMS wavefront error for spherical aberrations vs voltage. Hatched zones correspond to max and min values measured for each lens size.

As it is shown in Fig. 2.7, the obtained OPs (in diopters) are indeed inversely proportional to the square of the lens size, as predicted. We experimentally reach 40 diopters of OP for the double lens ($\varnothing=1,3$ mm) in comparison with the septuple lens ($\varnothing=4.55$ mm) the maximum OP of which is reaching 3.5 diopters. For constant frequency and amplitude values, the wavefront is theoretically identical for each lens size due to linear voltage distribution. Indeed, the total RMS aberrations show the same tendency for all diameters. Up to $V = 3.6 V_{RMS}$, the total RMS error is below $0.2 \mu m$. Spherical RMS aberrations are representing the majority of the wavefront deformations in these lenses. Up to $3.5 V_{RMS}$, the generated lens maintains a good spherical profile, but for higher voltage values, spherical aberrations increase, and the lens' shape tends to a conical profile (generating an axicon).

In the next section, we demonstrate the capability of the proposed design to change the position of the local lens. Indeed, when the desired position (the center) of the lens and its diameter are decided, then we activate the peripheral control electrodes (A, B, C and D) that are centered around the desired position and spaced (separated) from each other to provide also the desired diameter. All the rest of the procedure is the same. To move the center of the lens, the same four signals are applied on different peripheral electrodes that are centered now

around the new position. Obviously, if we desire to keep the same diameter, then the distance between these peripheral electrodes must be kept constant, see the corresponding example in Fig.2.8. To facilitate the discussion of these localized lenses, vertical and horizontal references (by numbers and letters, respectively) were added to easily identify their positions. In this particular demonstration, the diameter was kept constant (1.3 mm).

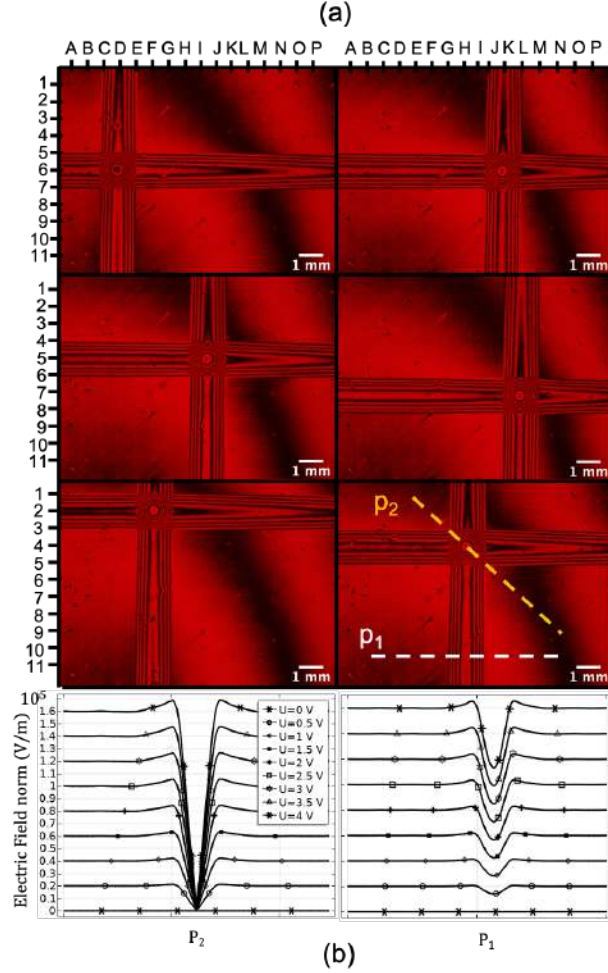


FIGURE 2.8 – a) Interference patterns for several positions of a lens (with the same $CA = 1.3$ mm) through the surface of the MTLCL. $V = 3.2 V_{RMS}$ and $V_{off} = 1.2 V_{RMS}$; b) Electric field's profile through the active lens (line P_2) and through the addressing electrodes (line P_1).

It is also interesting to analyze (see Fig.2.8) the wavefront scans across the lens (by diagonal, along the dashed line P_2) as well as across the "traces" generated by the activation of control electrodes (along the dashed line P_1). It is clear that, in this implementation, we have generated a good lens (see bottom left, Fig.2.8 b)) in the central zone of interest, while there is also a relatively weak cylindrical lens created between the peripheral electrodes (see bottom right, Fig.2.8 b)). Here also, we can use the spatial frequency of interferential fingers to evaluate the corresponding profile changes.

If desired, we can reduce the cylindrical lensing effect in regions outside the active lens. This may be done by avoiding (or reducing) the abrupt drop (or change) of the electric potential and corresponding molecular reorientations in these areas. For example, if the electric potential, applied on external (around the zone of interest) electrodes, are close to V_{sat} (with V_{sat} being the reorientation saturation voltage) then all the NLC, around the active lens, will be completely reoriented (tending to homeotropic alignment), and the active lens will then be better localised. In our case, due to the driver limitation, we were able to apply on external electrodes (out of the zone of interest) only a voltage V similar to those applied on electrodes A, B, C and D, see Fig.2.9 d). However, we are convinced that the application of higher voltages $V_{ext} > V$ can induce a fully localised lens. In the opposite case, our simulations and measurements confirm that, if the outer electrodes were left floating (Fig.2.9 b)) or grounded (Fig.2.9 c)), then the voltage drop increased. When the same signals were applied also to external electrodes, it induced a relatively uniform electrical potential in the outer area (Fig.2.9 d)).

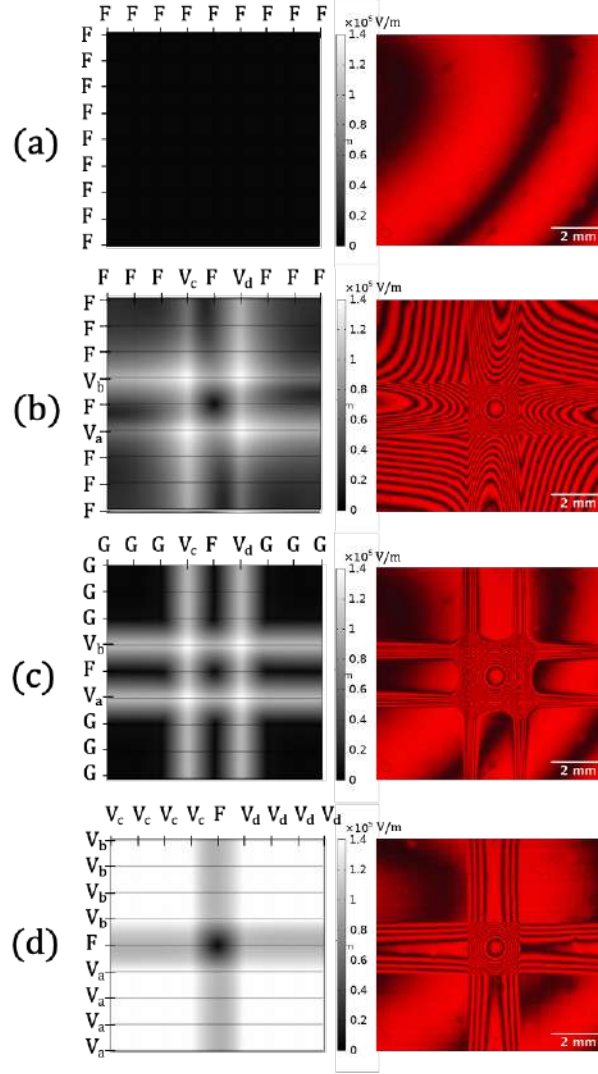


FIGURE 2.9 – Left column : theoretical simulations of the electric field distribution depending upon the external electrodes' states, floating : F ; ground : G ; V_a, V_b, V_c and V_d : A/B/C/D signals. Right column : experimental observations of the interference pattern. a) Reference image, all electrodes are in the floating (off) state. Lens generation : b) applied 4 phase shifted signals $V_a/V_b/V_c$ and V_d , while maintaining external electrodes in floating states. c) external electrodes are in Ground state. d) external electrodes are in the same state as the control signals applied to the peripheral control electrodes of the desired zone.

Furthermore, to evaluate the local improvement of image quality, the MTLCL was positioned in front of a standard commercial camera (Raspberry Pi Module v2 combined with 6 mm wide angle lens). The camera lens was adjusted to have target objects (books) out of focus. Then, a local lens of diameter 3.9 mm was activated and its OP was adjusted to bring one part of the scene (the note "Think Python" positioned at approximately 37 cm) in focus. The corresponding voltage was $3.6 V_{RMS}$ and the OP was 4D. Figure 2.10 shows the difference between the out of focus image (with the MTLCL disabled but still in front of the camera, Fig.

2.10 a)) compared to the case when the MTLCL was activated Fig. 2.10 b). The corresponding improvement of the modulation transfer function of the system is demonstrated in Fig. 2.10 c), there is no copy right issues ; we have recorded this image by using commercially available books.

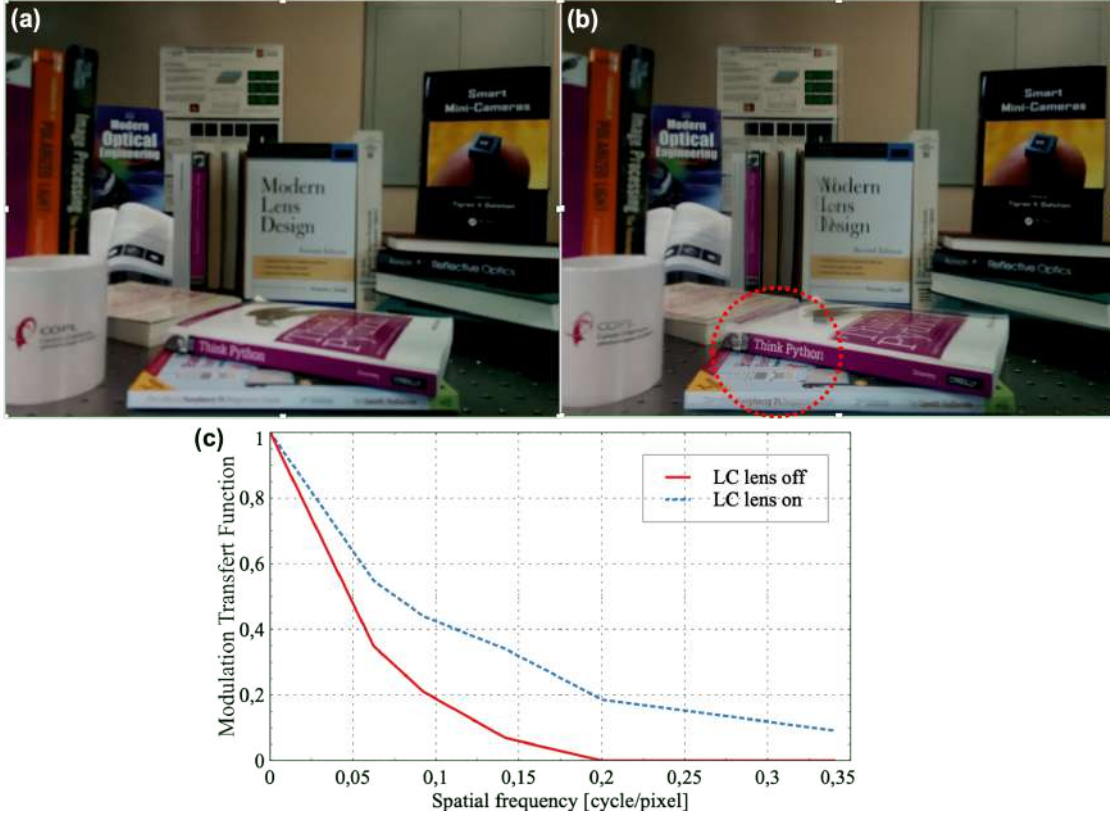


FIGURE 2.10 – Impact of the MTLCL on the local image quality recorded on a random scene by using a commercial Raspberry Pi camera combined with MTLCL, a) original photo, MTLCL is off. b) photo with a local lens (with 3.9 mm diameter) activated (at $3.6 V_{RMS}$), focused on the area "Think Python". c) the corresponding modulation transfer functions of the region of interest.

2.4 Discussions and Conclusions

The capability of creating tunable lenses in different positions and changing their diameters seems to be a very interesting feature when dealing with large optical surfaces where the standard GRIN approach is not efficient over the entire surface, but the zone of interest may be dynamically localized. The proposed design could be very promising first of all to enhance the vision (ophthalmic, augmented reality, etc.) and imaging (microscopy, endoscopy, panoramic cameras with distorted large distorted field of view, etc.). Its applications in various

display and projection systems also is quite possible. In many of above-mentioned applications there are indeed local zones of interest changing dynamically. Obviously, these applications have various requirements in terms of performances. The variability range of the OP and corresponding aberrations of obtained here lenses are similar to traditional modal lenses and should be acceptable for the majority of these applications.

In the presented here implementation, we observe wavefront perturbation outside the zone of interest, but in many above-mentioned applications that zone has less importance. Human tests we have started recently confirm this hypothesis (a corresponding manuscript is in preparation). However, as we have mentioned above, if desired, it will be possible also to create fully localised lenses, without noticeably disturbing the external area, by modifying the driver.

Concerning the zone of interest for foveal vision : we have already mentioned that 5.5 mm diameter lenses might be large enough to insure a clear foveal vision. Our current demonstration was made with lenses of CA=4.55 mm (designed for a different application), which were providing 3.5 diopters of OP. If we use the inverse square rule of tunable GRIN lenses, we should be able to generate 2.4 diopters of OP for 5.5 mm diameter lenses. According to our discussions with ophthalmology experts, this should cover the large majority of customers. In addition, thanks to the specific electrode structure of the local lens and its driving technique, we have much richer wavefront control capabilities. Namely, we can generate also cylindrical lenses, axicons, etc. (e.g., for compensating astigmatism, coma, etc.).

For the current implementation, we have used 0.65 mm as the minimum distance between control electrodes, which defines the minimum diameter (or the unit cell size) of the lens. Also, the external size of the optically active area was 25 mm x 25 mm. However, there is no fundamental reason why we could not change these values. From the point of view of the local lens ; the main limiting factors, to obtain smaller sizes, shall be related to the choice of the ITO's sheet resistance R_s and to the thickness of substrates used. Indeed, in some cases (not always) a polarization independent operation will be required. Thus, we would need to laminate two such devices together (cross oriented, see, e.g., [66]), with NLC layers as closes as possible to avoid the polarization related aberrations [89]. For larger sizes (still for the local lens), the main optimization should be related to the choice of the R_s . For such sizes, we can increase the thickness of the LC layer to partially compensate the loss of the OP, but this must be done considering also the speed and scattering requirements of target application.

In terms of the external size of the device (the active area over which we can move the local lens) - we do not see limitations, except the number of connections, which, by the way, is much smaller in our case compared to traditional LCDs and SLMs.

The fact that we create such lenses without using a WCL is another important advantage from the manufacturing (cost) point of view. Indeed, our patterned ITO is rather simple to manufacture in a single lithographic step, compared to the WCL. Finally, with very low voltages (below 5.5 V_{RMS}) and frequencies (20 - 120 Hz), required for the control, this device

will feature very low power consumption that is another important advantage for mobile (e.g., ophthalmic or augmented reality) applications.

There are still important characterizations to be done, such as the speed (currently, the Activation/Relaxation times are at the order of 0.2 sec and 0.8 sec, respectively) and haze measurements and their possible optimizations (if required by the specific application), but we can already state that the proposed device has very high potential for applications.

Acknowledgments

We would like to thank LensVector for the financial and material support. We would like to express a special thank to A. Bagramyan for his help in the process of lens prototyping.

Disclosures

Authors declare no conflict of interest.

Data availability

Detailed data underlying the results, presented in this paper, are not publicly available at this time, but may be obtained from authors upon request.

DYNAMIC CONTROL OF DEFOCUS, ASTIGMATISM AND TILT ABERRATIONS WITH A LARGE AREA FOVEAL LIQUID CRYSTAL LENS

Bégel Louis¹, and Galstian Tigran^{1,2}

¹ Center for Optics, Photonics and Laser, Department of Physics, Engineering Physics and Optics, Université Laval, 2375 Rue de la Terrasse, Quebec, G1V 0A6, Canada

² LensVector Canada, 2375 Rue de la Terrasse, Quebec, G1V 0A6, Canada

We have recently reported the dynamic adjustment of the focal length in an electrically tunable liquid crystal "foveal" lens the center of which can be shifted over a large working area. In the present work, we show that this design allows also independently generating astigmatism with arbitrary axis and tilt of light wavefront by simply changing the phase and the voltage differences between 4 control electrodes. Furthermore, we also demonstrate the capability of generating highly localised negative (defocusing) lenses with the same device by using a dual frequency liquid crystal.

3.1 Introduction

Liquid crystals (LCs) have been successfully used in pixelated optical devices, such as LC displays (LCDs) and Spatial Light Modulators (SLMs), see, e.g.[90, 91]. However, for many

mobile applications, these devices are cumbersome and costly. Adaptive gradient index (GRIN) optical devices (such as tunable lenses, see, e.g. [92, 6, 66, 65, 62]) represent an interesting alternative for using LC materials in optical imaging or vision systems since, compared to LCDs or SLMs, they can be made much smaller, requiring significantly less electrodes (at least by an order of magnitude) and may be fabricated at very low cost (at least by 2-3 orders of magnitude). Such devices have been successfully used for miniature cameras with 1.5 mm - 2 mm optical clear apertures (CA) [66, 62]. Despite the fact that the typical optical path differences $OPD = \Delta n L$ (where Δn is the optical birefringence and L is the thickness of the LC layer [38]) of such components are usually much larger compared to LCDs or SLMs, their use with devices having larger CAs still faces challenges. One possible approach here is the use of diffractive structures, but the chromatic aberrations, discrete focus and high cost (electrodes with very small features must be etched) are important issues to consider [76, 93, 94]. Another possible approach is the use of refractive Fresnel type phase resets, and several groups, including our group, are working in this direction [73, 81, 95].

In the meantime, we have recently introduced a new design of an electrically tunable LC lens (eTLCL) allowing the generation of local lenses, the center of which may be moved over a very large CA [96]. We call them "foveal" by referring on the fact that, at each moment, only a local area of the device is usually operated. By using this eTLCL, we have successfully generated spherical lenses with different diameters and positive (focusing) optical powers (OP). Currently we are working on several applications of this lens. One of them is in microscopy and endoscopy (to excite and to image only the zone of interest and scan that zone dynamically [97]), while other applications are in augmented reality glasses and virtual reality headsets.

In the present work, we continue its exploration and we show that the same design allows much richer functionalities, including the generation of an almost free-axis astigmatism, tip/tilt, etc. In addition, we demonstrate also the generation of highly localized lenses with negative (defocusing) OP with the help of so called "dual-frequency" LCs. The article is organized in the following way. We first briefly present the structure and the operation principle of the device. Then, we discuss the metrology tools used for its characterization. Obtained results on the generation and the control of the astigmatism, defocus, and tip/tilt are then presented and discussed. Finally, a preliminary experimental demonstration of a localized lens is presented for a negative OP, followed by discussions and conclusions.

3.2 Structure and operating principle

Lens design and operation principle.

The structure and the general operation principle of the proposed device were already reported in [8, 96]. As a short reminder, it consists of two glass substrates coated by indium tin oxide (ITO) transparent conductive layers, which are lithographically patterned into ser-

pentine forms (Fig.3.1). The width w of ITO lanes, the gap g between them as well as the sheet resistance R_o of the ITO must be optimized for specific applications, e.g., dynamic vision correction, panoramic or microscopic imaging, etc. There are two main criteria for this optimization : 1- to be able to generate the maximum possible modulation depth for the spatial distribution of electrical potential (from one control electrode to the other), and 2- to ensure that this spatial distribution is continuous (without discrete jumps) and not abrupt (to reduce undesired aberrations). For example, if R_o is too high, then, small values of w and g will generate abrupt decrease of the electrical potential and the resulting aberrations will be high. In contrast, if the values of w and g are too high, then there will be a discretization effect (in the distribution of the electric potential), which will generate undesired diffraction increasing the haze.

In the present implementation, we had $w = 35 \mu m$, $g = 5 \mu m$ and $R_o = 1 M\Omega/sq$. The total working area of the device was set to $25 mm \times 25 mm$. The serpentine ITO pattern was connected (through periodically spaced peripheral "contact electrodes") to an electrical driver at each $0.65 mm$ distance, resulting into a total of 40 electrodes on each substrate. Polyimide (PI150) alignment layer was spin-coated on each substrate, cured and uniformly rubbed (in "antiparallel directions", [98]). Finally, these substrates were used to form a sandwich (spaced with the help of $L = 40 \mu m$ micrometer diameter beads, see Fig.3.1a) and the space between them was filled by a commercial nematic LC (NLC) ML2608 (from Merck).

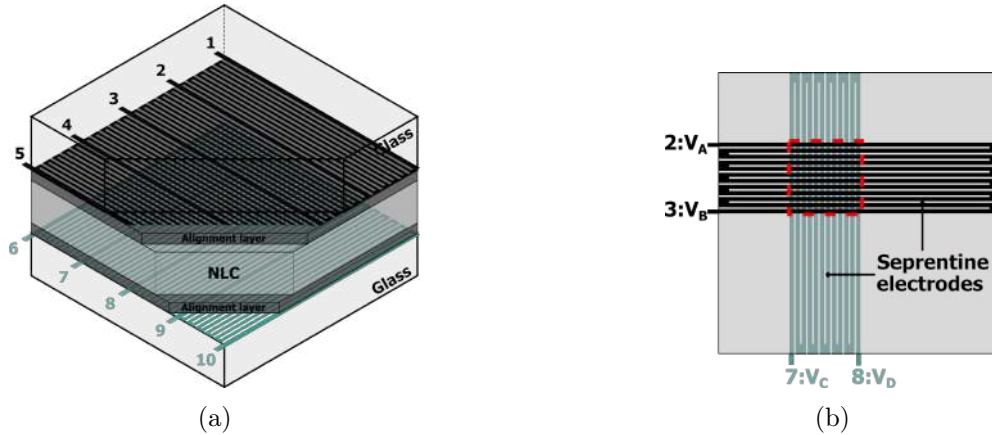


FIGURE 3.1 – (a) Schematic 3D representation of the device showing electrodes' structure, orientation, and contact electrodes' positions (e.g., 1-5 on top and 6-10 on bottom substrates), (b) Top schematic view, example of a "smallest lens unit" area (shown by the dashed red rectangle), where 2-3 & 7-8 represent activated contact electrodes (on top & bottom substrates) with corresponding signals V_a, V_b, V_c and V_d .

The wavefront modulation here is based on the control of the phase ϕ and the amplitude V of signals applied to control electrodes [58, 61, 99]. We can briefly present the operation principle of the device on the example of the smallest lens unit, controlled by 4 closest control electrodes V_a, V_b, V_c and V_d , shown in the Fig.3.1b. We have already demonstrated the possibility to

generate tunable (with only positive OP) and scalable (with variable local CA) spherical lenses by using this approach[8], when the same voltage V and an increment of 90° phase delay (ϕ) was applied to control electrodes, from V_a to V_d (that is, $\phi_a = 0^\circ$, $\phi_c = 90^\circ$, $\phi_b = 180^\circ$ and $\phi_d = 270^\circ$). Namely, when the phase delay is set to $\Delta\phi_t = \phi_a - \phi_b = 180^\circ$ on two electrodes on the same (say, top) substrate, then the root mean square (RMS) voltage profile may adopt a cylindrical shape with linear gradient (perpendicular to electrode lines) and zero value in the center of the electrode structure. However, applying simultaneously the same phase shift of $\Delta\phi_b = \phi_c - \phi_d = 180^\circ$ on the control electrodes of the bottom substrate and maintaining a common phase shift between the top and bottom electrodes $\Delta\phi_t - \Delta\phi_b = 90^\circ$, will generate two phase shifted and spatially overlapped identical and orthogonal cylindrical shapes. The resulting rapid (for the NLC's reaction) dynamic rotation (thanks to the 90° common phase shift) of the total electric field around the normal to cell substrates is thus generating an averaged (in time and space) conical form of electrical potential (see, e.g.,[8, 96]). Thus, a gradient of electric field E is formed (with E being smallest in the center and largest close to activated control electrodes, defining the "periphery" of the activated zone of interest). A corresponding dielectric torque [44, 100], which is proportional to $\Delta\epsilon E^2$ (where $\Delta\epsilon$ is the dielectric anisotropy of the NLC), is then exerted on the local optical axis of the NLC (so called "director", representing the local average orientation of long axis of the NLC's molecules) by E . This torque tends to reorient NLC molecules to align them with the local E , if $\Delta\epsilon$ is positive. Due to the lateral gradient of E , the corresponding reorientation angle of the director is smallest at the center ($x=0$, where x is the radial coordinate) and largest closer to the activated control electrodes ($x = \pm r$, where $r = CA/2$ is the radius of the local lens). Respectively, a refractive index gradient $n_{eff}(x)$ is created for the extraordinary polarized wave [66] :

$$n_{eff}(x) = n_c - \frac{x^2}{2fL} \quad (3.1)$$

where n_c is the effective refractive index value in the center of the lens, f is the focal distance of the generated GRIN lens and L is the thickness of the NLC layer. This transverse modulation occurs thanks to the anisotropy of the NLC :

$$n_{eff}(\theta) = \frac{n_{\parallel}n_{\perp}}{(n_{\perp}^2 \sin^2\theta + n_{\parallel}^2 \cos^2\theta)^{1/2}} \quad (3.2)$$

where n_{\parallel} and n_{\perp} are, respectively, extraordinary and ordinary refractive indices of the NLC ($\Delta n = n_{\parallel} - n_{\perp}$), and θ is the angle between the NLC's director and the wavevector of the probe light. Finally, given the parabolic form of the gradient, an OP may be generated (measured in dioptries, D , or $1/m$), the maximum of which is limited by material (Δn) and geometrical parameters (r and L) of the local lens, [37] :

$$OP_{max} = 2\Delta n \cdot L/r^2 \quad (3.3)$$

Optical metrology tools.

For a quick visual characterization of obtained wavefronts, a first (approximative) approach can be used by placing the NLC cell between two cross oriented linear polarizers with the rubbing direction (defining the ground state orientation of NLC's optical axis) being aligned at 45° with respect to the entrance polarizer's transmission axis. Then, the incident (on the NLC) light generates ordinary and extraordinary waves inside the NLC. The second polarizer (analyzer) projects both polarization components on the same axis (its transmission axis), generating thus transversally changing inferential pattern showing the relative phase shift between two polarization modes (the ordinary wave experiencing a uniform phase shift across the entire NLC), see, e.g. [39, 38]. Thus, two neighboring maximums (fringes) of the obtained interference pattern represent positions where the phase shift, experienced by the extraordinary wave, is equal to 2π .

For a more quantitative approach, the wavefront of exiting, from the lens, extraordinary polarized light (at $\lambda = 633\text{nm}$) was measured by using a relay lens ($F = 50\text{ mm}$) that was projecting the exit plane of the NLC on a Shack-Hartmann (S-H) wavefront sensor (WFS30-5C(M), Thorlabs) with an optimized magnification. Plane wavefront reference was recorded when the lens was in the "off" state ($OP=0$). The wavefront error was then determined by acquiring first 11 zernike polynomials and a least square Zernike fit was done to determine the weight of each aberration. We have already demonstrated in our previous work [96] that we can generate spherical positive lenses with different diameters, ranging from 1.3 mm to 4.55 mm, respectively with OP values of 40 D and 3.5 D, while maintaining rather good RMS aberrations (below $\lambda/3$, closed to limited diffraction $\lambda/4$). It is worth mentioning that the acceptable level of aberrations depends upon the specific application, for example, some mobile imaging devices can accept total RMS values of $0.2\text{ }\mu\text{m}$, while other, e.g., ophthalmic systems, may require significantly smaller values (below $0.1\text{ }\mu\text{m}$).

Square aperture

In most application cases, a circular aperture is used for lenses. However, the specific geometry of electrodes, we are using in the foveal lens, imposes a square shaped working (excitation) zone. In this section, we shall describes the corresponding particularities of obtained dynamic wave fronts and we shall then orthogonalize (project) the Zernike polynomials (usually applied for circular apertures) on our square shaped pupil. Indeed, for a fixed position of the lens center, we can always design the final imaging device to use mostly the central circular part of it (e.g., by using a corresponding diaphragm). However, for the foveal approach, it might be useful to clarify the description method we are going to use. Usually we characterize the wavefront \hat{W} , generated by our lens, with the help of Zernike circle polynomials Z_j , described in polar

(ρ, θ) or Cartesian (x, y) coordinates as a set of orthonormal functions, while the pupil remains circular [21]. \hat{W} is expressed into Z_j with the Zernike coefficients a_j as weights, assuming that the number of base polynomials has a finite value J :

$$\hat{W}(x, y) = \sum_{j=1}^J a_j \cdot Z_j(x, y) \quad (3.4)$$

However, Zernike polynomials are not the best for fitting noncircular pupils and lose orthogonality over such areas. Hence, the Zernike polynomials are not appropriate for wavefront analysis of noncircular pupils. Since other polynomials can be used for the decomposition of the wavefront accros a square aperture, such as 2D Chebyshev polynomials or 2D Legendre polynomials [101], Circular Zernike polynomials could be orthogonalized [102, 103] over square aperture [104, 86]. Square polynomials $S_j(x, y)$ being generated in Cartesian coordinates, the aberration function W for square pupil may be expanded in terms of square polynomials that are orthonormal over the pupil weigted by square coefficients b_j :

$$W(x, y) = \sum_{j=1}^J b_j \cdot S_j(x, y) \quad (3.5)$$

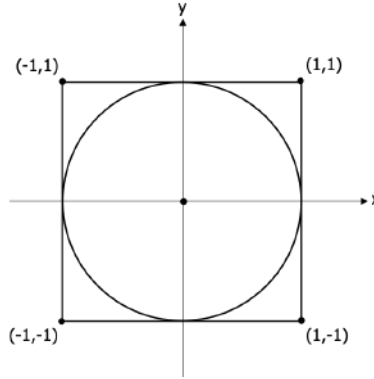


FIGURE 3.2 – Coordinate for a square pupil inscribed outside a unit circle.

In our case, the square aperture has regions that fall outside the unit circle (Fig.3.2), which is measured by our S-H sensor, the side length of the square is a length of 2 and it's area (A) is 4. the square aperture is inscribed outside of a unit circle. From S-H measurement of the circular pupil, we have orthogonalized Zernike polynomials over a square aperture. These polynomials can be obtained by using the Gram-Schmidt orthogonalization process, based on the circle Zernike polynomials : $Z_j(x, y)$ already describe in detail by Mahajan [102].

3.3 Results and discussion

Previously, we have demonstrated that, to generate a centrosymmetric positive lens, the phase shift between signals, applied to peripheral electrodes of top and bottom substrates, must be

maintained to 90° and they must have the same RMS amplitude V [96]. Based on the same principle of LCD pixels, the excitation (molecular reorientation) state is determined only by the RMS value of the voltage difference across its row and column electrodes, regardless of the frequency of the applied signals. From the eq.3.6, we can obtain the resulting RMS amplitude of the voltage between the top and bottom electrodes as equal to $\sqrt{2}V$.

In the current work, we have discovered additional control modes when we have changed independently the 4 voltage values and phase delays. In this control regime, the resulting voltage between the top and bottom electrodes is the sum of two sin waves (of same frequency) with amplitudes (V' and V'') and phase shifts (α and β) as [105] :

$$\begin{aligned} V_{sum} &= V' \cdot \sin(\omega t + \alpha) + V'' \cdot \sin(\omega t + \beta) \\ &= \sqrt{[V' \cdot \cos(\alpha) + V'' \cdot \cos(\beta)]^2 + [V' \cdot \sin(\alpha) + V'' \cdot \sin(\beta)]^2} \\ &\quad \cdot \sin \left\{ \omega t + \tan^{-1} \left(\frac{V' \cdot \sin(\alpha) + V'' \cdot \sin(\beta)}{V' \cdot \cos(\alpha) + V'' \cdot \cos(\beta)} \right) \right\} \end{aligned} \quad (3.6)$$

By changing independently voltage and phase differences between crossing electrodes, it was possible to additionally modulate the wavefront's shape (see hereafter).

Tunable astigmatism. In this part of our work, we have tried to control the primary astigmatic aberration (further noted as AST). We have investigated the AST oblique at 45° (AST45) and the AST horizontal/vertical at $0^\circ/90^\circ$ (AST0/90). In the following section, we first discuss the influence of applied voltages on the Zernike coefficient for AST0/90. Namely, we have started by applying a voltage difference ΔV between top and bottom substrates (with $\Delta V = V_{top} - V_{bot}$, where $V_A = V_B = V_{top}$ on the top substrate and $V_C = V_D = V_{bot}$ on the bottom substrate). Figure 3.3(b) shows the experimentally obtained interference images confirming the desired distortion of the obtained wavefront along the horizontal and vertical axes, corresponding to x and y axes. Deforming the lens along its x-axis, where bottom electrodes' amplitude (V_{RMS}) is higher than the amplitude, applied to the top substrate, corresponds to $\Delta V < 0V$ and results in an increase of the Zernike coefficient a_6 (see Fig.3.5a). In contrast, distorting the lens parallel to its y-axis, where bottom electrodes' amplitude is lower than the top one (corresponds to $\Delta V > 0V$) causes the same coefficient to decrease. The absolute values of this change in a_6 coefficient are approximately the same, as summarized in Table 1 ; in this table, ' ΔV ' refers to the difference in voltage between top and bottom substrates (in V_{RMS}). The a_6 coefficient evolves linearly with the applied voltage difference, its sign depending on the axis, related to the sign of ΔV , if $V_{top} > V_{bot}$, $a_6 < 0\mu m$. Otherwise, if $V_{top} < V_{bot}$, then $a_6 > 0\mu m$.

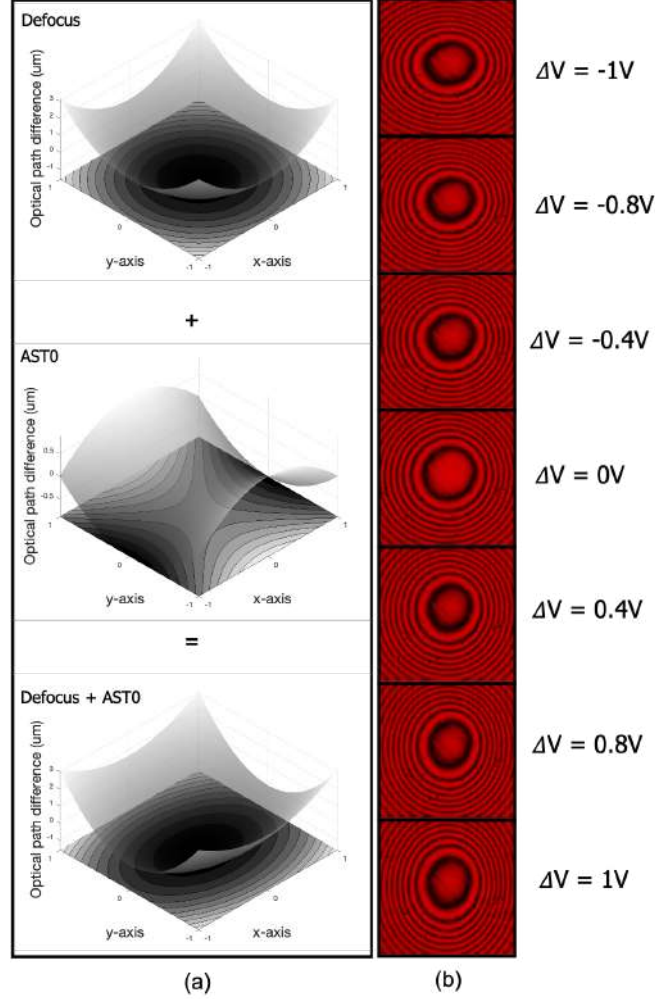


FIGURE 3.3 – (a) Digitally reconstructed wavefronts by using square Zernike polynomials (described in the main text), coupling AST0 and defocus from $a_6 = 0.375\mu\text{m}$ and $a_4 = 1.7\mu\text{m}$, respectively; (b) Experimentally obtained polarimetric images, confirming the generation of tunable vertical/horizontal astigmatism (AST0) with amplitude difference ΔV applied between top and bottom electrodes.

Futhermore, we have also demonstrated (in Fig.3.4(b)) that the adjustment of the phase delay between 4 signals deforms the lens along the oblique axis (AST45) and induces an increase/decrease of the corresponding Zernike coefficient a_5 (cf. Fig.3.5b), with positive and negative signs depending of axis orientation $+45^\circ$ or -45° , respectively. Here, we can see also the proportionality between the phase difference on top/bottom substrates and the corresponding coefficient values.

Then, we have decided to change the relative phase shift compared to the standard spherical lens approach, where signals, applied to top and bottom electrodes, are always phase shifted by 90° . As example, we show the case where the phase delay between substrates is set to 60° phase shift. Signals of the top substrate were maintained at the initial configuration $\varphi_a = 0^\circ$

and $\varphi_b = 180^\circ$, while the phases of signals, applied to the bottom substrate, were changed to $\varphi_c = 60^\circ$ and $\varphi_d = 240^\circ$. Correspondingly, based on eq.3.6, the voltage along the four corners of the lens changed; it became $V_{c/a} = V_{d/b} = \sqrt{3}V$ and $V_{c/b} = V_{d/a} = V$. This allowed us controlling the AST45. To simplify the configuration notation, we considered $\Delta\varphi$ as phase variation from the initial phase delay between top/bottom electrodes, $\Delta\varphi = \varphi_c - 90^\circ$, in this example $\Delta\varphi = -30^\circ$. It is important to notice that here we have maintained the phase shift between two parallel electrodes at 180° during all the experiments.

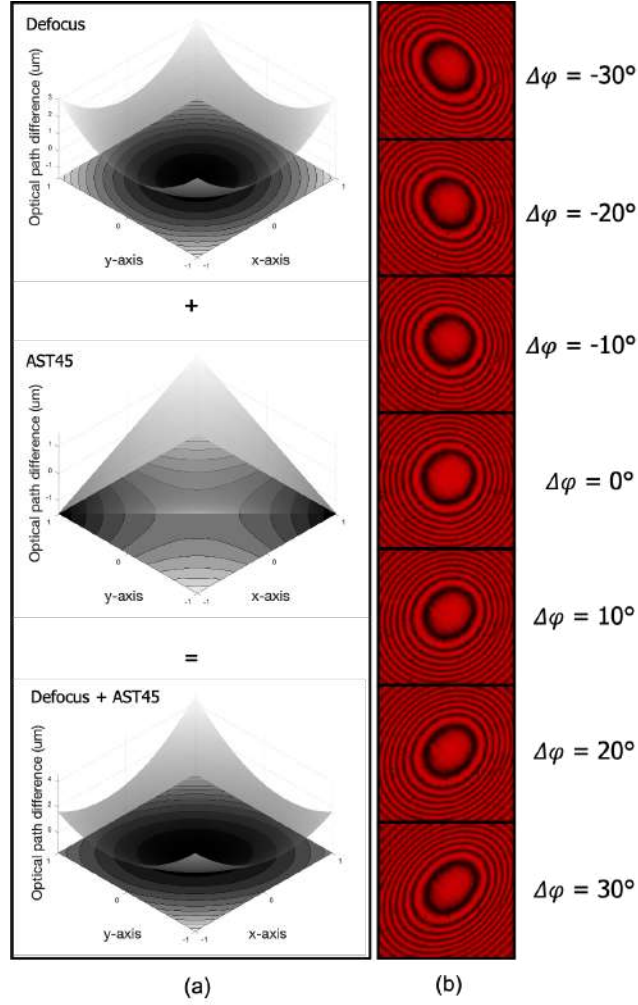


FIGURE 3.4 – (a) Digitally reconstructed wavefronts with a square aperture, coupling AST45 and defocus with $a_5 = 0.5\mu m$ and $a_4 = 1.7\mu m$, respectively; (b) Exeprimental generation of tunable oblique astigmatism (AST45) with phase shift control $\Delta\varphi$.

The astigmatism tunability was demonstrated by keeping the defocus (optical power) and other RMS aberrations almost constant (see Fig.3.5). In this case, the voltage and phase differences have to be symmetric from the initial diopter settings (for demonstration here we have normalized the initial OP to 1D). Figure 3.6 and Table 3.1, summerize our demonstration that

the AST45 and AST0/90 can be tuned independently. The independent control parameters are the amplitude of the electric potential for AST0/90 and the phase delay of the signals for AST45 (thanks to the difference between top and bottom electrodes in both cases).

The summary of results obtained in different driving modes is presented in Fig.3.5. Thus, we can see how evolve Zernike coefficients (AST45 = a_5 and AST0 = a_6) and the corresponding OP and RMS aberrations for various amplitude (a) and phase (b) settings. The details of these settings are respectively shown in tables (c) and (d).

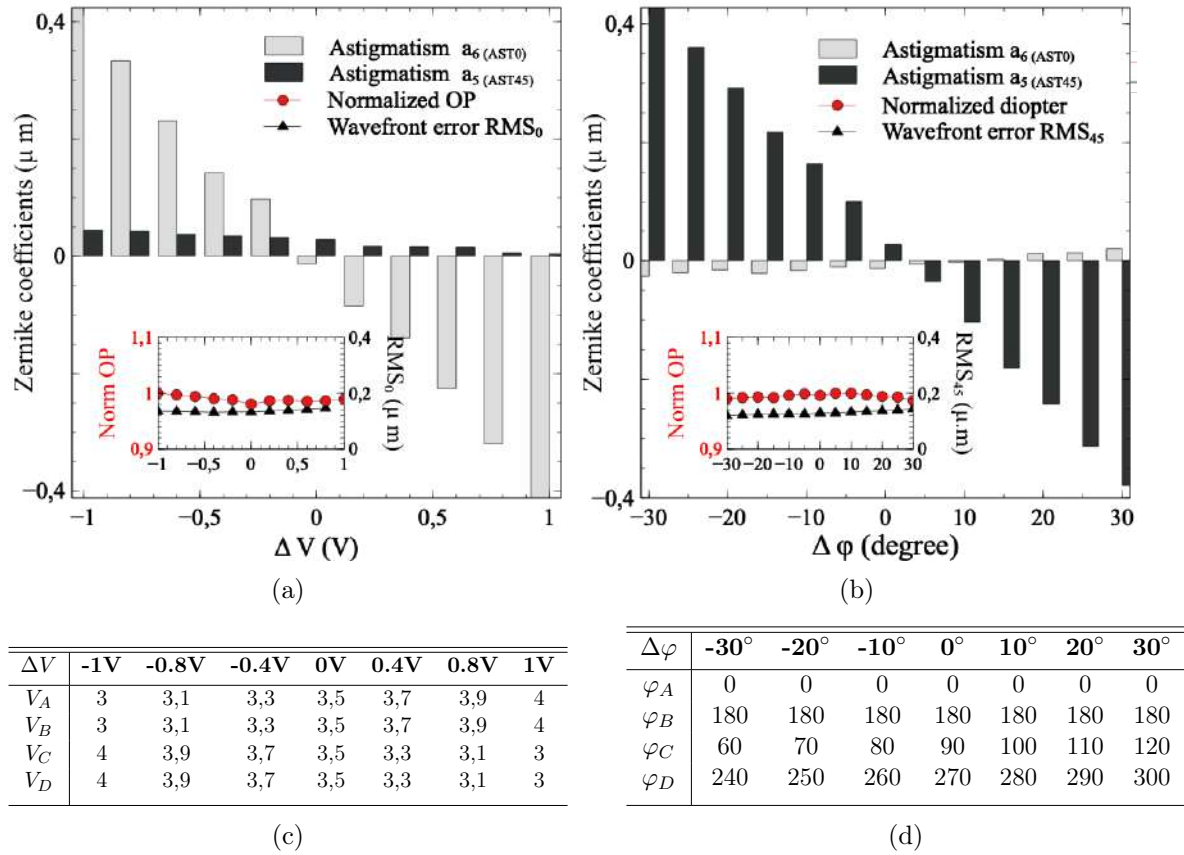


FIGURE 3.5 – Different driving modes and corresponding astigmatism Zernike coefficients (AST45 = a_5 and AST0 = a_6); (a) and (b) Each bar shows the dependence of the Zernike coefficient's variation on the applied electric field. Optical power (OP) variation is represented by red circles and the total RMS aberrations (without considering astigmatism and defocus) are plotted by black triangles; (c) and (d) Amplitudes and phase settings on electrodes A, B, C and D for AST45 and AST0 generation, respectively.

Further, we have measured Zernike coefficients a_5 and a_6 of AST0/90 and AST45, respectively. The S-H has measured over an inner circular pupil of the square aperture lens, and we have converted those coefficients into Square coefficients b_5 and b_6 . During all these experiments, we have maintained the diopter constant and increased or decreased the astigmatism coefficients. Moreover, without considering primary astigmatism, the aberration wavefront error

RMS still remained fixed. The combination of both approaches allow us to generate free-axis astigmatism. In this control regime, we have simultaneously generated AST0/90 combined with AST45, an independent control on $a_5 + a_6$ values inducing a free rotation of AST, see arbitrary axis generation in Fig.3.6.

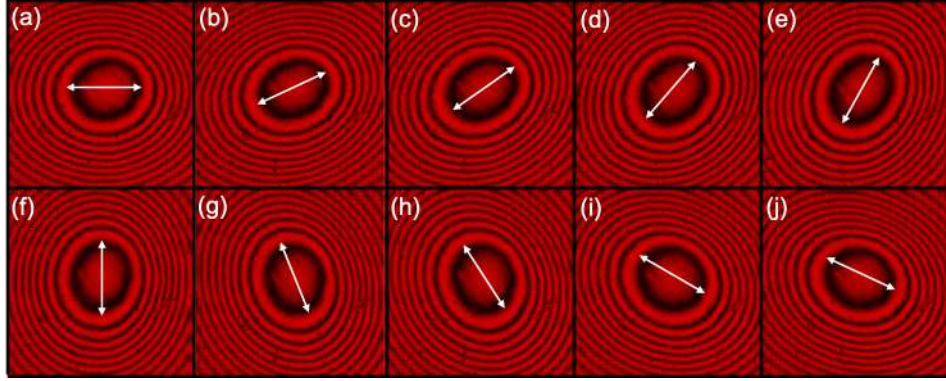


FIGURE 3.6 – Examples of generating astigmatism with precise control along arbitrary (desired) directions.

TABLE 3.1 – Amplitude and phase settings between orthogonal electrodes used to generate astigmatism along the desired axis.

Fig.	a	b	c	d	e	f	g	h	i	j
$Axis(^{\circ})$	0	25	35	49	61	90	112	123	150	155
$\Delta\varphi$	0	+10	+15	+15	+10	0	-10	-15	-15	-10
ΔV	-1	-0,8	-0,4	0	+0,4	+1	+1	0.2	-0.6	-0.8

Tunable tilt. We have then proceeded to the demonstration of simultaneous control of tilt and defocus modulation. These configurations are chosen for demonstration purpose with $\Delta V_T = 0.8V$, showing several combinations of $Tilt_x$, $Tilt_y$ combined to defocus. We have measured the corresponding Zernike coefficients a_2 , a_3 and a_4 under different Tilt conditions, see Fig.3.7.

The distortion is a tilt, depending on the field. The idea behind the proposed system is to use an active optical element to adjust in real time the distortion of the system. Distortion is not an aberration, which affects the image quality by changing the spot size, but an aberration that changes the local lens magnification.

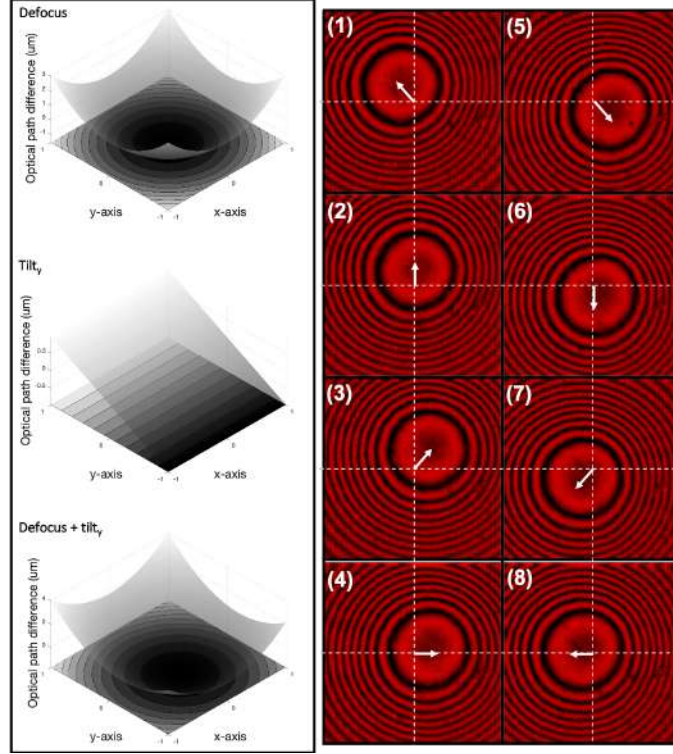


FIGURE 3.7 – a) Digital wavefront reconstruction of $Tilt_y$ $b_2 = 0.8\mu m$ and Defocusing $b_4 = 1.7\mu m$ aberrations; b) Experimental demonstration of Tilt and Defocus control. These configurations are chosen for demonstration purpose with $\Delta V = 0.8V$, showing several combination of Tilt x + Tilt y + Defocus.

As we can see, the center of the concentric interference fringes changes with the relative lateral shift (see also similar tuning in [106, 107]). The corresponding excitation voltages are shown in Table 3.2.

TABLE 3.2 – Amplitude setting on electrodes A, B, C and D for Defocus + Tilt generation.

Fig.	1	2	3	4	5	6	7	8
V_A	3.2	3.5	3.8	3.8	3.8	3.5	3.2	3.2
V_B	3.8	3.5	3.2	3.2	3.2	3.5	3.8	3.8
V_C	3.2	3.2	3.2	3.5	3.8	3.8	3.8	3.5
V_D	3.8	3.8	3.8	3.5	3.2	3.2	3.2	3.5

Negative lens. The above-description illustrates how we can generate various positive lens profiles. While these are rather advanced wavefronts, the proposed design allows generating much richer wavefronts. This includes also bipolar responses (with both positive and negative OP values) [108, 74, 95]. Such a bipolar response may add significant capabilities in future applications (including the compensation of myopia, along with other types of all possible aberrations of human vision).

While we realize that it will require a separate more detailed study of this bipolar capability

of our lens, we think that it might be useful to make the demonstration of its feasibility here. For this demonstration, we have used a so-called dual frequency NLC (DFNLC). As it was already described [60, 109], a DFNLC exhibits a frequency dependent inversion of the sign of its dielectric anisotropy $\Delta\epsilon$. Thus, an electric field with a high frequency F that is above the inversion (so-called *crossover*) frequency f_c forces the NLC director to realign in the perpendicular (to the field) plane since $\Delta\epsilon$ is negative. In the meantime, a field with low frequency f (below the f_c) is orienting molecules along the field [110] since the $\Delta\epsilon$ is positive. If both high and low frequency fields are applied almost simultaneously, then the NLC responds essentially to the difference of the opposing torques, and settles at a corresponding equilibrium. In our demonstration, the low frequency electric field propagates well in the transverse plane and forces molecules to align (almost uniformly) perpendicular to the substrates of the cell. Then a high frequency field, controlled by using standard phase shifts, as described earlier [8, 96], partially reorients molecules back to the parallel state in areas of the cell that are closest to the peripheral (activated) electrodes. Thus, we can start from a planar aligned cell (in the ground-state) and obtain lenses with negative OP. In addition, by keeping external (beyond the peripheral) electrodes on the ground state, we can obtain a highly localized negative lens, which may be tuned, scaled, and moved through the entire area, see few examples in Fig.3.8.

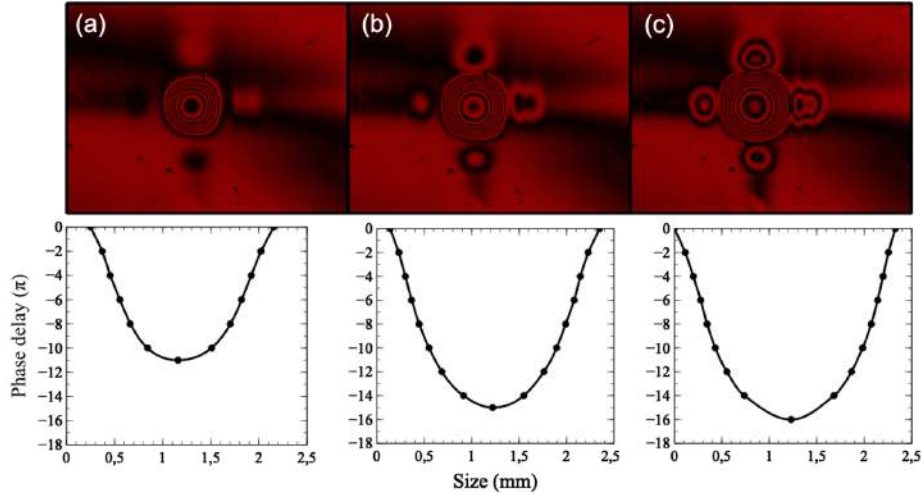


FIGURE 3.8 – Demonstration of the possibility of generating and controlling a tunable negative lens with CA=2.3 mm (a-c : top pictures show the polarimetric images, obtained for different optical power values, while the bottom curves show the corresponding reconstructed waveforms (obtained from polarimetric data)).

In the example of Fig.3.8, a local lens of CA=2.3 mm is shown. The high frequency drive signal was fixed at $F=30\text{kHz}$ and its amplitude was $V_F = 6 V_{RMS}$, while the low frequency was $f=20\text{Hz}$ and we have only adjusted its amplitude V_f to change the OP of the lens. The 3 examples here are obtained for the values of V_f equal to $3.2 V_{RMS}$, $3.5 V_{RMS}$ and $3.8 V_{RMS}$ for figures a, b, and c, respectively. External (beyond peripheral) electrodes are in the ground

state.

Here, our preliminary results show that the ITO serpentine resistivity must be further optimized to help the electric potential with high frequency to propagate further towards the center of the local lens (from peripheral electrodes). With this method, we are able to scale and to generate negative tunable lens with free axis astigmatism too.

3.4 Summary and Conclusions

We have used the same design as in our previous work [96], but we have used different control approaches that allowed us the generation of advanced wavefront control capabilities. Indeed, a rather high level of independent control of aberrations was achieved by a relatively simple technique : applying different voltages and phase delays to 4 control electrodes (defined by the zone of interest). For example, among others, we have proposed a method to generate an astigmatism with almost arbitrary axis and arbitrary values and we have experimentally demonstrated the possibility to control the magnitude and the orientation of AST vector axis. Moreover, the tuning focus range could be extended by increasing or decreasing electrical amplitude signals on four peripheral electrodes.

The presence of astigmatism in an optical system implies that rays of the sagittal plane and rays of the meridional plane are focused at different planes perpendicular to the optical axis. This results in a directional blurring of the obtained image. Thus, the accurate control of astigmatism value and orientation (reported here) will allow controlling wavefront aberrations of many optical systems, especially for vision (eye) correction. If we consider an eyeglass prescription, it consists of spherical power D_r , cylindrical power C_r (related to astigmatism value) and an axis direction θ_r diagnostic. An estimation of the direction of astigmatism axis (θ_r in degrees) and their OP from the measured Zernike coefficients may be easily obtained [111].

We have also demonstrated a variable tilt by applying a simple electrical modulation technique. All these demonstrations were done on arbitrary positions over the entire clear aperture.

We think that the above mentioned capabilities might be also very useful for augmented and virtual reality headsets, among others, to address the ophthalmic eye-glass or vergence-accommodation [112] problems, which are subject of active research efforts today [113].

Despite the non circular pupil of the device, we have used a method of transforming the Zernike coefficients for quantitative wavefront analysis over square shaped apertures. In this case, outer square coefficients can be derived from Zernike coefficients.

Futhermore, we have also demonstrated (in a very preliminary way) the possibility of generation of highly localised (throughout the entire surface of the device) negative lenses by using DFNLIC. It will also allow obtaining faster responses, if needed by the specific application.

We think that this device has rather unique features to be discovered yet. Its spectral, dynamic and other technical characteristics (e.g., haze) are very similar to traditional single "fixed" aperture lenses (see, e.g., [66]). In addition, its manufacturing is simple (single lithography step

is required) and can be done in a very cost-effective way.

There is no doubt that it will enable a significant enhancement of adaptive capabilities of various optical systems and will find multiple applications in imaging and/or vision. The specific choices of parameters of the lens (electrodes' width and spacing, sheet resistance of the ITO, the type of the NLC, etc.) must be done in the framework of a specific target application to optimize its performances.

Acknowledgments

We would like to acknowledge LensVector inc., the Natural Sciences and Engineering Research Council of Canada (NSERC, 05888) and the Canada Research Chair in Liquid Crystals and Behavioral Biophotonics (CRC, 230212) for their financial support of this work.

Funding

Natural Sciences and Engineering Research Council of Canada (05888); Canada Research Chairs (230212).

Disclosure

Authors have no conflict of interest to disclose.

Data availability

Detailed data, underlying the results presented in this paper, are not publicly available at this time, but may be obtained from authors upon request.

DYNAMIC PRESBYOPIA CORRECTION IN THE MACULAR FIELD OF VIEW BY USING A LIQUID CRYSTAL LENS

Bégel Louis¹, and Galstian Tigran^{1,2,3}

¹ Center for Optics, Photonics and Laser, Department of Physics, Engineering Physics and Optics, Université Laval, 2375 Rue de la Terrasse, Quebec, G1V 0A6, Canada

² LensVector inc., 2307 Leghorn Street, Mountain View, CA 94043 USA

³ PATQER Photonique inc., 2375 Rue de la Terrasse, Quebec, G1V 0A6 Canada

A large aperture matrix of tunable liquid crystal lenses (MTLCL) is used for dynamic presbyopia correction. The special electrode design and driving method allow the activation of local lenses at arbitrary lateral positions of the MTLCL. First the study of tunable wavefronts, that can be generated by such a device, is presented. Then, the image quality at different viewing angles and distances is quantified. A driving algorithm is also developed to increase the speed of focusing. It is shown that this device may provide continuous focus tunability (from 0 to 2.5 Diopters), react within 0.5 s, operate with relatively low voltages (<5 V), and enable diffraction limited on-axis aberrations. Finally, the results of a comprehensive evaluation of its performances with human subjects are reported, comparing the visual acuity (VA) achieved by using the proposed in this project against the natural human VA for objects in the near field.

4.1 Introduction

As the global population ages, a significant challenge in ophthalmic health emerges : presbyopia. This age-related condition, affecting the eye’s ability to focus on nearby objects, is a consequence of the loss of the capability to dynamically deform the crystalline lens (hardening, loss of strength or elasticity, etc. [15, 114]), typically occurring in individuals around their mid 40s to 50s [115]. Presbyopia is more than a mere inconvenience ; it represents a profound shift in the individual’s visual experience, impacting daily activities and overall quality of life. Currently, over a billion people worldwide grapple with presbyopia [116] and this number is expected to rise with the aging demographic. In all attempts to address this problem, the ability to seamlessly switch between near and far vision correction is a critical issue, addressing the need for a more natural and wide-ranging visual experience. Traditional corrective approaches, such as single vision, monovision, bifocal, and progressive lenses [117], offer partial solutions but are fraught with limitations. For example, fixed discrete optical power (OP) zones can cause image jump and a reduced natural field of view (FoV), while progressive lenses, despite their seamless power progression in vertical direction, induce peripheral astigmatism [118] and often require head movement for clear near vision. Furthermore, the inconvenience of managing multiple pairs of glasses for different visual needs, and the physical discomfort associated with some corrective methods, underscore the need for more innovative and adaptable solutions.

An interesting solution for presbyopia would involve restoring the flexibility of the crystalline lens or employing a type of focus-adjustable lens. Currently, surgical techniques are being researched that focus on either reducing the stiffness of the crystalline lens or replacing it with a flexible intraocular lens [119]. However, these surgical methods come with the inherent risks of invasive procedures and are predominantly in the experimental phase, with long-term efficiency and reliability yet to be established. A significant limitation of the methods described above is that they offer only a fragmented or distorted correction of vision, which is not natural. For a true restoration of normal vision, active correction of accommodation may be necessary. This means that the correction must be responsive to the distance of the object being observed, without compromising the visual field or requiring adjustments in the viewing angle. To achieve this, the focus-tunable element could also be placed outside the eye. A variable OP change of 3.0 Diopters (D, the inverse of focal distance in meters) is needed here [119]. Efforts to create such variable-focus eyeglasses led to several interesting solutions, such as sliding Alvarez lenses [120] or liquid filled lenses [121]. Subsequent enhancements in the actuation mechanism of these lenses have been proposed [122, 123].

To avoid mechanical movements or deformations, variable-focus lenses can also be made by using other technologies, e.g., liquid crystal (LC) lenses [124, 125], deployed as contact lenses [72] or intraocular lenses [126]. However, for wide-aperture optical systems (such as human vision that requires large-diameter optics) LC lenses face their own drawbacks. Namely, if the aperture size of an LC lens increases while the LC layer’s thickness remains constant, the

OP decreases according to a quadratic relationship. Consequently, active research is being conducted to develop LC Fresnel lenses [127, 128, 129, 82, 81]. However, the manufacturing of LC variable-focus lenses with apertures in the the range of 25 mm - 50 mm (for eyeglasses) remains a challenge. Fresnel zones' boundary scattering, diffraction effects between electrodes, capacitive effects, etc. remain significant limitations [130, 95, 124, 125].

At the same time, it is well known that the human vision is foveal, based on a small area that provides the sharpest visual acuity (VA) needed for detailed tasks, such as reading. It provides images focused at different distances along the optical axis and is, therefore, a matter of central "foveal" viewing. Therefore, a new electrode structure has recently been developed with serpentine electrodes in the LC cell [131, 96, 132] capable of locally activating lenses in a wide FoV (in arbitrary lateral positions) with variable diameters and focal lengths.

In this work, our primary aim is to conduct an evaluation of the potential of using such focus-tunable eyeglasses (based on this new approach) as a method of correction for presbyopia by correcting exclusively the foveal and macular FoV, without noticeably altering the rest of the FoV. Thus, preliminary characterization work is presented, describing the wavefront, OP, aberrations and speed of the lens. Finally, the results of human vision correction tests (performed on 7 patients) are presented.

4.2 Design and operating principle of the lens

The operating principle of the proposed matrix of tunable LC lenses (MTLCL) has already been described in detail in [96, 132]. Its schematic diagram is shown in Fig.4.1 (c). The structure consists of a planar LC cell formed by two transparent substrates (usually glass, but can also be plastic) with transparent conductive coatings (on their inner surfaces) made of a thin layer (approximately 30 nm thick) of indium tin oxide (ITO). Using the photolithography process, serpentine ITO electrodes with a width of 35 μm and a gap of 5 μm are patterned orthogonally on both substrates (see Fig.4.1 (a), (b)). For the moment, this patterning creates a very weak diffraction from etched edges of the ITO. However, this is not noticeable and can be mitigated later by using ITO with index matched layers. While the number of control electrodes (external contact points) can be varied, the current design features 40 control contacts per substrate, with a total active area of 25 mm \times 25 mm. A resistance of 1 M Ω was measured between neighboring contact electrodes spaced 0.64 mm apart [96]. These serpentine ITO surfaces are coated (on both the upper and lower substrates) with a parallel-alignment polyimide film (from Nissan) and uniformly rubbed. These substrates are then aligned parallel to each other to form a sandwich with a gap that is maintained by polymer ball spacers (with an average diameter of 60 μm). The cell is filled with a nematic LC (NLC) material, MLC-2048 (from Merck, Germany), [133, 134], by capillary action. This material was selected, first of all, for its well-documented dielectric and viscoelastic properties (see hereafter).

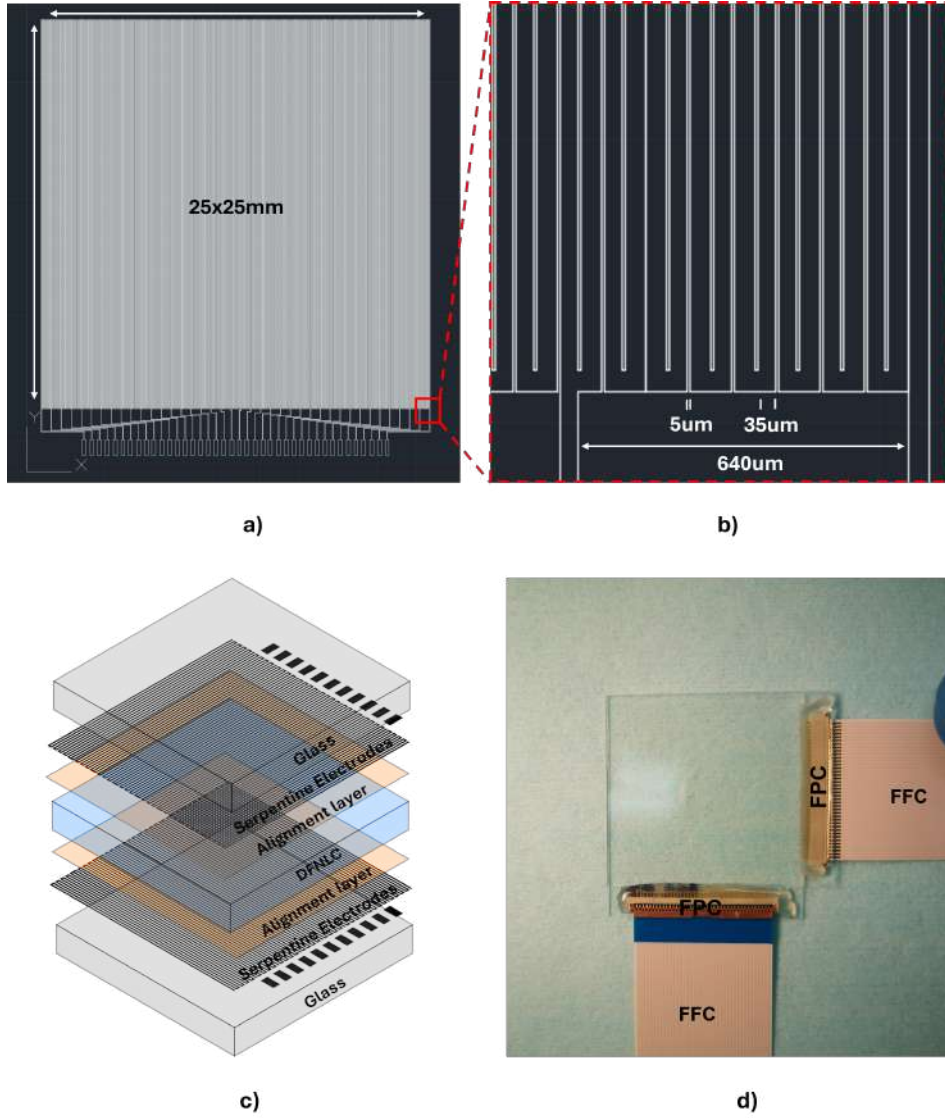


FIGURE 4.1 – a) Schematic top view of transparent electrodes of the lens. b) Zoom on the corner of the patterned electrodes and c) Schematic 3D view of the lens. External contact electrodes (dark rectangles) are arranged at a constant distance. d) Top photograph of the lens with flat printed connectors (FPC) and flat flexible cables (FFC).

In order to generate four control electrical signals (described in [96, 8]), a driving module has been designed and built. It consists of a custom electrical phase shift waveform generator. A micro controller generates two high-frequency waves F_1 and F_2 (here, with the same specific frequency values F but with 90° phase shift Φ), as well as one low-frequency f signal (typically 20 Hz) as an offset component. Buffer/inverter pairs create balanced positive(P)/negative(N) versions of these signals F_{1P}/F_{1N} (Φ $0^\circ/180^\circ$), F_{2P}/F_{2N} (Φ $90^\circ/270^\circ$), and f_P/f_N (Φ $0^\circ/180^\circ$). These 6 signals are then amplified up to desired values of U for high frequency signals and U_{off} for low frequency (offset) signals to produce balanced *sin* waves. These amplified signals

are combined (as detailed in [96]) to produce 4 signals, applied to 4, dynamically changeable, peripheral contacts A, B, C and D, as follows : A ($F_{1P}+f_P$), B($F_{1N}+f_P$), C($F_{2P}+f_N$) and D($F_{2N}+f_N$). Finally, 160 1/8 multiplexers are used to generate the drive outputs. The multiplexers can select an open-circuit (floating), one of the A/B/C/D signals, or the ground to be applied to MTLCL's electrodes.

The authors have previously demonstrated the capability of this device to locally create and adjust (through a large aperture) a variable focal length lens without noticeably disturbing the rest of the FoV [96]. That device was using a polarizer. Here (in the last section), results are presented with an electrically tunable polarizer-free MTLCL (full-lens, built by using two LC layers, see hereafter), which is more appropriate for ophthalmic applications. Indeed, due to the anisotropic properties of the NLCs used here, the lens with a single NLC cell (or so-called, "half-lens") exhibits polarization-dependence (it is focusing only the extraordinary polarization component of light). For ophthalmic applications, it is crucial that these lenses operate with unpolarized light. To achieve this, two identical NLC layers must be assembled together [135] (what is called here a "full-lens") with their ground state molecules being oriented in orthogonal planes.

Such a lens is schematically demonstrated in Fig.4.2. Small orange ellipses schematically represent NLC molecules. The longer the ellipse, the larger is its projection on the drawing plane. Thus, in the ground state, Fig.4.2 (a), molecules of the first sandwich (on the left) are perpendicular to the drawing plane, while molecules of the second sandwich are in that plane (oriented vertically). For the specific choice of positions of target objects (letters E and F), they appear blurry on the plane of the retina if the lens is in the ground state, Fig.4.2 (b). Figure 4.2 (c) demonstrates the case when an appropriate local lens is activated to focus the letter E. In this case, the letter F (which is out of the region of interest, RoI) appears blurry on the retina. In contrast, Fig. 4.2 (d) demonstrates the case when the neighboring local lens is activated to focus the letter F. In this case, the letter E (which is now out of the RoI) appears blurry on the retina.

The optical performance of half and full lenses are very similar. For example, the maximum achievable range of OP is still the same, defined by the birefringence of the NLC material, its thickness and the local lens diameter (often called clear aperture, CA), [96], see, eq.4.2. The main question here is how to insure that the two half lenses (NLC layers) of the full lens focus at the same focal plane to avoid image degradation. Indeed, two orthogonal polarized components may be focused at different distances, generating thus, so-called "polarization aberrations" [89]. However, using relatively thin substrates (particularly internal ones, see Fig.4.2) allows achieving very good results [66, 126].

The choice of the working CA of the local lens also is crucial for ophthalmic applications. In human vision, the VA decreases rapidly from the fovea to the periphery due to the decrease of the cone photoreceptor density [2]. At the center of the fovea, VA is 1.0 (ideal value for

an average observer ; while the value of 1.5 would be more common), associated with what is called as 20/20 vision. Moving towards the periphery of the macula, VA drops to approximately 0.31. Beyond a 60° deviation from the fovea, VA approaches zero [2]. Due to this decrease beyond the foveal area, we can limit the CA of the local lens while moving it across the entire lens matrix. Obviously, an eye tracking capability must be provided with such a lens to follow the eye movements (see hereafter).

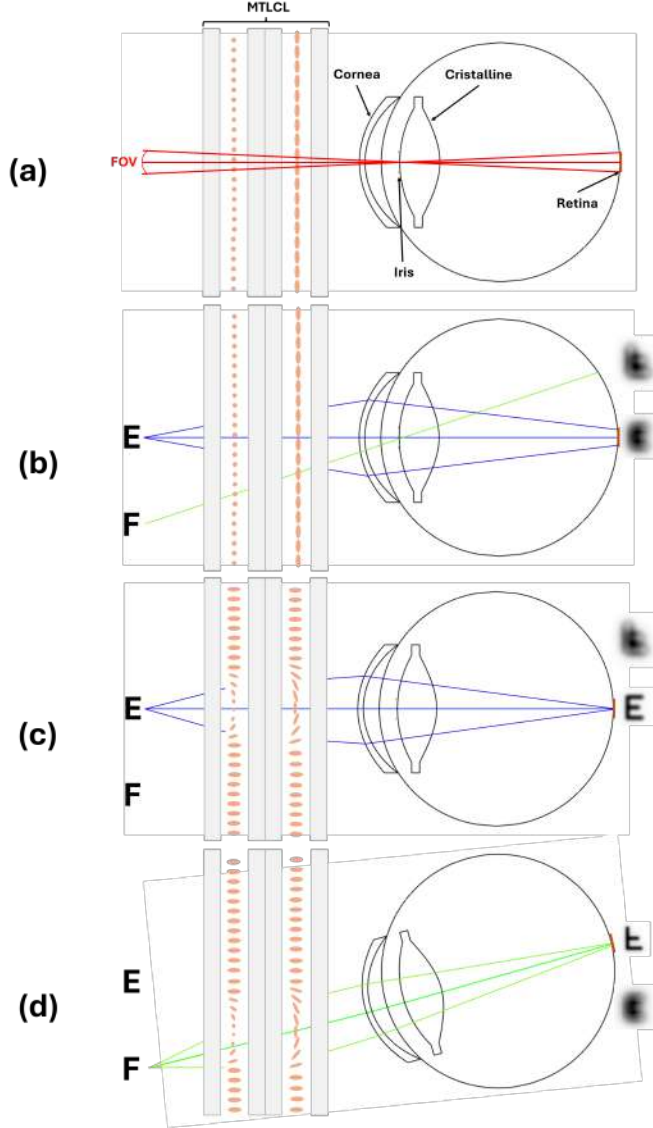


FIGURE 4.2 – Schematic representation of the proposed MTLCL with two (cross-oriented) LC layers (sandwiched between two flat substrates and laminated together) with dynamically changing positions of local lenses following the region of interest (RoI) for a human eye. The orange ellipses represent molecules. a) The limited field of view (FOV) focusing on the retina, with the tunable lens size (local CA) necessary to adjust the focus on the retina. b) The focal shift on the retina with a presbyopia eye. c) Local lens activated in the RoI to bring in focus the letter E, while keeping uniform the periphery (under the red colored electrodes). d) The same as above but for the letter F.

Correspondingly, the CA of our local lens was optimized to cover the total FoV of the macula. Aligning the optical axis to the center of the macula, its FoV, seen from the air, can be approximated as [136] :

$$FoV = 2\sin^{-1} \left(\frac{L_m n_{avg}}{\sqrt{L_m^2 + 4L_e^2}} \right) \quad (4.1)$$

where L_m is the size of the macula and n_{avg} is the average refractive index of the eye. Given $L_m = 5.5$ mm and $n_{avg} = 1.369$ [137], FoV is around 17° - 18° . Usually, eye glasses are placed at $D \approx 16$ mm from the eye, and the MTLCL is supposed to be attached to them. Thus, to adequately cover the retina and macula FoV, the CA of the local lens on the MTLCL must have a diameter greater than $CA > 5.1$ mm.

4.3 Experimental results

Image quality tests

The characterization of the lens' performance began by using a Shack-Hartmann wavefront sensor (SHWFS). It allows the measurement of key optical properties, including the focal length and aberrations under various applied voltages. A continuously working (CW) He-Ne laser (operating at 632.8 nm) provided the probe beam at normal incidence on the lens. The SHWFS captured the probe's wavefront at the output of the tunable lens (a fixed relay lens was used to create the image of this output on the microlens array of the SHWFS).

Initial measurements were performed with zero applied voltage for the calibration of the SHWFS, followed by incremental voltage applications with wavefront recordings at each step. The results obtained (Fig.4.3) demonstrate the relationship between the applied voltage and the focal length of the lens, as well as the corresponding values of astigmatism, coma, and spherical aberration. Usually, root mean square (RMS) aberrations are used to assess the quality of the lens by quantifying how much the lens distorts the wavefront of light (with respect to the desired one, e.g., spherical) passing through it. This is necessary for applications, such as ophthalmic lenses, where minimizing aberrations is essential for clear vision correction in real-time. RMS aberrations at the level of $\lambda/4$ are commonly cited as an acceptance threshold [138, 139]. An optical system with RMS wavefront error less than $\lambda/4$ is generally considered to be performing at a level where diffraction effects dominate over aberrations. This is often used as a practical criterion for good optical quality.

Figure 4.3 shows results obtained for CA values larger than required (5.2 mm, 5.85 mm and 6.5 mm). As can be seen, 2.5 D (diopter correction to be able to correct 85% of presbiopic eyes [119]) can be reached while still keeping optical aberrations at a rather low level. All voltages hereafter are presented in their RMS values. It is worth mentioning that the MTLCL acts like a capacitive charge. Its electrical current and power consumption are very low [126] and there is no noticeable ohmic heating.

Thus, the MTLCL shows a good potential for ophthalmic applications, where a specific RoI may be observed with higher quality within the entire FoV of the local lens.

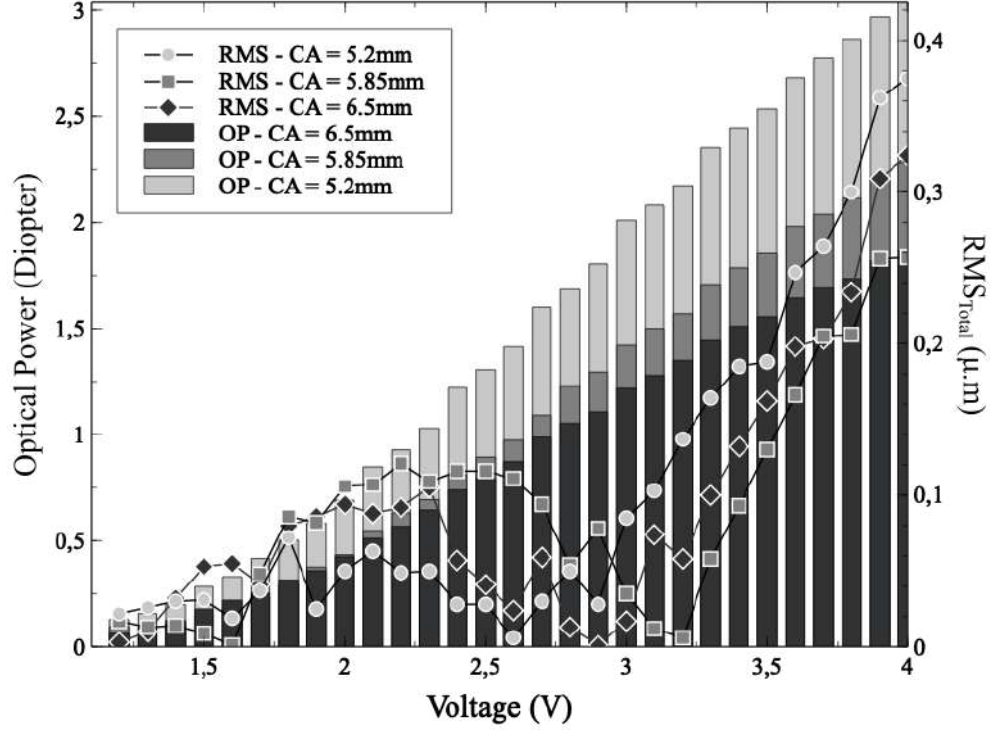


FIGURE 4.3 – Excitation dependencies of RMS aberrations and OP values for various sizes of the clear aperture of the local lens.

Figure 4.4 is qualitatively demonstrating how the local lens may bring into focus various RoIs (a- in the center and b- shifted towards the top left) of a target image consisting of a 2D array of small white squares. The dashed white square demonstrates the total MTLCL area, FFC 1/2/3 and 4 correspond to the flat flexible cable positions, which were activated to address electrodes to create the local lens in the Fig.4.4 (a).

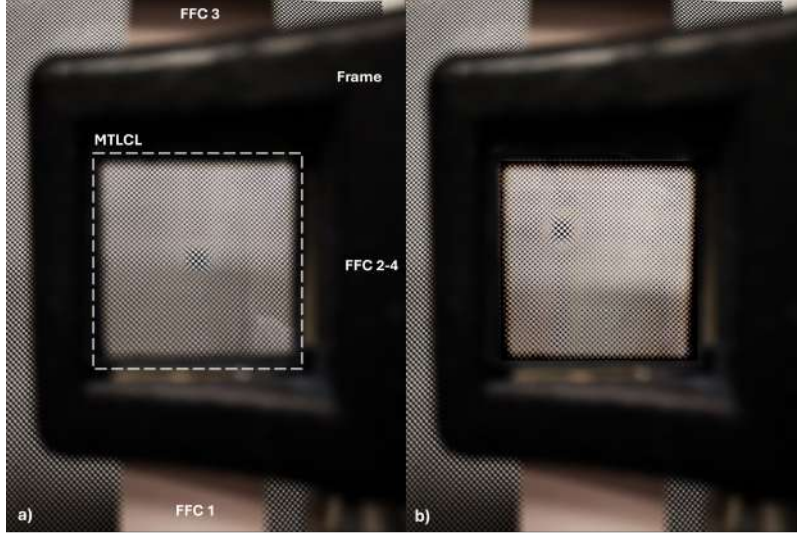


FIGURE 4.4 – Comparative images of a target object (2D array of white squares) formed with the use of the MTLCL for different regions of interest, a) in the center and b) shifted to the top left. Dashed square corresponds to the MTLCL area. FFC1/2/3 and 4 correspond to the flat flexible cable positions activated to create the lens in a).

Then, the lens was used to perform more quantitative image characterizations. To this end, six targets (binary black and white patterns) of multiple lines pair sizes were placed simultaneously at 100 cm, 60 cm, and 35 cm from the MTLCL (which was placed in front of a raspberry pi HQ Camera, coupled with a 16 mm objective) at different viewing angles (to ensure that all these targets are within the total FoV of the camera, Fig.4.5 (a)). The camera was adjusted in order to mimic (approximately) the human eyes with presbyopia. Namely, for each distance, the smallest feature (printed in our experimental charts) corresponds to 20/20 vision, that is, if we can differentiate the minimal feature (a black bar) then it corresponds to 1 arcmin. When the OP of the MTLCL was 0 D, the target at 100 cm (center/top) was in focus and thus could be recorded with good quality, Fig.4.5 (a). At the same time, all other targets are out of focus. When the OP of the LC lens was 1.5 D ($CA = 5.2$ mm), target 2 (placed at 60 cm on the left) appeared in focus, Fig.4.5 (c). When the OP of the local LC lens was tuned to 2.5 D, then target 1 (placed at 35 cm in the center) became clear, Fig.4.5 (b). These targets allowed us to extract the quantitative information (modulation transfer function or MTF) about the contrast enhancement with corresponding focus correction (shown in Fig.4.5).

As can be seen, noticeable improvement is observed for the MTF values when local lenses are activated. For example, at 0.8 cycles/mm, the growth of the MTF is by an approximate factor of 2 for target 1, while this factor is 4.4 for target 2. On average, at this point, they are only at 24% below the diffraction limit. According to the authors, this is a rather significant improvement. It is important to mention that the contrast degrades at the level of the smallest features (corresponding to 1 arcmin), but it is still possible to differentiate them. In any case, it is also important to keep in mind that the analogy with human vision is not perfect here

since there are other parameters affecting this performance (such as pixel characteristics of the camera, etc.).

It is worth mentioning that, while black and white images were used in this work, the image recording was performed by using a color (RGB) camera. As one can see, the edges of black and white zones remain very clear (without coloration) when the image is brought into focus. This shows that the chromatic aberrations are rather small at all spatial frequencies (averaged in the visible spectrum of the camera). In addition, the same lens was used in the past to record images of colored objects (described in the Fig.10 of [96]), and results reported there also confirm that chromatic aberrations are low.

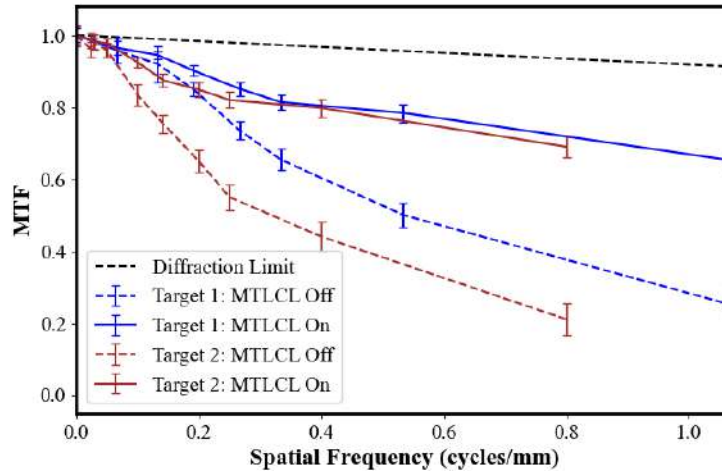
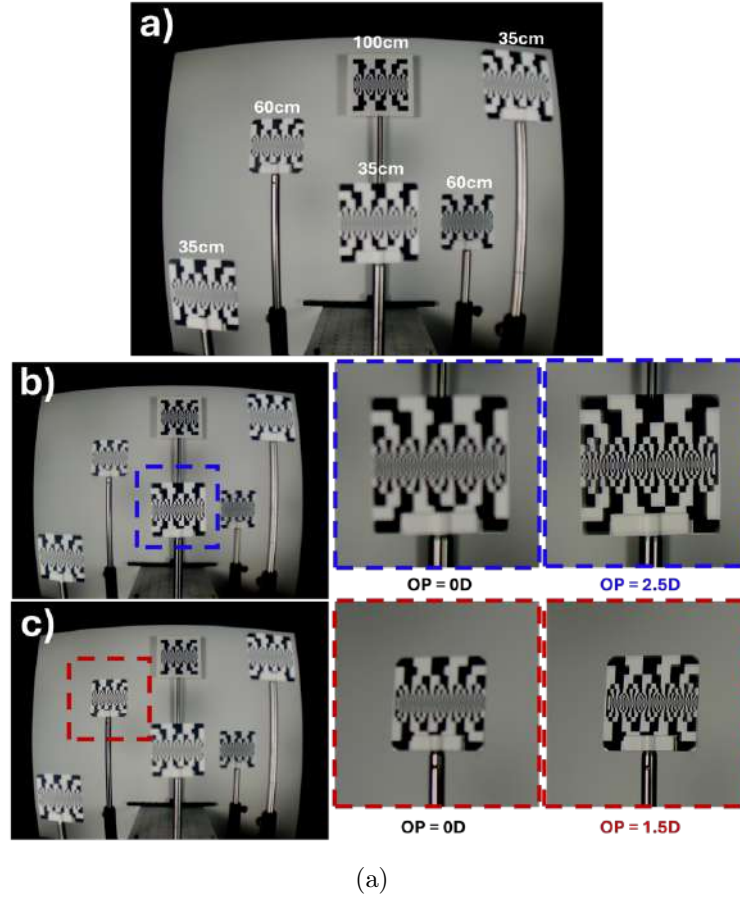


FIGURE 4.5 – (a) The experimental scene with 6 objects, placed at various positions (at 100, 60 and 35 cm from our lens) and at various angles. Demonstrated examples : a(b) - a local lens is activated (with OP=2.5 D) to focus on the target 1 (placed at 35 cm in the center), a(c) - The next local lens is activated (with OP=1.5 D) to focus on the target 2 (placed at 60 cm on the left). (b) Modulation Transfer Function (MTF) calculated for two different targets.

4.3.1 Transition speed measurements and optimization

One of the fundamental problems in the development of electrically controlled NLC lenses is their slow response time. For vision corrections, the accommodation time of the eye typically ranges from 0.3 s to 0.6 s in healthy adults [140]. In addition, the MTLCL's operation must comply with a real-time eye-tracking system. Thus, the entire system must adapt the MTLCL's OP and lateral position within these time scales to maintain clear vision across different viewing distances.

Also, the NLC layer of the MTLCL needs to be relatively thick since lens is operating in the refractive gradient index (GRIN) mode [65]. This is necessary to provide enough optical path difference $OPD = \delta n d$ (where d is NLC thickness and δn is the refractive index modulation depth that is limited by the optical birefringence Δn of the NLC) and corresponding range of focus changes. Indeed, the maximum achievable OP of a GRIN lens may be approximated as

$$OP \approx \frac{2 \times OPD}{(CA/2)^2} \quad (4.2)$$

Thus, the increase of d may help. However, by increasing d , we increase the time needed for the change of average orientation of the long molecular axis of the NLC (often called *director* [44]). Thus, the natural relaxation time τ_{off} (when the electrical voltage is simply switched off after some degree of excitation and NLC molecules orient back to the original state that is defined by the surface alignment in the cell) is described [141] by the following equation :

$$\tau_{off} \approx \frac{\gamma_1 d^2}{\pi^2 K} \quad (4.3)$$

where γ_1 and K are the rotational viscosity and elastic constants of the NLC, respectively. More detailed analyses should also take into account the fact that the excitation process may involve different types of director deformations. In this case, we should also consider different elastic constants. However, very often, a "one-constant" approximation works very well.

As one can see from Eq.4.3, the natural relaxation time τ_{off} (sometime also called turn-off time) depends only on material characteristics (γ_1/K) and the thickness d of the NLC. However, the excitation (or turn-on) time can be controlled also by the value of the applied (excitation) voltage U :

$$\tau_{on} \approx \frac{\tau_{off}}{((U/U_{th})^2 - 1)} \quad (4.4)$$

where U_{th} is the threshold voltage (typically at the order of 1V) of the director's reorientation [100]. It is also worth mentioning that, in so-called "modal-control" tunable lens designs (which is also the case here), the spatial distribution of electrical potential (and thus the local value of U) depends upon the excitation frequency due to the effective distributed RC circuit defined by the geometry (the structure) of the lens [142, 143].

Equation 4.4 shows that larger the value of U , the shorter is τ_{on} , while the natural relaxation τ_{off} still plays an important role. The problem of large τ_{off} has been addressed in the past

by using thinner cells or polymer-stabilized NLC. However, thinner cells result in a reduced OPD, and thus, small OP of the lens, while adding the polymer component causes increased light scattering that is also very undesired [144, 145].

Here several possibilities to overcome this problem are proposed. One of them follows the example, reported in [109], that addresses the need for fast switching of the MTLCL by using the frequency dependence of the NLC material itself (in contrast with the above mentioned structural dependence). This is a family of materials that we actually already use that is called dual-frequency NLC (DFNLC). It is well known that, in NLCs with positive dielectric anisotropy $\Delta\epsilon$, the director tends to be reoriented along the applied electric field, while in NLCs with negative dielectric anisotropy, the director is "repulsed" from the electric field (towards the perpendicular plane). In DFNLCs, the $\Delta\epsilon$ may change from a positive to a negative value with the change (increase) in the frequency of the applied electric field [133, 146]. The frequency, at which such a change of sign occurs, is known as the crossover frequency f_c . This distinctive behavior of DFNLC allows for the better control of switching times of NLCs not only by maintaining a desired level of excitation voltage, but also by changing its frequency from low f to higher F values. The above-mentioned repulsion process, coupled with the original surface alignment, allows recovering the initial (ground state) alignment faster compared to the case of natural relaxation. Thus, to benefit from the DFNLC character of NLC mixtures, F and f valued must be chosen to have them at opposite sides of the f_c (12 kHz for the DFNLC MLC-2048 used here).

To study the dynamic behavior of tunable lens (all measurements were performed at room temperature, $T = 292^\circ \text{ K}$), first, qualitative measurements of the wavefront of light transmitted through this lens were taken. A polarimetric imaging system was used for this purpose (see, e.g., [39, 38] for details). Namely, the MTLCL (with a single NLC layer) was placed between two crossed polarizers with the ground state orientation of the director along the diagonal (at 45° between two crossed polarizers). Thus, the incident probe beam (obtained from the same CW He-Ne laser) generated both ordinary and extraordinary polarized waves inside the NLC. The second polarizer was used as an analyzer, which "projected" these two waves onto its transmission axis' direction to produce their interference. The ordinary wave experiences a uniform phase shift everywhere in the NLC layer, while the phase shift for the extraordinary wave is different depending upon the position with respect to the center of the lens. Thus, the above-mentioned interference will generate light fringes (see Fig.4.6) the distances of which will be defined by the achieved phase shift (the distance between two dark fringes correspond to 2π shift on the wavefront) and thus will represent the evolution of the OP's value (the number of these rings can be used to estimate the value of the achieved OP [38], see hereafter for more quantitative details). These images were recorded by a camera in real time at the speed of 6 frame/s.

Figure 4.6 a) shows a sequence of non-optimized excitation conditions. As we can see, initially

(on the left, $t=0$ s) there are no fringes. The small variation of the brightness (along the diagonal) is related to the non uniformity of the NLC cell gap. Then, the direct application of excitation at 3.5 V generates a spherical wavefront delay and corresponding concentric fringes. It can be seen that the desired OP value is achieved very slowly (50 s). It is clear that such transition times are not acceptable.

To increase the transition speed, before the application of the final driving voltage $U_0 = 3.5$ V (corresponding to the desired value of OP), we can first apply a high-voltage *sin* wave U_h during a short time interval Δt (see eq.4.4). Hereafter, we refer to this burst of *sin* waves as "overdrive" (OD) pulses. Figure 4.6 b) shows an example of a sequence of optimized excitation (with an OD, applied during $\Delta t = 0.19$ s). As one can see, in this case, the focusing lens is formed much faster (multiple rings already appear already in the second picture from the left).

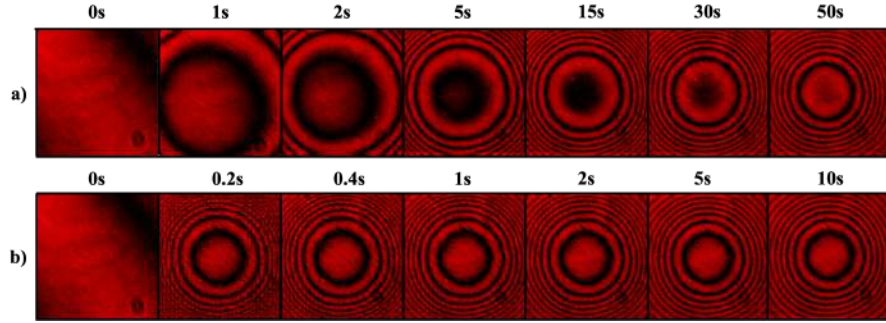


FIGURE 4.6 – Temporal evolution of polarimetric interference patterns (recording moments are displayed on the top of each image), a) without overdrive, $U = 3.5$ V b) with overdrive 20 V applied during $\Delta t = 0.19$ s.

Next, the same SHWFS were used for more quantitative analyses of transition times. Here again, an example of a non optimized excitation condition is selected to demonstrate the importance of an accurate choice of driving parameters. The transition time is measured between the original (ground state; OP=0 D) quasi-planar uniform alignment (here named S_1) of the NLC and a predefined focusing state (named S_2) for the following excitation parameters : Amplitude and frequency of the high frequency signal $U = 3.5$ V, $F = 120$ Hz, and the parameters of the low frequency (offset signal) $U_{off} = 1.2$ V, $f = 20$ Hz. The "standard" experimental curves, shown in Fig.4.7, correspond to this transition from S_1 to S_2 (non optimized activation) and from S_2 to S_1 (natural relaxation). The vertical axis shows the dynamic value of OP (normalized on the maximum OP), while the horizontal axis represents time (in seconds). These measurements were performed by using the same probe beam, a polarizer (aligned with the NLC's director to generate only extraordinary polarized light inside the NLC), the tunable lens, and a relay lens that was forming the image of the output plane of the proprietary lens on the SHWFS. The tunable lens was driven by *sin* wave voltages with modulated frequency and amplitude alternations (see the details in [96]). Voltage waveform generation, data acquisition, and analysis were performed in real time by using a proprietary software developed for the

team's measuring system.

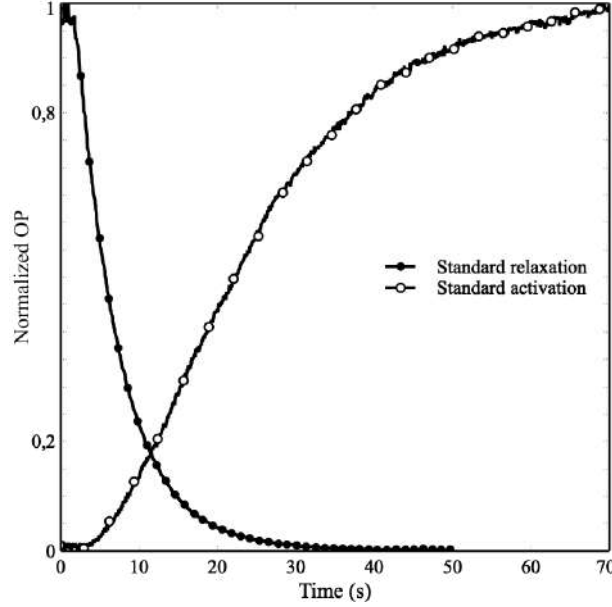


FIGURE 4.7 – Example of a non-optimized transition dynamics (change of the normalized optical power, OP) illustrating the slow response during the activation (turn-on) and relaxation for the following specific example of electrical excitation conditions : $U = 3.5$ V, $F = 120$ Hz, $U_{off} = 1.2$ V, and $f = 20$ Hz.

In the next experiment, various OD conditions were used to optimize (reduce) the transition times. Figure 4.8 shows examples of optimized OD pulse amplitudes and durations Δt that allowed the team to obtain significantly better (shorter) rise times τ_{on} . For example, if we choose $\Delta t = 0.75$ s at 14 V, then τ_{on} becomes smaller (about 2.1 s). It is important to emphasize that the exaggeration of OD excitation level may also increase the time needed to reach the desired value of OP. Thus, as can be ascertained (e.g. in Fig.4.8 (a)), the $\Delta t = 0.9$ s duration of OD is excessive and the final (desired) value of OP is reached significantly later compared to the case with the same amplitude of OD excitation but maintained during $\Delta t = 0.8$ s.

Furthermore, if it were decided to increase the amplitude of the overdrive pulse up to 20 V, for $\Delta t = 0.19$ s, then τ_{on} becomes even smaller (≈ 0.6 s, Fig. 4.8b). It is a clear improvement in comparison to the non-optimized approaches; e.g., when the final voltage is directly applied ($\Delta t = 0$) that provides a τ_{on} about 50 s.

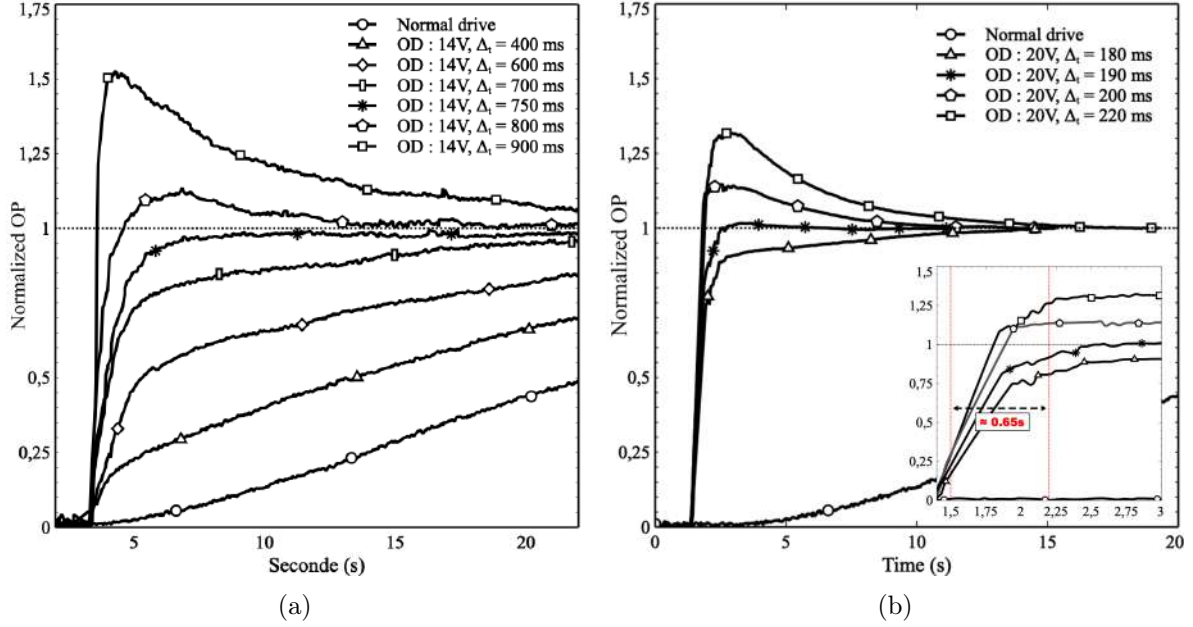


FIGURE 4.8 – Examples of optimization of the speed of the MTLCL with a) 14 V and b) 20 V overdrive (OD) voltages, applied with various pulse durations (Δ_t), compared with the normal drive response (without overdrive).

There are other ways to accelerate transitions. For example, it may be interesting to notice that the non-focusing state ($OP = 0$ D) may be achieved not only in the ground state, but also when the cell is uniformly activated. Namely, a lens can be first generated in a specific "focusing" state (say S2). Then, the excitation can be removed, after which natural relaxation will occur (when the director is back to its ground state), or voltage can be applied with high frequency (above f_c) to force this back reorientation. In contrast, the excitation can be "continued" up to the saturation of the director's reorientation. That is, one can take advantage of the fact that at low excitation frequencies, the electrical potential U propagates well across the NLC cell (almost uniformly over the lateral dimension of the layer). Thus, high voltage can be applied with rather low-frequency excitation (e.g., $f = 120$ Hz) at which the used NLC has positive dielectric anisotropy (below f_c). As a result, the director may be uniformly reoriented towards the homeotropic state (S3) where the director is aligned along the applied electrical field everywhere in the cell. This state will have $OP = 0$ D, it may be reached very quickly and, in addition, it will demonstrate the lowest possible light scatter [66].

Subsequently, it is possible to return to the S2 state (with specific OP value) by changing the frequency of excitation or to go back to the initial planar alignment S1 either naturally or by applying a high-frequency voltage (using the negative sign of the dielectric anisotropy $\Delta\epsilon < 0$ when a frequency above f_c is used).

The corresponding demonstrations and measurements of the turn-off time were performed at frequencies of 30 kHz, 70 kHz and 120 kHz (above f_c). For this experiment, two different

amplitudes of driving signals were applied, $U = 6$ V and $U = 14$ V. A few examples of the obtained electro-optical response of the MTLCL are shown in Fig.4.9.

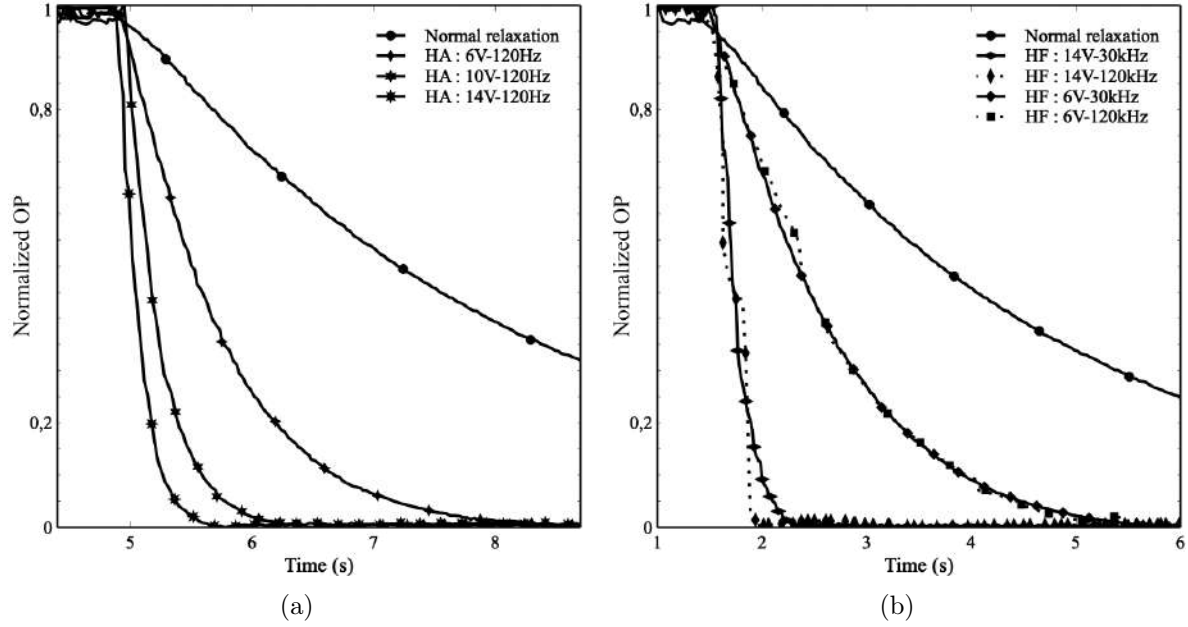


FIGURE 4.9 – Demonstrations of transition times with relatively high amplitude (HA) excitations at various frequencies from a predefined lens state (S2) to either a) to a quasi homeotropic state S3, or b) to a quasi planar state S1, both with zero OP.

Thus, according to Fig.4.9 and Fig.4.8, the turn-on time and turn-off times can be rather short (at the order of a half second), which makes DFNLC materials quite suitable for ophthalmic applications.

4.3.2 Application in presbyopia correction

Encouraged by the results obtained, the team proceeded to tests of human VA. It is worth reminding that the VA is the reciprocal of the angular size (in minutes of arc) of one of the elements of the target letter. “Normal” VA is considered to correspond to a minimum angle of resolution (MAR) of 1.0 minute of arc or also known as 20/20 (Snellen ratio), i.e., when the smallest recognizable letter subtends an angular height of 5 minutes from the eye and each element of the letter subtends 1 minute [20].

Thus, a VA of one-half, or 20/40, indicates that the minimum recognizable letter subtends 10 minutes and the MAR is 2 minutes. However, this is the value of VA under which it might be termed as “normal” condition, and it is the value only for that part of the FoV, which corresponds to the fovea of the retina. Outside the fovea, the acuity drops rapidly, as indicated in [2], which is a logarithmic plot of VA. The measurement of VA in the referenced studies is in agreement with the Logarithm of the Minimum Angle of Resolution (logMAR)

chart methodology, closely aligning with the Early Treatment Diabetic Retinopathy Study (ETDRS) standard [147]. This procedure involves presenting participants with lines of five random letters, selected from "Sans Font Sloan" letters [19, 148], with each subsequent line decreasing in size by 0.1 logMAR to incrementally assess the smallest detail the participant can accurately discern. The testing progresses until the participant incorrectly identifies three or more letters on the same line, at which point the acuity level of that line (adjusted by subtracting 0.02 logMAR for each letter incorrectly identified) is recorded as the participant's VA. This method provides a standardized way to evaluate visual performance under various conditions and with different visual corrections.

Approval for the study was obtained (study number 2021-272/23-09-2021) in accordance with the rules of the Comité d'éthique (ethics committee) de la recherche de l'Université Laval. Before the experimental procedures, informed consent was obtained from each patient after the nature of the study was explained. Exclusion criteria included myopia, ocular disease, amblyopia and/or strabismus and a history of ocular surgery or inflammation. Indeed, while the MTLCL may provide both positive and negative OP values (depending upon the LC and electrical control signals used), at this stage, all myopic patients were excluded (-0.5D and beyond) and the device developed was tested only for presbyopia correction. For this group of patients, no other requirements were specified, but the maximal OP was limited to $+3\text{ D}$ (the local lens' OP was varied from 0 to $+3.00\text{ D}$ on the defocus in steps of 0.5 D).

The study comprised three phases. First, the eye prescriptions of the patients were analysed; second, their VAs were evaluated; and third, attempts were made to correct their eyes' aberrations (defocus and astigmatism). The "wearer" of the MTLCL looked at charts at different distances, repeated once with no correction and once with the MTLCL being activated for correction. The next step was to find a local maximum of perceived visual quality by electrically tuning the lens properties (correction order was alternated between participants).

The proof of concept test was carried out on 7 subjects (aged between 45 to 70 years old), who were already diagnosed by a professional ophthalmologist. Thus, the exact eye corrections were already known on the basis of the corresponding prescription.

The correction procedure chosen was non-contact and without prior manipulation. MTLCL replaced the user's correction (pair of eyeglasses). The patient's head was positioned with temple supports and a chin rest to observe the scene presented in Figure 5a, which no longer included targets for estimating the MTF, but instead featured EDTRS targets for VA testing. Three targets were positioned at 35cm, three others at 1 meter; targets at 2.8 meters were placed within the field of view in the back of the scene. Letter sizes (in these targets) were adjusted according to the distances, with a print resolution of 300 dots per inch (dpi). At a given distance, multiple targets were analyzed within the total field of view. To minimize memory effects, the target was replaced with each increment of the lens's OP. For a given distance, the VA for each target was averaged to determine the corresponding VA.

While an eye was analyzed, an eye-patch was placed in front of the second eye. Scene illu-

mination was set to approximately 50 cd/m² to ensure comfort due to the sensitivity of the retina (with two white LEDs of 6200 Kelvin, with diffusors for homogenization).

The MTLCL logMAR VA (defocus curve; range from 0 to +3.00 D in 0.50 D steps) was evaluated.

It is worth reminding that the eyeglass prescription consists of spherical power *Sphere*, cylindrical power *Cyl* related to the astigmatism value, an axis direction, *axis* and additional magnifying power needed for near work, *ADD* diagnosis. They can be computed from the Zernike amplitudes [21] :

$$\begin{aligned} Cyl &= 2\sqrt{J_o^2 + J_{45}^2}, \\ Sphere &= D_r - \frac{Cyl}{2}, \\ axis &= -\arctan\left(\frac{Cyl/2 + J_o}{J_{45}}\right) \end{aligned} \quad (4.5)$$

Using the coefficients measured by the SHWFS, it is possible to convert these values into diopters, which quantify the OP of lenses. The first-order Zernike polynomials, as defocus and astigmatism, may be represented by mathematical expressions of a concave or convex wavefront [21]. The Peak Valley (PV) value, which represents the wavefront deviation is independent of the physical diameter of the pupil, as it solely describes the wavefront deviation along the Z-axis. To convert the PV value into the radius of curvature (RoC), a standard circle function was employed based on the "sagitta" formula [149]. After calculating the RoC, this value was converted to diopters (1/RoC), with D_r , the defocus diopter, J_o et J_{45} the lateral and oblique astigmatisms, respectively. The following equations were obtained [150] :

$$D_r = \frac{-16\sqrt{3}.a_4}{d^2}, \quad J_o = \frac{-8\sqrt{6}.a_5}{d^2}, \quad J_{45} = \frac{-8\sqrt{6}.a_6}{d^2} \quad (4.6)$$

These equations show that the MTLCL is able to tune diopter correction for defocus and astigmatism with a precise control of Zernike coefficients [132].

Coming back to the tests performed, a specific example of the applied procedure is as follows : the target was placed at 35 cm, refractive error ranged from +0.50 to +3.75 D (median spherical equivalent, +1.65 D). Astigmatism values for examined patients ranged from 0 to 1.25 D (median, 0.42 D), With the optimal diopter correction acuity ranging from -0.04 to +0.18 logMAR. Figure 4.10 presents the measured impact (individualized for each 7 patients) of the MTLCL's tuning on their VA, showcasing both the overall enhancement and the variation in performance across different patients. It can be seen that the obtained VA is a little lower than desired in most cases. There may be several reasons for this. First, at present, experiments were carried out without an eye tracking system. The transversal positions of local lenses (to be activated) were pre-registered to align (approximately) the retina, lenses and corresponding targets (in fixed positions). Better positioning of each lens (e.g., by using an eye tracking system to follow the movements of the head and thus of the eye) should enable better alignment and

results. Also, the printing quality of the targets used was not very good. Indeed, the targets were printed with 300 dpi resolution (in theory it should be sufficient for printing letters corresponding to 20/20 at 35 cm). However, it would have been preferable to print in 600 dpi to reduce (as much as possible) the degradation of edges on small letters, which can impact on the reading quality.

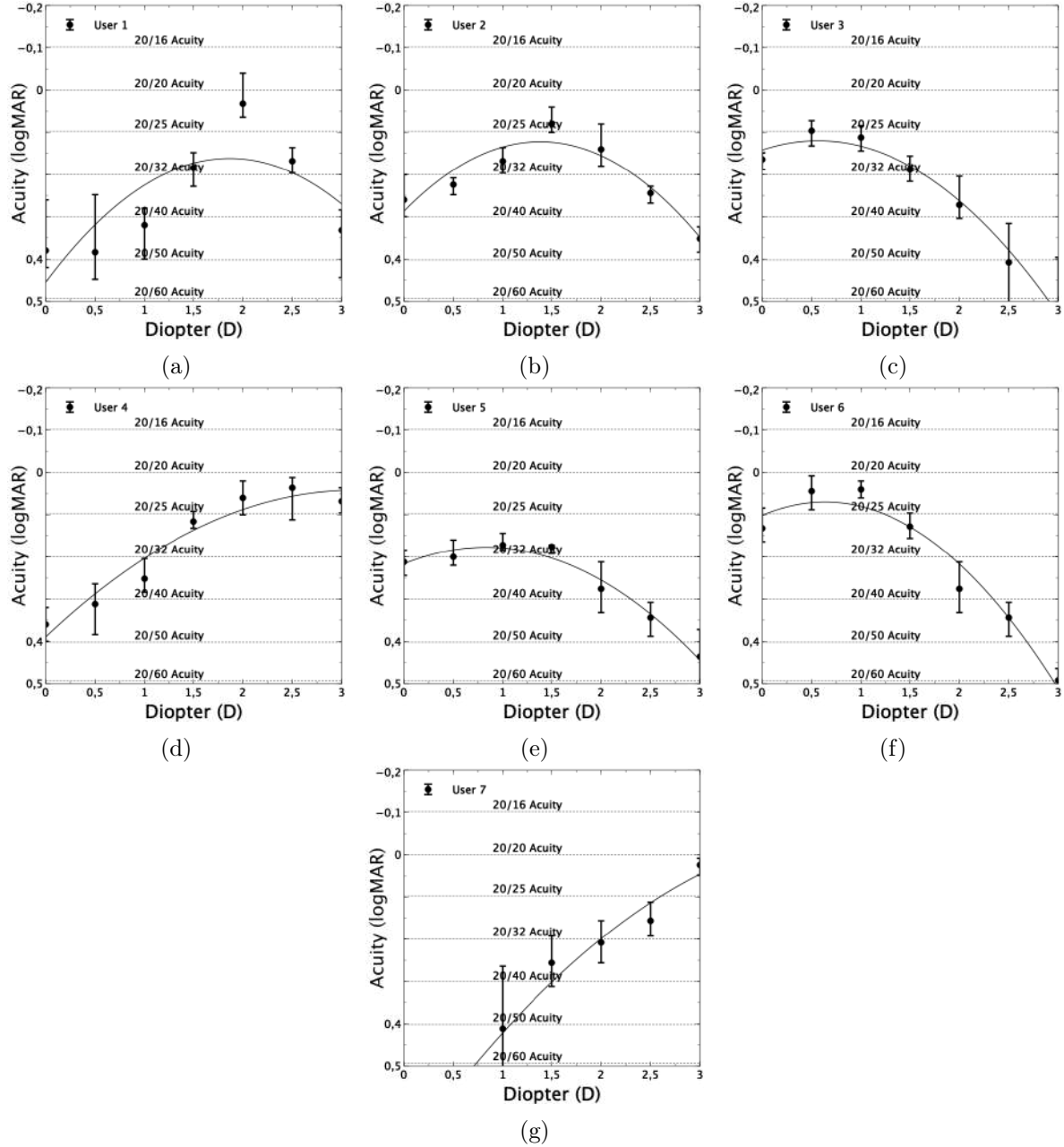


FIGURE 4.10 – Demonstration of the impact of the MTLCL on visual acuity of 7 patients.

The comparison of average VA for users is presented in Fig.4.11 in comparison between natural correction and when the MTLCL lens is activated and optimized in the first approximation.

As can be seen, here again, a rather significant improvement is obtained, by a factor of 3.4. The final state is very close to 20/20 vision.

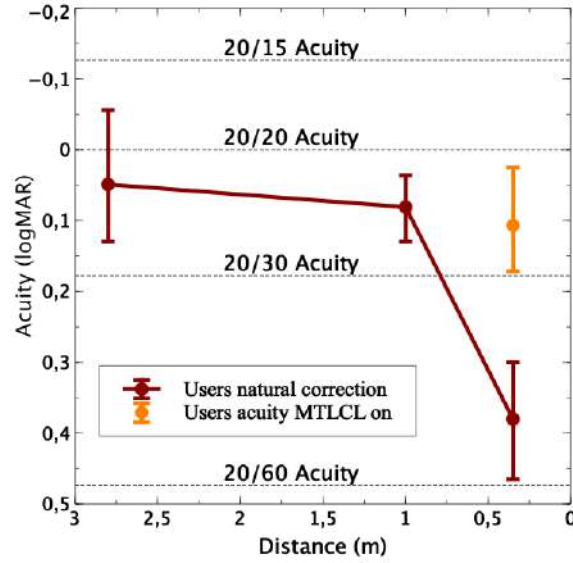


FIGURE 4.11 – Comparison between natural correction and when the MTLCL lens is activated (by using the average VA for users).

Discussion and Conclusion

As already mentioned, other physical mechanisms have been considered in the past to dynamically correct presbyopia. However, the reported (in the scientific literature) work with human tests seems to be very limited. For example, Monpean et al., report the use of a couple of liquid lenses (driven by pupil tracking) to correct presbyopia [151]. However, in addition to the presence of mechanical deformation (inside the structure of the lens), such lenses usually require very high voltages (up to 140V, [121]) and consequently their electrical power consumption will be very high.

That is why, it seems that the lens introduced here represents high potential for ophthalmic (mobile) applications. Already preliminary experimental tests conducted with a small group of patients have demonstrated that this lens effectively corrects the vision almost to natural vision, suggesting its potential as a practical solution for presbyopia correction. In addition, the same device can be used to dynamically generate various types of wavefront deformations (coma, astigmatism, etc., [132]) to correct corresponding aberrations in the human eye.

One of the performance aspects is the reaction speed. Its optimization (0.5 sec) was done at room temperature. At the same time, it is well known that LCs react differently for different temperatures (slower for low temperatures). For higher temperatures, the performance of the lens will be faster, but the optical power of the lens will degrade if the temperature is close to the so-called nematic-isotropic phase transition temperature T_c . However, currently, LC

mixtures are available that have a $T_c = 145^\circ\text{C}$. Thus, if the lens is used well below these temperatures (say, below 100°C), then the variations of the temperature will not noticeably affect the focusing capability.

Concerning the overall performance : as already mentioned, an eye-tracking system must be added to the device to provide information about the direction (to define the appropriate position of the local lens to be activated) as well as the distance (to define the value of OP to be generated) of the object of interest. Such devices are already widely used in Virtual Reality headsets and other mobile devices (displays, etc.), see, e.g., [152]. Most of them use either a camera or an emitter coupled with an array of photo detectors to track the eye direction and the distance of objects of interest. They are very miniature and will not add much volume and weight. In contrast, their integration will provide a more natural visual correction method that aligns closely with the physiological processes ongoing in the human eye.

The currently used substrates are thick (0.55 mm) for the easy manipulation of the prototype. However, the final (portable) device may be produced by using the latest generation of LC display manufacturing procedures to make it very thin. The best procedure known today uses 0.1 mm thick glass substrates (the 0.2 mm is already well mastered). This means that the total thickness of the element under discussion may be reduced down to 0.54 mm. The authors believe that this would be quite acceptable as thickness (standard eye glasses may be 3 mm thick in the center and 4 mm thick at the periphery).

While the current study focuses only on the ophthalmic case, it is worth mentioning that this capability of simultaneous focusing and wavefront tilting, provided by the proposed device, might be also explored to solve the vergence accommodation problem in virtual reality applications [153].

In addition, it was already demonstrated [132] that one can use the same device to generate also negative lenses, which may offer promising avenues for the simultaneous presbyopia and myopia corrections by the same device. Interestingly enough, this may be achieved by using dual frequency NLCs, which, in addition, may also help to further decrease the response time of the device developed.

Obviously, further developments and tests should be done to explore the eye tracking integration aspects. In the case of success (integration and operation), such a solution may help millions of people worldwide. The study reported here is only the first step, but it already showcases the technical feasibility of the device and sets the stage for its further development and integration into a practical and user-friendly device.

Disclosures

Authors have no conflict of interest to disclose.

Acknowledgments

We would like to thank LensVector inc and PATQER Photonique inc for their material support as well as Natural Sciences and Engineering Research Council of Canada (05888) and Canada Research Chairs (230212) for their financial support.

Data availability

Additional information may be obtained by contacting authors.

Conclusion

Cette thèse est l'introduction d'une nouvelle configuration de lentille à cristaux liquide pour la correction des aberrations en ophtalmologie et système de grandes ouverture. Ces travaux ont exploré une configuration novatrice exploitant une architectures matricielle associées à des électrodes en serpent, permettant une répétabilité dans la conception et un contrôle des propriétés optiques en temps réel, telles que la taille, la position et la correction de principales aberrations de premières ordres. Cette approche offre une flexibilité, étendant considérablement les possibilités des lentilles à cristaux liquides (LC) dans divers contextes, allant de la vision humaine à l'imagerie avancée [97]. Une modélisation théorique suivi d'une validation expérimentale et tests humains, ont établi non seulement la faisabilité technique mais aussi la robustesse et la polyvalence de ce dispositif, ouvrant la voie à une nouvelle génération de solutions optiques.

Les résultats obtenus montrent que ces lentilles, avec leur capacité à générer dynamiquement des focales variables, répondent efficacement aux besoins d'une vision personnalisée. Elles offrent également des solutions prometteuses pour la correction en temps réel des aberrations optiques primaires telles que la défocalisation, l'astigmatisme. La possibilité de moduler le diamètre des lentilles et leur position sur une grande ouverture optique, positionne ce dispositif comme des solutions futures pour des applications telles que la réalité augmentée, la correction de la vision humaine, et les systèmes d'imageries haute résolution.

Pour l'avenir, le potentiel d'amélioration de ce système est indéniable. Tout d'abord, une optimisation des tensions appliquées aux électrodes permettrait d'isoler d'avantage la lentille au travers de la matrice. En particulier, l'utilisation de tensions plus élevées sur les électrodes périphériques pourrait isoler davantage les zones actives en éliminant toutes perturbations sur les régions adjacentes. Par ailleurs, la possibilité d'activer simultanément plusieurs lentilles indépendantes au sein d'un même dispositif mérite une attention particulière, pour des applications tel que la microscopie et la vidéosurveillance.

Une autre perspective particulièrement prometteuse réside dans l'intégration de ces lentilles dans les systèmes de réalité virtuelle et augmentée. Ces environnements nécessitent une correction optique dynamique pour minimiser les distorsions visuelles et maximiser le confort utilisateur. Les lentilles LC peuvent non seulement corriger ces aberrations mais aussi s'adapter aux

mouvements de l'utilisateur grâce à des technologies telles que le suivi oculaire (eye-tracking). De surcroît, l'intégration de dispositifs d'estimation de la profondeur permettrait à ces lentilles de moduler automatiquement leur mise au point en fonction de la distance perçue, offrant une expérience immersive optimale.

L'exploration de lentilles négatives au travers de cette matrice représente une autre perspective intéressante. Ouvrant également une solution pour la correction de la myopie. Ouvrant ainsi la possibilité de corriger la très grande majorité des aberrations de la vision humaine, garantissant une correction adaptatives et dynamique même en cas de variations des conditions de vision.

Enfin, ces lentilles pourraient jouer un rôle clé dans le développement de systèmes optiques intelligents et autonomes. En couplant ces dispositifs à des capteurs avancés, il serait possible de créer des systèmes capables de s'ajuster automatiquement aux besoins de l'utilisateur, améliorant ainsi la qualité de la vision et l'interaction avec l'environnement visuel.

Bibliographie

- [1] H. Kolb, “How the retina works : Much of the construction of an image takes place in the retina itself through the use of specialized neural circuits,” *American scientist*, vol. 91, no. 1, pp. 28–35, 2003.
- [2] W. J. Smith, *Modern optical engineering : the design of optical systems*. McGraw-Hill Education, 2008.
- [3] G. Smith and D. A. Atchison, *The eye and visual optical instruments*. 1997.
- [4] D.-K. Yang and S.-T. Wu, *Fundamentals of liquid crystal devices*. John Wiley & Sons, 2014.
- [5] J. Piard, V. Genot, C. Adam, and C. Doré, “Synthèse d’un cristal liquide nématique : le mbba,” *Le Bulletin de l’Union des Professeurs de Physique et de Chimie*, vol. 109, no. 982, pp. 335–359, 2016.
- [6] A. Naumov, M. Y. Loktev, I. Guralnik, and G. Vdovin, “Liquid-crystal adaptive lenses with modal control,” *Optics letters*, vol. 23, no. 13, pp. 992–994, 1998.
- [7] A. Naumov, G. Love, M. Y. Loktev, and F. Vladimirov, “Control optimization of spherical modal liquid crystal lenses,” *Optics Express*, vol. 4, no. 9, pp. 344–352, 1999.
- [8] J. Stevens and T. Galstian, “Electrically tunable liquid crystal lens with a serpentine electrode design,” *Optics letters*, vol. 47, no. 4, pp. 910–912, 2022.
- [9] H. Gross, *Handbook of Optical Systems*. Wiley Online Library, 2005.
- [10] M. J. Booth, “Adaptive optics in microscopy,” *Philosophical Transactions of the Royal Society A : Mathematical, Physical and Engineering Sciences*, vol. 365, no. 1861, pp. 2829–2843, 2007.

-
- [11] L. N. Thibos, X. Hong, A. Bradley, and X. Cheng, "Statistical variation of aberration structure and image quality in a normal population of healthy eyes," *JOSA A*, vol. 19, no. 12, pp. 2329–2348, 2002.
 - [12] R. J. Noll, "Zernike polynomials and atmospheric turbulence," *JOsA*, vol. 66, no. 3, pp. 207–211, 1976.
 - [13] D. Purves, G. J. Augustine, D. Fitzpatrick, W. Hall, A.-S. LaMantia, and L. White, *Neurosciences*. De Boeck Supérieur, 2019.
 - [14] J. Liang, D. R. Williams, and D. T. Miller, "Supernormal vision and high-resolution retinal imaging through adaptive optics," *JOSA A*, vol. 14, no. 11, pp. 2884–2892, 1997.
 - [15] A. Glasser and M. C. Campbell, "Presbyopia and the optical changes in the human crystalline lens with age," *Vision research*, vol. 38, no. 2, pp. 209–229, 1998.
 - [16] H. Kolb, E. Fernandez, and R. Nelson, "The organization of the retina and visual system," *Webvision-the organization of the retina and visual system*, 2005.
 - [17] D. Purves and R. B. Lotto, *Why we see What we do : An Empirical theory of Vision*. Sinauer Associates, 2003.
 - [18] C. A. Curcio, K. R. Sloan, R. E. Kalina, and A. E. Hendrickson, "Human photoreceptor topography," *Journal of comparative neurology*, vol. 292, no. 4, pp. 497–523, 1990.
 - [19] I. L. Bailey and J. E. Lovie, "New design principles for visual acuity letter charts," *Optometry and Vision Science*, vol. 53, no. 11, pp. 740–745, 1976.
 - [20] A. Jackson and I. Bailey, "Visual acuity," *Optometry in Practice*, vol. 5, pp. 53–68, 2004.
 - [21] V. Lakshminarayanan and A. Fleck, "Zernike polynomials : a guide," *Journal of Modern Optics*, vol. 58, no. 7, pp. 545–561, 2011.
 - [22] S. Esposito, O. Feeney, and A. Riccardi, "Laboratory test of a pyramid wavefront sensor," in *Adaptive Optical Systems Technology*, vol. 4007, pp. 416–422, SPIE, 2000.
 - [23] I. Iglesias, R. Ragazzoni, Y. Julien, and P. Artal, "Extended source pyramid wave-front sensor for the human eye," *Optics express*, vol. 10, no. 9, pp. 419–428, 2002.
 - [24] R. Ragazzoni, "Pupil plane wavefront sensing with an oscillating prism," *Journal of modern optics*, vol. 43, no. 2, pp. 289–293, 1996.

-
- [25] J. C. Wyant, “Use of an ac heterodyne lateral shear interferometer with real-time wave-front correction systems,” *Applied optics*, vol. 14, no. 11, pp. 2622–2626, 1975.
 - [26] D. Malacara, “Optical shop testing,” *Wiley Interscience*, 2007.
 - [27] B. C. Platt and R. Shack, “History and principles of shack-hartmann wavefront sensing,” 2001.
 - [28] J. Liang, B. Grimm, S. Goelz, and J. F. Bille, “Objective measurement of wave aberrations of the human eye with the use of a hartmann-shack wave-front sensor,” *JOSA A*, vol. 11, no. 7, pp. 1949–1957, 1994.
 - [29] W. H. Southwell, “Wave-front estimation from wave-front slope measurements,” *JOSA*, vol. 70, no. 8, pp. 998–1006, 1980.
 - [30] F. Roddier, “Adaptive optics in astronomy,” 1999.
 - [31] J. W. Goodman, *Introduction to Fourier optics*. Roberts and Company publishers, 2005.
 - [32] M. Born and E. Wolf, *Principles of optics : electromagnetic theory of propagation, interference and diffraction of light*. Elsevier, 2013.
 - [33] J. Porter, A. Guirao, I. G. Cox, and D. R. Williams, “Monochromatic aberrations of the human eye in a large population,” *JOSA A*, vol. 18, no. 8, pp. 1793–1803, 2001.
 - [34] H. W. Babcock, “The possibility of compensating astronomical seeing,” *Publications of the Astronomical Society of the Pacific*, vol. 65, no. 386, pp. 229–236, 1953.
 - [35] E. J. Fernández, I. Iglesias, and P. Artal, “Closed-loop adaptive optics in the human eye,” *Optics letters*, vol. 26, no. 10, pp. 746–748, 2001.
 - [36] M. Glanc, E. Gendron, F. Lacombe, D. Lafaille, J.-F. Le Gargasson, and P. Léna, “Towards wide-field retinal imaging with adaptive optics,” *Optics Communications*, vol. 230, no. 4-6, pp. 225–238, 2004.
 - [37] L. Begel and T. Galstian, “Dynamic compensation of gradient index rod lens aberrations by using liquid crystals,” *Applied optics*, vol. 57, no. 26, pp. 7618–7621, 2018.
 - [38] L. Begel and T. Galstian, “Liquid crystal lens with corrected wavefront asymmetry,” *Applied optics*, vol. 57, no. 18, pp. 5072–5078, 2018.
 - [39] L. Tabourin and T. Galstian, “Liquid crystal module for motionless generation of variable structured illumination,” *JOSA B*, vol. 37, no. 7, pp. 2064–2070, 2020.

-
- [40] F. Reinitzer, “Beiträge zur kenntniss des cholesterins,” *Monatshefte für Chemie und verwandte Teile anderer Wissenschaften*, vol. 9, pp. 421–441, 1888.
 - [41] H. Kelker and B. Scheurle, “A liquid-crystalline (nematic) phase with a particularly low solidification point,” *Angewandte Chemie International Edition in English*, vol. 8, no. 11, pp. 884–885, 1969.
 - [42] F. C. Frank, “I. liquid crystals. on the theory of liquid crystals,” *Discussions of the Faraday Society*, vol. 25, pp. 19–28, 1958.
 - [43] C. Oseen, “The theory of liquid crystals,” *Transactions of the Faraday Society*, vol. 29, no. 140, pp. 883–899, 1933.
 - [44] P.-G. De Gennes and J. Prost, *The physics of liquid crystals*. No. 83, Oxford university press, 1993.
 - [45] I. W. Stewart, *The static and dynamic continuum theory of liquid crystals : a mathematical introduction*. Crc Press, 2019.
 - [46] R. A. Serway, J. W. Jewett, and V. Peroomian, *Physics for scientists and engineers*, vol. 2. Saunders college publishing Philadelphia, 2000.
 - [47] J. H. Adler, T. J. Atherton, T. R. Benson, D. B. Emerson, and S. P. MacLachlan, “Energy minimization for liquid crystal equilibrium with electric and flexoelectric effects,” *SIAM Journal on Scientific Computing*, vol. 37, no. 5, pp. S157–S176, 2015.
 - [48] M. Oh-e and K. Kondo, “Response mechanism of nematic liquid crystals using the in-plane switching mode,” *Applied physics letters*, vol. 69, no. 5, pp. 623–625, 1996.
 - [49] I.-C. Khoo, *Liquid crystals*. John Wiley & Sons, 2022.
 - [50] E. Jakeman and E. Raynes, “Electro-optic response times in liquid crystals,” *Physics Letters A*, vol. 39, no. 1, pp. 69–70, 1972.
 - [51] J. L. Ericksen, “Conservation laws for liquid crystals,” *Transactions of the Society of Rheology*, vol. 5, no. 1, pp. 23–34, 1961.
 - [52] F. M. Leslie, “Some constitutive equations for liquid crystals,” *Archive for Rational Mechanics and Analysis*, vol. 28, pp. 265–283, 1968.
 - [53] R. Dąbrowski, P. Kula, and J. Herman, “High birefringence liquid crystals,” *Crystals*, vol. 3, no. 3, pp. 443–482, 2013.

-
- [54] J. Wu, J. Cao, W.-Q. Han, A. Janotti, and H.-C. Kim, *Functional metal oxide nanostructures*, vol. 149. Springer Science & Business Media, 2011.
- [55] J. Algorri, P. Morawiak, N. Bennis, D. Zografopoulos, V. Urruchi, L. Rodríguez-Cobo, L. R. Jaroszewicz, J. Sánchez-Pena, and J. M. López-Higuera, “Positive-negative tunable liquid crystal lenses based on a microstructured transmission line,” *Scientific reports*, vol. 10, no. 1, p. 10153, 2020.
- [56] N. Bennis, T. Jankowski, P. Morawiak, A. Spadlo, D. C. Zografopoulos, J. M. Sánchez-Pena, J. M. López-Higuera, and J. F. Algorri, “Aspherical liquid crystal lenses based on a variable transmission electrode,” *Optics Express*, vol. 30, no. 8, pp. 12237–12247, 2022.
- [57] G. V. Vdovin, I. Guralnik, S. P. Kotova, M. Y. Loktev, and A. F. Naumov, “Liquid-crystal lenses with a controlled focal length. i. theory,” *Quantum Electronics*, vol. 29, no. 3, p. 256, 1999.
- [58] S. P. Kotova, S. Samagin, *et al.*, “Tunable liquid-crystal focusing device. 1. theory,” *Quantum Electronics*, vol. 41, no. 1, p. 58, 2011.
- [59] J. Algorri, G. Love, and V. Urruchi, “Modal liquid crystal array of optical elements,” *Optics express*, vol. 21, no. 21, pp. 24809–24818, 2013.
- [60] A. K. Kirby, P. J. Hands, and G. D. Love, “Liquid crystal multi-mode lenses and axicons based on electronic phase shift control,” *Optics express*, vol. 15, no. 21, pp. 13496–13501, 2007.
- [61] S. P. Kotova, V. Patlan, and S. A. Samagin, “Tunable liquid-crystal focusing device. 2. experiment,” *Quantum Electronics*, vol. 41, no. 1, p. 65, 2011.
- [62] T. Galstian, *Smart mini-cameras*, vol. 258. CRC press Boca Raton, 2014.
- [63] S. Sato, “Liquid-crystal lens-cells with variable focal length,” *Japanese Journal of Applied Physics*, vol. 18, no. 9, p. 1679, 1979.
- [64] V. G. Chigrinov, *Liquid crystal devices : physics and applications*. 1999.
- [65] Y.-H. Lin, Y.-J. Wang, and V. Reshetnyak, “Liquid crystal lenses with tunable focal length,” *Liquid Crystals Reviews*, vol. 5, no. 2, pp. 111–143, 2017.
- [66] T. Galstian, O. Sova, K. Asatryan, V. Presniakov, A. Zohrabyan, and M. Evensen, “Optical camera with liquid crystal autofocus lens,” *Optics express*, vol. 25, no. 24, pp. 29945–29964, 2017.

-
- [67] S. Kotova, V. Patlan, S. Samagin, and O. Zayakin, “Wavefront formation using modal liquid-crystal correctors,” *Physics of Wave Phenomena*, vol. 18, no. 2, pp. 96–104, 2010.
 - [68] S. Emberger, L. Alacoque, A. Dupret, C. L.-M. de Boissac, d. l. T. de Bougrenet, J. Louis, and N. Fraval, “Liquid crystal lens characterization for integrated depth sensing and all in focus imaging application,” *Electronic Imaging*, vol. 2017, no. 6, pp. 34–39, 2017.
 - [69] Y. Lei, Q. Tong, X. Zhang, H. Sang, A. Ji, and C. Xie, “An electrically tunable plenoptic camera using a liquid crystal microlens array,” *Review of scientific instruments*, vol. 86, no. 5, p. 053101, 2015.
 - [70] Y.-J. Wang, X. Shen, Y.-H. Lin, and B. Javidi, “Extended depth-of-field 3d endoscopy with synthetic aperture integral imaging using an electrically tunable focal-length liquid-crystal lens,” *Optics letters*, vol. 40, no. 15, pp. 3564–3567, 2015.
 - [71] A. Bagramyan, T. Galstian, and A. Saghatelian, “Motion-free endoscopic system for brain imaging at variable focal depth using liquid crystal lenses,” *Journal of biophotonics*, vol. 10, no. 6-7, pp. 762–774, 2017.
 - [72] J. Bailey, P. B. Morgan, H. F. Gleeson, and J. C. Jones, “Switchable liquid crystal contact lenses for the correction of presbyopia,” *Crystals*, vol. 8, no. 1, p. 29, 2018.
 - [73] A. Jamali, D. Bryant, A. K. Bhowmick, and P. J. Bos, “Large area liquid crystal lenses for correction of presbyopia,” *Optics Express*, vol. 28, no. 23, pp. 33982–33993, 2020.
 - [74] Z. Zemska and T. Galstian, “Electrically tunable lens with a non-monotonic wavefront control capability,” *Optics Letters*, vol. 47, no. 17, pp. 4287–4290, 2022.
 - [75] T. Galstian, “Electrode structure for creating electrical potential gradient,” Jan. 5 2023. US Patent App. 17/783,539.
 - [76] P. Valley, D. L. Mathine, M. R. Dodge, J. Schwiegerling, G. Peyman, and N. Peyghambarian, “Tunable-focus flat liquid-crystal diffractive lens,” *Optics letters*, vol. 35, no. 3, pp. 336–338, 2010.
 - [77] F. Kahn, “Electronically variable iris or stop mechanisms,” June 26 1973. US Patent 3,741,629.
 - [78] J. Algorri, V. Urruchi, N. Bennis, J. Sánchez-Pena, and J. Otón, “Tunable liquid crystal cylindrical micro-optical array for aberration compensation,” *Optics express*, vol. 23, no. 11, pp. 13899–13915, 2015.

-
- [79] J. F. Algorri, V. Urruchi, N. Bennis, P. Morawiak, J. M. Sánchez-Pena, and J. M. Otón, “Liquid crystal spherical microlens array with high fill factor and optical power,” *Optics express*, vol. 25, no. 2, pp. 605–614, 2017.
- [80] J. F. Algorri, V. Urruchi, B. García-Cámara, and J. M. Sánchez-Pena, “Liquid crystal lensacons, logarithmic and linear axicons,” *Materials*, vol. 7, no. 4, pp. 2593–2604, 2014.
- [81] O. Sova and T. Galstian, “Modal control refractive fresnel lens with uniform liquid crystal layer,” *Optics Communications*, vol. 474, p. 126056, 2020.
- [82] A. Pusenkova, O. Sova, and T. Galstian, “Electrically variable liquid crystal lens with spiral electrode,” *Optics Communications*, vol. 508, p. 127783, 2022.
- [83] J. Algorri, P. Morawiak, D. Zografopoulos, N. Bennis, A. Spadlo, L. Rodríguez-Cobo, L. R. Jaroszewicz, J. Sánchez-Pena, and J. M. López-Higuera, “Multifunctional light beam control device by stimuli-responsive liquid crystal micro-grating structures,” *Scientific Reports*, vol. 10, no. 1, pp. 1–10, 2020.
- [84] J. F. Algorri, P. Morawiak, D. C. Zografopoulos, N. Bennis, A. Spadlo, L. Rodríguez-Cobo, L. R. Jaroszewicz, J. M. Sanchez-Pena, and J. M. Lopez-Higuera, “Cylindrical and powell liquid crystal lenses with positive-negative optical power,” *IEEE Photonics Technology Letters*, vol. 32, no. 17, pp. 1057–1060, 2020.
- [85] Y. Zhang, G. Li, X. Chen, and M. Ye, “Driving methods for liquid crystal lens with rectangular aperture and four voltages,” *Japanese Journal of Applied Physics*, vol. 60, no. 10, p. 102002, 2021.
- [86] G.-m. Dai and V. N. Mahajan, “Orthonormal polynomials in wavefront analysis : error analysis,” *Applied optics*, vol. 47, no. 19, pp. 3433–3445, 2008.
- [87] M. Bray, “Orthogonal polynomials : a set for square areas,” in *Optical Fabrication, Testing, and Metrology*, vol. 5252, pp. 314–321, International Society for Optics and Photonics, 2004.
- [88] V. N. Mahajan and G.-m. Dai, “Orthonormal polynomials in wavefront analysis : analytical solution,” *JOSA A*, vol. 24, no. 9, pp. 2994–3016, 2007.
- [89] A. Bagramyan and T. Galstian, “Dynamic control of polarization mismatch and coma aberrations in rod-grin assemblies,” *Optics Express*, vol. 27, no. 10, pp. 14144–14151, 2019.

-
- [90] S. S. Reza, “A review paper on liquid crystal display,” *International Journal of Optical Sciences*, vol. 5, no. 1, pp. 5–8, 2019.
- [91] J. Huignard, “Spatial light modulators and their applications,” *Journal of optics*, vol. 18, no. 4, p. 181, 1987.
- [92] S. Sato, “Applications of liquid crystals to variable-focusing lenses,” *Optical Review*, vol. 6, pp. 471–485, 1999.
- [93] Z. Luo, Y. Li, J. Semmen, Y. Rao, and S.-T. Wu, “Achromatic diffractive liquid-crystal optics for virtual reality displays,” *Light : Science & Applications*, vol. 12, no. 1, p. 230, 2023.
- [94] E. Otón, P. Morawiak, R. Mazur, X. Quintana, M. A. Geday, J. M. Otón, and W. Piecek, “Diffractive and refractive liquid crystal devices based on multilayer matrices,” *Journal of Lightwave Technology*, vol. 37, no. 9, pp. 2086–2093, 2019.
- [95] O. Sova, V. Presniakov, A. Zohrabyan, S. Bassene, M. Cotovanu, A. Bagramyan, B. Khodadad, and T. Galstian, “Large diameter electrically tunable lens for ophthalmic distance accommodation,” *Biomedical Optics Express*, vol. 14, no. 12, pp. 6317–6327, 2023.
- [96] L. Bégel, B. Khodadad, and T. Galstian, “Adaptive lens for foveal vision, imaging, and projection over large clear apertures,” *Optics Express*, vol. 31, no. 2, pp. 2877–2891, 2023.
- [97] L. Tabourin, F. Bretzner, and T. Galstian, “Towards a mini-endoscope design with spatially selective excitation and imaging,” *Biomedical Optics Express*, vol. 15, no. 3, pp. 1750–1760, 2024.
- [98] K. Takato, M. Sakamoto, R. Hasegawa, M. Koden, N. Itoh, and M. Hasegawa, *Alignment technology and applications of liquid crystal devices*. CRC press, 2005.
- [99] S. Kotova, A. Mayorova, D. Prokopova, and S. Samagin, “Tunable liquid crystal astigmatic plate,” in *Journal of Physics : Conference Series*, vol. 1368, p. 022018, IOP Publishing, 2019.
- [100] L. M. Blinov and V. G. Chigrinov, *Electrooptic effects in liquid crystal materials*. Springer Science & Business Media, 2012.
- [101] J. Ye, Z. Gao, S. Wang, J. Cheng, W. Wang, and W. Sun, “Comparative assessment of orthogonal polynomials for wavefront reconstruction over the square aperture,” *JOSA A*, vol. 31, no. 10, pp. 2304–2311, 2014.

-
- [102] V. N. Mahajan and G.-m. Dai, “Orthonormal polynomials for hexagonal pupils,” *Optics letters*, vol. 31, no. 16, pp. 2462–2464, 2006.
 - [103] V. N. Mahajan, “Orthonormal polynomials in wavefront analysis,” in *Proceedings of the Optical Society of Korea Conference*, pp. 50–51, Optical Society of Korea, 2009.
 - [104] A. H. Al-Hamdani and S. Y. Hasan, “Zernike polynomials for optical systems with rectangular and square apertures of area equal to,” 2013.
 - [105] R. Lyons, “Sum of two sinusoids,” *For free publication by IOWEGIAN*, 2011.
 - [106] W. Feng, Z. Liu, and M. Ye, “Liquid crystal lens with a shiftable optical axis,” *Optics Express*, vol. 31, no. 10, pp. 15523–15536, 2023.
 - [107] M. Ye, B. Wang, and S. Sato, “Liquid crystal lens with focus movable in focal plane,” *Optics Communications*, vol. 259, no. 2, pp. 710–722, 2006.
 - [108] B. Wang, M. Ye, and S. Sato, “Liquid crystal lens with focal length variable from negative to positive values,” *IEEE Photonics Technology Letters*, vol. 18, no. 1, pp. 79–81, 2005.
 - [109] O. Pishnyak, S. Sato, and O. D. Lavrentovich, “Electrically tunable lens based on a dual-frequency nematic liquid crystal,” *Applied Optics*, vol. 45, no. 19, pp. 4576–4582, 2006.
 - [110] O. A. Zayakin, M. Y. Loktev, G. D. Love, and A. F. Naumov, “Cylindrical adaptive lenses,” in *Sixth International Symposium on Atmospheric and Ocean Optics*, vol. 3983, pp. 112–117, SPIE, 1999.
 - [111] R. Kosaki, N. Maeda, K. Bessho, Y. Hori, K. Nishida, A. Suzaki, Y. Hirohara, T. Mihashi, T. Fujikado, and Y. Tano, “Magnitude and orientation of zernike terms in patients with keratoconus,” *Investigative Ophthalmology & Visual Science*, vol. 48, no. 7, pp. 3062–3068, 2007.
 - [112] G. Kramida, “Resolving the vergence-accommodation conflict in head-mounted displays,” *IEEE transactions on visualization and computer graphics*, vol. 22, no. 7, pp. 1912–1931, 2015.
 - [113] S. Charrière and L. Duveau, “A vergence accommodation conflict-free virtual reality wearable headset,” in *Digital Optics for Immersive Displays*, vol. 10676, pp. 242–256, SPIE, 2018.

-
- [114] A. Glasser and M. C. Campbell, "Biometric, optical and physical changes in the isolated human crystalline lens with age in relation to presbyopia," *Vision research*, vol. 39, no. 11, pp. 1991–2015, 1999.
- [115] A. Duane, "Studies in monocular and binocular accommodation with their clinical applications," *American Journal of Ophthalmology*, vol. 5, no. 11, pp. 865–877, 1922.
- [116] B. A. Holden, T. R. Fricke, S. M. Ho, R. Wong, G. Schlenther, S. Cronjé, A. Burnett, E. Papas, K. S. Naidoo, and K. D. Frick, "Global vision impairment due to uncorrected presbyopia," *Archives of ophthalmology*, vol. 126, no. 12, pp. 1731–1739, 2008.
- [117] C. W. Brooks, *System for ophthalmic dispensing-e-book*. Elsevier Health Sciences, 2023.
- [118] J. E. Sheedy, C. Campbell, E. King-Smith, and J. R. Hayes, "Progressive powered lenses : the minkwitz theorem," *Optometry and Vision science*, vol. 82, no. 10, pp. 916–922, 2005.
- [119] W. N. Charman, "Developments in the correction of presbyopia ii : surgical approaches," *Ophthalmic and Physiological Optics*, vol. 34, no. 4, pp. 397–426, 2014.
- [120] L. W. Alvarez, "Two-element variable-power spherical lens," Feb. 21 1967. US Patent 3,305,294.
- [121] J. Jarosz, N. Molliex, G. Chenon, and B. Berge, "Adaptive eyeglasses for presbyopia correction : an original variable-focus technology," *Optics Express*, vol. 27, no. 8, pp. 10533–10552, 2019.
- [122] J. E. Floyd, "Fluid filled and pressurized lens with flexible optical boundary having variable focal length," Nov. 4 1997. US Patent 5,684,637.
- [123] S. Kuiper and B. H. W. Hendriks, "Variable focus spectacles," June 30 2009. US Patent 7,553,019.
- [124] Y.-H. Lin and H.-S. Chen, "Electrically tunable-focusing and polarizer-free liquid crystal lenses for ophthalmic applications," *Optics express*, vol. 21, no. 8, pp. 9428–9436, 2013.
- [125] H.-S. Chen, M.-S. Chen, and Y.-H. Lin, "Electrically tunable ophthalmic lenses for myopia and presbyopia using liquid crystals," *Molecular Crystals and Liquid Crystals*, vol. 596, no. 1, pp. 88–96, 2014.
- [126] T. Galstian, K. Asatryan, V. Presniakov, and A. Zohrabyan, "Electrically variable liquid crystal lenses for ophthalmic distance accommodation," *Optics Express*, vol. 27, no. 13, pp. 18803–18817, 2019.

-
- [127] S. P. Kern, “Variable power lens system,” July 22 1986. US Patent 4,601,545.
- [128] P. Valley, M. Reza Dodge, J. Schwiegerling, G. Peyman, and N. Peyghambarian, “Non-mechanical bifocal zoom telescope,” *Optics letters*, vol. 35, no. 15, pp. 2582–2584, 2010.
- [129] W. Feng and M. Ye, “Refractive fresnel liquid crystal lenses driven by two voltages,” *Optics Express*, vol. 32, no. 1, pp. 662–676, 2024.
- [130] A. Jamali, D. Bryant, Y. Zhang, A. Grunnet-Jepsen, A. Bhowmik, and P. J. Bos, “Design of a large aperture tunable refractive fresnel liquid crystal lens,” *Applied optics*, vol. 57, no. 7, pp. B10–B19, 2018.
- [131] T. Galstian, “Electrode structure for foveal lens device,” *U.S. Provisional Patent Application*, vol. 63/211,396, no. Jun. 16, 2021, 2021.
- [132] B. Louis and G. Tigran, “Dynamic control of defocus, astigmatism, and tilt aberrations with a large area foveal liquid crystal lens,” *Applied Optics*, vol. 63, no. 11, pp. 2798–2805, 2024.
- [133] A. B. Golovin, S. V. Shiyanovskii, and O. D. Lavrentovich, “Fast switching dual-frequency liquid crystal optical retarder, driven by an amplitude and frequency modulated voltage,” *Applied Physics Letters*, vol. 83, no. 19, pp. 3864–3866, 2003.
- [134] Y.-Y. Kao and P. C.-P. Chao, “A new dual-frequency liquid crystal lens with ring-and-pie electrodes and a driving scheme to prevent disclination lines and improve recovery time,” *Sensors*, vol. 11, pp. 5402–5415, 2011.
- [135] M. Ye, B. Wang, and S. Sato, “Double-layer liquid crystal lens,” *Japanese journal of applied physics*, vol. 43, no. 3A, p. L352, 2004.
- [136] Y. Wu, C. P. Chen, L. Mi, W. Zhang, J. Zhao, Y. Lu, W. Guo, B. Yu, Y. Li, and N. Maitlo, “Design of retinal-projection-based near-eye display with contact lens,” *Optics express*, vol. 26, no. 9, pp. 11553–11567, 2018.
- [137] R. Navarro, “The optical design of the human eye : a critical review,” *Journal of Optometry*, vol. 2, no. 1, pp. 3–18, 2009.
- [138] P. Zhao, Ç. Ataman, and H. Zappe, “Spherical aberration free liquid-filled tunable lens with variable thickness membrane,” *Optics Express*, vol. 23, no. 16, pp. 21264–21278, 2015.

-
- [139] L. Sun, S. Sheng, W. Meng, Y. Wang, Q. Ou, and X. Pu, “Design of spherical aberration free liquid-filled cylindrical zoom lenses over a wide focal length range based on zemax,” *Optics Express*, vol. 28, no. 5, pp. 6806–6819, 2020.
 - [140] J. A. Mordi and K. J. Ciuffreda, “Dynamic aspects of accommodation : age and presbyopia,” *Vision research*, vol. 44, no. 6, pp. 591–601, 2004.
 - [141] X. Nie, R. Lu, H. Xianyu, T. X. Wu, and S.-T. Wu, “Anchoring energy and cell gap effects on liquid crystal response time,” *Journal of Applied Physics*, vol. 101, no. 10, 2007.
 - [142] M. Loktev, “Modal wavefront correctors based on nematic liquid crystals,” *Ph. D. dissertation*, 2005.
 - [143] L. Tabourin, D. Brousseau, S. Thibault, and T. Galstian, “Wavefront control capability in a modal lens with segmented circular peripheral electrodes,” *Applied Optics*, vol. 62, no. 30, pp. 7970–7976, 2023.
 - [144] A. Pusenkova and T. Galstian, “Reducing the light scattering impact in liquid-crystal-based imaging systems,” *Applied Optics*, vol. 59, no. 16, pp. 4780–4789, 2020.
 - [145] Y.-H. Lin, W.-C. Cheng, H.-S. Chen, Y.-J. Wang, and X. Liang, “Orientation fluctuation in liquid crystal lenses,” *Journal of Optical Microsystems*, vol. 3, no. 4, pp. 041204–041204, 2023.
 - [146] H. Xianyu, S.-T. Wu, and C.-L. Lin, “Dual frequency liquid crystals : a review,” *Liquid Crystals*, vol. 36, no. 6-7, pp. 717–726, 2009.
 - [147] F. L. Ferris III, A. Kassoff, G. H. Bresnick, and I. Bailey, “New visual acuity charts for clinical research,” *American journal of ophthalmology*, vol. 94, no. 1, pp. 91–96, 1982.
 - [148] J. T. Holladay, “Proper method for calculating average visual acuity,” 1997.
 - [149] Wikipedia, “Sagitta (geometry),” 2024.
 - [150] X. Cheng, A. Bradley, S. Ravikumar, and L. N. Thibos, “Visual impact of zernike and seidel forms of monochromatic aberrations,” *Optometry and Vision Science*, vol. 87, no. 5, pp. 300–312, 2010.
 - [151] J. Mompeán, J. L. Aragón, and P. Artal, “Portable device for presbyopia correction with optoelectronic lenses driven by pupil response,” *Scientific Reports*, vol. 10, no. 1, p. 20293, 2020.

-
- [152] H. Singh and J. Singh, "Human eye tracking and related issues : A review," *International Journal of Scientific and Research Publications*, vol. 2, no. 9, pp. 1–9, 2012.
- [153] Y. Zhou, J. Zhang, and F. Fang, "Vergence-accommodation conflict in optical see-through display : Review and prospect," *Results in Optics*, vol. 5, p. 100160, 2021.